Squeezed Light at 2128 nm for future Gravitational-Wave Detectors

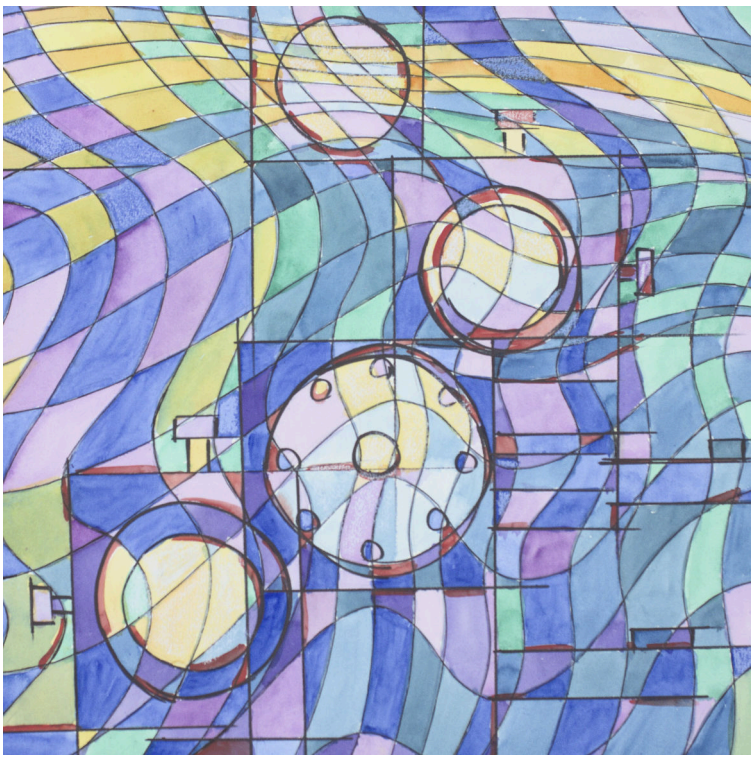

Christian Domenic Darsow-Fromm
2022

Squeezed Light at 2128 nm for future Gravitational-Wave Detectors

Dissertation
zur Erlangung des Doktorgrades
an der Fakultät für Mathematik, Informatik und Naturwissenschaften
Fachbereich Physik
der Universität Hamburg

vorgelegt von

Christian Domenic Darsow-Fromm

Hamburg

2022

Gutachter der Dissertation:	Prof. Dr. Roman Schnabel Prof. Dr. Sebastian Steinlechner
Zusammensetzung der Prüfungskommission:	Prof. Dr. Roman Schnabel Prof. Dr. Sebastian Steinlechner Prof. Dr. Oliver Gerberding Prof. Dr. Erika Garutti Prof. Dr. Michael Potthoff
Vorsitzender der Prüfungskommission:	Prof. Dr. Michael Potthoff
Datum der Disputation:	30.08.2022
Vorsitzender des Fach-Promotionsausschusses Physik:	Prof. Dr. Wolfgang J. Parak
Leiter des Fachbereichs Physik:	Prof. Dr. Günter Sigl
Dekan der Fakultät MIN:	Prof. Dr. Heinrich Graener

Coverbild: Alexandra Fromm

Kurzfassung

Seit der ersten Messung von Gravitationswellen im Jahr 2015 hat sich das Forschungsfeld zu Gravitationswellen-Astronomie weiterentwickelt, mit Multi-Messenger-Messungen und Ereignisstatistik. Rauschquellen müssen weiter reduziert werden, um die Messreichweite zu vergrößern und um mehr Informationen über die gemessenen Ereignisse zu bekommen. In aktuellen Observatorien ist das Brown'sche Rauschen der optischen Beschichtungen die dominante Rauschquelle bei etwa 100 Hz. Um diese thermische Rauschquelle zu vermeiden, sollen die Testmassen in zukünftigen Gravitationswellen-Observatorien (GWOs) auf kryogene Temperaturen gekühlt werden. Die mechanischen Eigenschaften des aktuell genutzten Quarzglases verschlechtern sich bei tiefen Temperaturen, weshalb kristallines Silizium mit amorphen siliziumbasierten Beschichtungen als Testmassen-Material in Betracht gezogen wird. Das macht jedoch einen Wechsel der Laser-Wellenlänge von 1064 nm zu etwa 2 µm notwendig. Dann ist Quantenrauschen die einzige verbleibende Rauschquelle bei mittleren und höheren Frequenzen. Daher werden alle notwendigen Technologien für die neue Wellenlänge mit hoher Priorität erforscht.

Diese Arbeit stellt eine gequetschte Lichtquelle bei 2128 nm vor, wo ein Nd:YAG nicht planarer Ring-Oszillator (NPRO) Laser bei 1064 nm verwendet wird, um über Wellenlängen-Verdopplung ultra-stabiles Laserlicht für Interferometrie bereitzustellen. Eine externe Konversionseffizienz von $\eta = (87.1 \pm 0.4)$ % (intern 93 %) konnte bei einer Pumpleistung von 52 mW erreicht werden. Eine Anpassung des Konversionsaufbaus zu höheren Laserleistungen könnte den Bedarf von 2 µm Laserverstärkern vermeiden. Die NPRO Laser wurden über Jahrzehnte stark optimiert, um die technologischen Voraussetzungen für Leistungsstabilität, Amplituden- und Phasenrauschen zu erreichen. Verfügbare Laser bei etwa 2 µm erreichen bislang nicht die benötigten Voraussetzungen, daran wird aber derzeit geforscht. Mit gequetschtem Licht wird die Unschärfe des Lichtfeldes auf (7.2 ± 0.2) dB unterhalb des Schrotrauschlevels reduziert, hauptsächlich limitiert durch die Quanteneffizienz von (92 ± 3) % der verfügbaren Photodioden. Als Teil der Technologieentwicklung wurden zwei digitale Regelungssysteme entwickelt, die benutzt werden, um Resonatoren (NQontrol) und Kristalltemperaturen (Raspitemp) zu stabilisieren. NQontrol ist ein quelloffenes digitales Regelungssystem, das acht Kanäle gleichzeitig regeln kann. Es bietet komplexe Möglichkeiten, Regelkreise zu optimieren und hohe Flexibilität, um das System an verschiedene Anforderungen anzupassen. Raspitemp ist ein modulares digitales Temperatur-Regelungssystem, das bis zu 20 Temperaturen gleichzeitig regeln kann, mit einer hohen Präzision von < 10 mK.

Um bei den GWOs der nächsten Generation das angestrebte Quetsch-Niveau von 10 dB zu erreichen, müssen die gesamten optischen Verluste von Interferometer und Detektion unter 10 % sein, was Photodioden mit einer Quanteneffizienz von 99 % notwendig macht. Der neuartige Ansatz, optisch-parametrische Ab-Konversion mit der Erzeugung von gequetschten Zuständen zu kombinieren, wird als Kandidat für GWOs der nächsten Generation in Betracht gezogen, wie etwa LIGO Voyager und dem Niederfrequenz-Teil des Einstein-Teleskops.

Abstract

Since the first detection of gravitational waves in 2015, the field has been developing to gravitational-wave astronomy with multi-messenger detections and event statistics. Noise sources need to be reduced further to increase the detection range and to get more information about the detected events. In current observatories, coating Brownian noise is the dominant noise source around 100 Hz. To avoid this thermal noise source, the test masses in future gravitational-wave observatories (GWOs) should be cooled to cryogenic temperatures. The mechanical properties of the currently used fused silica worsen at lower temperatures, and therefore the use of crystalline silicon as test mass material is considered, together with amorphous silicon-based coatings. However, this requires a change of the laser wavelength from 1064 nm to around 2 µm. Then, the only remaining noise source in the mid-range and at higher frequencies is quantum noise. Therefore, all technologies for the new wavelength are investigated at a high priority.

This thesis demonstrates a squeezed light source at 2128 nm via wavelength-doubling, where a Nd:YAG nonplanar ring oscillator (NPRO) laser at 1064 nm is used to provide ultra-stable laser light for interferometry. An external conversion efficiency of $\eta = (87.1 \pm 0.4)\,\%$ (internal 93 %) could be achieved at a pump power of 52 mW. Adapting the conversion scheme to higher laser power might avoid the need of 2 µm laser amplifiers. The NPRO lasers were highly optimized over decades to reach the technological requirements of power stability, amplitude and phase noise. Available lasers around 2 µm do not yet reach the required performance level, but are currently under research. Using squeezed light, the uncertainty of the light field is reduced to (7.2 ± 0.2) dB below shot noise, mainly limited by the quantum efficiency of $(92 \pm 3)\,\%$ of available photodiodes. As part of the technology development two digital control systems were developed which are used for stabilization of cavities (NQontrol) and crystal temperatures (Raspitemp). NQontrol is an open source digital control system that can control eight channels simultaneously, providing complex loop shaping abilities and high flexibility to adapt the system for different needs. Raspitemp is a modular digital temperature control system which can control up to 20 temperatures combined with a high accuracy of < 10 mK.

To reach the aimed squeezing level of 10 dB for the next-generation GWOs, the overall optical losses in the interferometer and the detection have to be below 10 %, requiring photodiodes with a quantum efficiency of 99 %. The novel approach of combining optical-parametric down-conversion with the creation of squeezed states is considered as a candidate for next-generation GWOs such as LIGO Voyager and the low-frequency part of the Einstein Telescope.

Contents

1 Gravitational-wave astronomy **1**

2 Nonclassical light **5**

2.1 Quantum states of light 5

2.1.1 Coherent states 5

2.1.2 Squeezed states 6

2.1.3 Influence of losses on squeezed light 8

2.2 Nonlinear crystals 9

2.2.1 Optical parametric oscillation 9

2.2.2 Generating squeezed states 12

2.3 Detection of light 13

2.3.1 Balanced homodyne detection 13

2.3.2 Limitations of InGaAs photodiodes 14

3 Conversion of bright coherent states from 1064 nm to 2128 nm **17**

3.1 Experimental setup 17

3.1.1 Laser preparation 18

3.1.2 Nonlinear cavities 19

3.1.3 Coupling efficiency measurements 22

3.1.4 Control scheme 23

3.2 Temperature dependencies 24

3.2.1 Output wavelength versus phase matching temperature 24

3.2.2 Detection of degeneracy of signal and idler modes 25

3.2.3 Output powers versus crystal temperatures 26

3.2.4 Finding degeneracy 26

3.3 Conversion efficiency . . . 29
3.4 Interference of converted beams . . . 31
3.5 Power stability . . . 32
3.6 Conclusion and outlook . . . 33

4 Generation of squeezed light at 2128 nm **35**
4.1 Experimental setup . . . 35
4.1.1 Balanced homodyne detection at 2128 nm . . . 36
4.1.2 Phase shifter pointing mismatch . . . 37
4.1.3 Beam overlap . . . 38
4.1.4 Monitoring and power adjustments . . . 38
4.2 Photodiode quantum efficiency . . . 40
4.3 Squeezing at MHz sideband frequencies . . . 42
4.4 Optical loss analysis . . . 43
4.5 Cooling of photodiodes . . . 45
4.6 Conclusion . . . 46

5 Digital control systems **47**
5.1 Introduction to control systems . . . 47
5.1.1 System dynamics . . . 48
5.1.2 Frequency domain . . . 48
5.1.3 Feedback . . . 49
5.1.4 Zeros and poles . . . 51
5.1.5 Control filters . . . 51
5.1.6 Feedback optimization and stability . . . 53
5.1.7 Practical example: optical cavity . . . 53
5.1.8 Going digital . . . 54
5.2 NQontrol – A new open source digital control system . . . 55
5.2.1 Design considerations . . . 56
5.2.2 Implementation . . . 57
5.2.3 Performance . . . 60
5.2.4 Filter design automation . . . 65
5.2.5 Autolock . . . 70

5.3 Raspitemp – A digital temperature control system 71
5.3.1 Design considerations 71
5.3.2 Implementation 72
5.3.3 Daily lab usage 80
5.4 Summary 80

6 Summary and Outlook **81**

Appendix **83**
A Homodyne detector 83
B Temperature control system 84

Bibliography **94**

1 | Gravitational-wave astronomy

Since the observation of the first black-hole coalescence in 2015 [Abb+16], gravitational-wave detection has evolved from proof-of-principle experiments into the new field of gravitational-wave astronomy [LIG17; LIG20]. Further increasing the sensitivity of detectors does not only allow the observation of weaker signals, but expands the observable area in the universe. This promises new insights into cosmology and even the origin of the universe by statistical evaluation of the gravitational-wave background [Sho19]. In the context of multi-messenger astronomy, the low-frequency regime is of particular interest, since merger events cross the gravitational-wave spectrum days to weeks before the coalescence, giving ample pre-warning for a precise sky localization of any electro-magnetic counterpart. Gravitational-wave detectors with a tenfold increased reach for sources producing signal frequencies around 100 Hz and with hundred times larger range around 10 Hz seem feasible [Rei+19; ET 20]. Such high sensitivities expand the detection range toward the entire universe for some sources, will result in a quasi permanent observation of mutually overlapping signals, and will promise new insights into cosmology and even the origin of the universe.

Besides another confirmation of the general relativity theory, important fundamental questions have already been answered within the field of gravitational-wave astronomy. The speed of gravitational waves was confirmed to be the same as the speed of light within very narrow boundaries, as expected by electro-magnetic theory [Abb+17c]. The measurement was inferred from a binary neutron star merger, from which the gravitational waves and a gamma-ray burst was measured simultaneously. Furthermore, the Hubble constant (a measure of universe expansion velocity) was confirmed by using the same neutron star merger as a gravitational-wave standard siren [Abb+17a]. While until now, standard candles (that means, objects with known luminosity) were necessary to estimate the distance to the object of study, the merger allows to estimate the distance to the event in an independent manner and provides a confirmation of the procedure used so far. Using a standard siren, the mass can be derived from merger frequencies and thus, the signal amplitude is known and, in case of gravitational waves, not absorbed by matter on its path to earth. Future measurements could provide more precision to solve the Hubble tension, where multiple measurements provide different and conflicting values for the Hubble constant [Val+21]. The neutron-star merger was a quite informative event and it was even possible to discover an origin of heavy elements (heavier than iron) [Kas+17; Abb+17b]. After the event, the resulting kilonova was optically bright for some days and modeling of the time-dependent spectrum suggests a high contribution to the nucleosynthesis of heavy elements.

An increased sensitivity would allow to refine upper limits for theoretical predictions, such as the isotropic [Col+21] and anisotropic [Abb+21] gravitational-wave background. Those upper

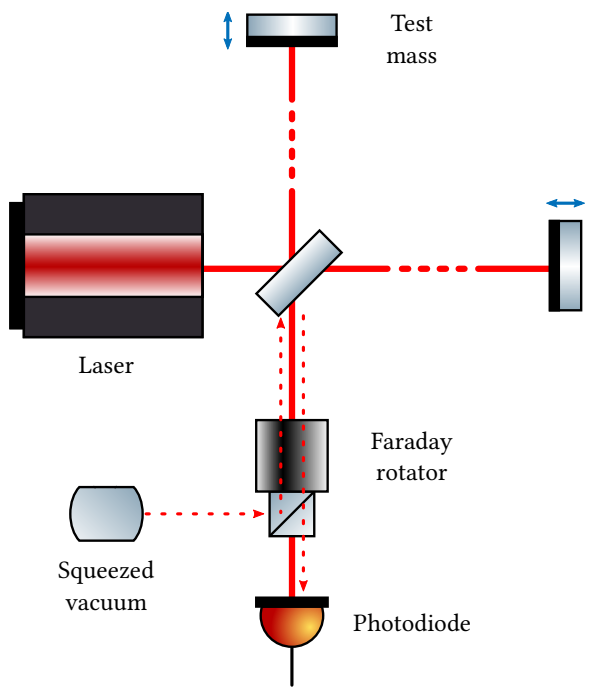

Figure 1.1: Principle of a gravitational-wave detector with Michelson configuration. It consists of two long interferometer arms, 4 km in the case of LIGO. Squeezed vacuum is injected into the interferometer to reduce vacuum noise acting on the mirrors.

limits can be refined as the detector sensitivity increases and future measurements could possibly even challenge the inflation theory of early universe expansion. In general, gravitational waves provide different information as the origin is in the bulk motion of their sources and not energy states of individual atoms. Even if gravitational waves can in principle be absorbed by dissipative heavy matter, the interaction is minuscule [Loe20], providing information about hidden regions and, hopefully, the Big Bang. Useful introductions to gravitational waves can be found in [Cre21; Sau17]. [Cre21] includes details of the calculation of gravitational-wave strain, while [Sau17] introduces the general relativity formalism.

There are currently several GWOs running: two LIGO detectors in Hanford and Livingston, Virgo in Italy, GEO 600 in Hannover and KAGRA in Japan. All current detectors are Michelson interferometers with arm lengths of several kilometers and reach a relative sensitivity of 10^{-23}. Figure 1.1 illustrates the principle of such a detector. The output of the interferometer runs as dark-port with nearly perfect destructive interference. Additionally, the signal strength is enhanced by arm cavities, power and signal recycling cavities. If a gravitational wave passes the detector, the lengths of the arms vary slightly, producing a measurement signal on the photodiode. As the impact of gravitational waves is extremely small, the signal-to-noise ratio has to be increased as much as possible to measure them.

There are plenty of necessary techniques to get the sensitivity high enough. Here, I will focus on quantum noise, being fundamental part of this thesis, and thermal noise, motivating the usage of light around 2 µm. The design noise budget of Advanced LIGO is shown in figure 1.2, where a strain of around $10^{-23}/\sqrt{\mathrm{Hz}}$ is reached, meaning that on a distance of 1 km length changes of 10^{-20}m can be detected. Here, the frequency-dependent sensitivity is shown, with the major contributions of seismic at low frequencies, coating Brownian noise in the mid-range and quantum noise at the remaining frequencies. The seismic noise is reduced by hanging heavy test masses (40 kg in the case of Advanced LIGO [Adh+20]) on long pendulums, which also helps to keep the radiation pressure noise low.

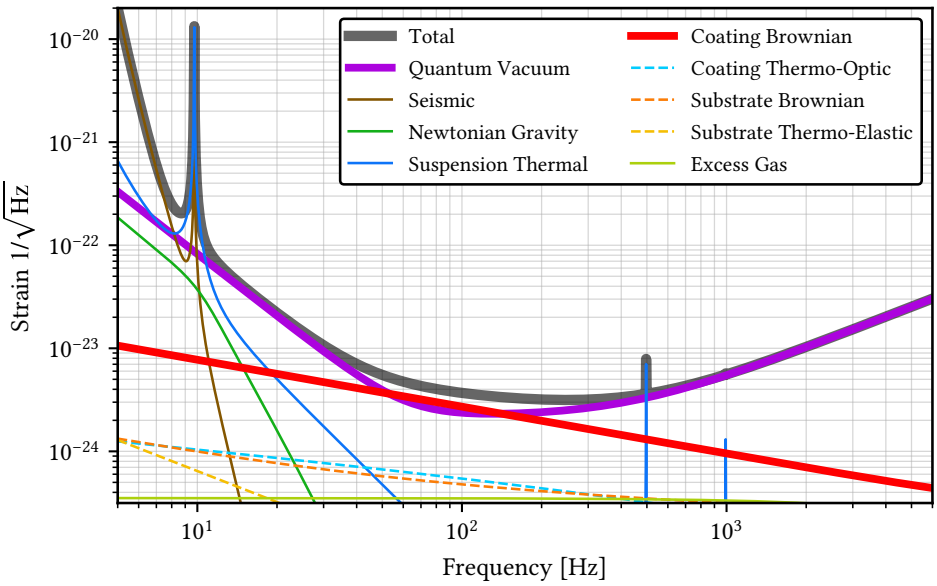

Figure 1.2: Advanced LIGO noise budget, shows the relative sensitivity (strain) in the frequency band of the detection. Already the currently running Advanced LIGO is limited by quantum noise over most of the detection range. Figure created with pygwinc and its included noise budgets [LIG].

At frequency ranges where all classical noise sources can be avoided, the fundamental quantum noise remains. In case of light, this is radiation pressure noise and shot noise; radiation pressure noise slightly moves the test masses of a gravitational-wave detector. Radiation pressure noise reduces by using less laser power, but at the cost of lowered sensitivity at high frequencies due to shot noise. Current GWOs are limited by photon radiation pressure noise at sub-audio frequencies and by photon counting noise (shot noise) in the higher audio-band [LIG19]. Reducing the quantum noise further requires squeezing the optical quantum uncertainty [Cav81; Sch+10; Sch17] over the entire spectrum of expected signals, as first achieved in [Vah+07]. By using filter cavities [Kim+01; Che+05; Kha10] or conditional squeezing [Ma+17; Süd+20], the squeezed light enhances the sensitivity for all frequencies simultaneously.

The current observatories use ultra-stable laser devices with powers of up to 160 W and squeezed light sources with a nonclassical noise suppression between 7 dB and 12 dB [Vah+10; MV18]. Optical resonators increase the light powers to up to 750 kW in the 4 km long arms in the case of Advanced LIGO [Aas+15]. Optical loss and phase noise reduce the squeeze factor to 6 dB in the case of GEO 600 [LIG11; Gro+13; Lou+21] and around 3 dB in LIGO and Virgo [Tse+19; Ace+19].

Except for KAGRA, where sapphire test masses are used [Hir+14], the mirror material is fused silica [LIG16; Ace+15], coated using silica and tantala. Despite providing excellent optical quality, coating thermal noise poses a significant limitation to the current detectors, particularly in the mid-frequency range from several tens of Hz to a few hundreds of Hz [Lev98; Har+02; Bar+18]. Usually, thermal noise issues can be circumvented by cooling, but in this case, the mechanical loss increases on cooling [Mar+09; Mar+14] and hence the thermal noise. Silicon with current coatings as used in Advanced LIGO can be cooled to cryogenic temperatures and operated at 1550 nm, reducing coating Brownian noise to 50 %. A wavelength around

2 µm would allow using novel amorphous silicon coatings, that can reduce the coating thermal noise to only 8% the latter [Ste+18].

For further improvements, future observatories such as the Einstein Telescope are planned to have some crucial design differences [ET 20]. Seismic noise will be reduced by building the interferometer in an underground location. Furthermore, coating noise needs to be reduced; here, silicon test masses and amorphous silicon coatings are promising candidates. When choosing silicon test masses, the squeezing has to be adapted for quantum noise reduction around 2 µm. The limitation by thermal noise could be avoided by operation at cryogenic temperatures, which requires a change of the mirror substrate and coating materials. The most promising substrate candidate, crystalline silicon, excels with high mechanical Q-factor and thermal conductivity in the cryogenic regime, in contrast to the currently used fused silica [Hil+10; ET 11]. On the other hand, latest research in coating technology has shown promising mechanical loss results with amorphous silicon thin films [Mur+15]. Optimized coatings from this material suggest that a thermal noise reduction by a factor of twelve below conventional silica-tantala coatings is possible [Ste+18]. However, the operation wavelength with these novel coatings is restricted to above 1.8 µm, since otherwise the absorption would exceed the required order of a few ppm [ET 11; LIG19; GK95], which would lead to significant heating of the test masses, distortions from thermal lensing and hinder advanced quantum sensing techniques. As such, design studies for upcoming detector generations such as LIGO Voyager [Adh+20], Cosmic Explorer [LIG19], the Einstein Telescope [ET 20] and NEMO [Ack+20] feature wavelengths around 2 µm. Prototype facilities like ETpathfinder [ETp20] are planning to investigate interferometry with this novel wavelength for gravitational-wave detection.

New laser schemes have to provide a comprehensive solution for high precision quantum metrology, including optics and detection devices [Sch+10; LIG11; Tse+19; Ace+19]. In addition, the laser sources themselves have stringent requirements in terms of power stability, amplitude and phase noise, as well as spatial mode quality. It took decades of development effort to reach the technological matureness with laser sources at 1064 nm. Laser technologies at around 2 µm are most often based on either holmium- or thulium-doped laser media. As their conventional use in medical and LIDAR applications does not require exceptional stability, their maturity and performance levels miss the performance goal of 1064 nm-technology by far [Man+18]. Increasing the signal requires ultra-stable laser radiation, that is not absorbed or scattered by the test mass mirrors.

A first squeezed light source for the 2 µm region was previously reported in [Yap+19; Man+18]. Squeeze factors of up to 4 dB were measured. The value was limited by the quantum efficiency of the photo detectors, as well as noise of the 1984 nm thulium fiber laser and subsequently its second harmonic pump field at 992 nm.

In the scope of this thesis, I realized a squeezed light source at the new wavelength of 2128 nm that uses stable 1064 nm pump light from a Nd:YAG nonplanar ring oscillator (NPRO), which is also used as the main laser in current GWOs. The 2128 nm light source is described in chapter 3 and published in [Dar+20a], while the description and analyzation of the squeezing can be found in chapter 4 and published in [Dar+21]. Additional part of the project was the development of two digital control systems to stabilize the optical cavities (published in [Dar+20b]) and to control multiple temperatures with a precision of some Millikelvin, which are presented in chapter 5.

2 | Nonclassical light

2.1 Quantum states of light

Squeezed states of light can not be explained classically and require a quantum-mechanical description. This section mainly follows Gerry and Knight [GK05].

2.1.1 Coherent states

A coherent state is the description of a Gaussian wave packet in a quantum-mechanical harmonic oscillator. The Hamiltonian of the quantum-mechanical harmonic oscillator reads

$$\hat{H} = \frac{1}{2}(\hat{p}^2 + \omega^2 \hat{q}^2)\,. \tag{2.1}$$

With the annihilation and creation operators

$$\begin{aligned} \hat{a} &= \frac{1}{\sqrt{2\hbar\omega}}(\omega\hat{q} + i\hat{p}) \\ \hat{a}^\dagger &= \frac{1}{\sqrt{2\hbar\omega}}(\omega\hat{q} - i\hat{p})\,, \end{aligned} \tag{2.2}$$

the Hamiltonian becomes

$$\hat{H} = \hbar\omega\left(\hat{n} + \frac{1}{2}\right) \tag{2.3}$$

where $\hat{n} = a^\dagger \hat{a}$ is the number operator.

The creation and annihilation operators can be used to formulate the amplitude and phase quadrature operators

$$\begin{aligned} \hat{X} &= \hat{a}^\dagger + \hat{a} \\ \hat{Y} &= i(\hat{a}^\dagger - \hat{a})\,. \end{aligned} \tag{2.4}$$

The different formulations of the Hamiltonian are thus [Sch17]

$$\hat{H} = \hbar\omega\left(\hat{n} + \frac{1}{2}\right) = \hbar\omega\left(\hat{a}^\dagger\hat{a} + \frac{1}{2}\right) = \hbar\omega\left(\hat{X}^2 + \hat{Y}^2\right)\,. \tag{2.5}$$

This equation shows the wave-particle dualism, where the eigenvalues of $\hat{n}$ have a discrete spectrum and the ones of $\hat{X}$ and $\hat{Y}$ a continuous spectrum.

Coherent states are defined as eigenstates of the annihilation operator which satisfy

$$\hat{a}|\alpha\rangle = \alpha|\alpha\rangle \tag{2.6}$$

and can be expressed as

$$|\alpha\rangle = e^{-\frac{1}{2}|\alpha|^2} \sum_{n=0}^{\infty} \frac{\alpha^n}{\sqrt{n!}}|n\rangle = \hat{D}(\alpha)|0\rangle\,, \tag{2.7}$$

which equals the formulation using the displacement operator

$$\hat{D}(\alpha) = \exp(\alpha\hat{a}^\dagger - \alpha^*\hat{a}) \tag{2.8}$$

on the vacuum state $|0\rangle$. The coherent state can be imagined as a displaced vacuum state in the phase space (compare figure 2.1) which corresponds to an amplification of spontaneous emission in a laser. α is a complex value where $|\alpha|$ is related to the amplitude of the field. The expectation value of the photon number can be calculated with

$$\bar{n} = \langle\alpha|\hat{n}|\alpha\rangle = |\alpha|^2 \tag{2.9}$$

and the standard deviation becomes

$$\Delta n = \sqrt{\bar{n}}. \tag{2.10}$$

A coherent state has minimal uncertainty in amplitude *and* phase, which equals the uncertainty of the vacuum field and has an equal distribution between amplitude and phase uncertainty

$$\Delta^2\hat{X} \cdot \Delta^2\hat{Y} \geq 1\,. \tag{2.11}$$

In the high-amplitude limit, the coherent state is similar to a classical noiseless wave [Sch26], while at low amplitudes, photon statistics becomes relevant, and in the case of gravitational-wave detection quantum effects become visible at high measurement sensitivity.

2.1.2 Squeezed states

When a coherent state is squeezed, the uncertainty in one quadrature becomes reduced and increased in the other (figure 2.2). This way, quantum noise limited measurements can be improved in sensitivity. Also squeezed states have to fulfill the Heisenberg uncertainty. Consider the squeezing operator

$$\hat{S}(\xi) = \exp\left(\tfrac{1}{2}(\xi^*\hat{a}^2 - \xi\hat{a}^{\dagger 2})\right) \tag{2.12}$$

with the parameter $\xi = re^{i\theta}$, the squeeze parameter r which is defined in the range $0 \leq r < \infty$ and the angle θ in the range $0 \leq \theta \leq 2\pi$. The operator is a two-photon generalization of the displacement operator. Acting on vacuum we get the state

$$|\xi\rangle = \hat{S}(\xi)|0\rangle. \tag{2.13}$$

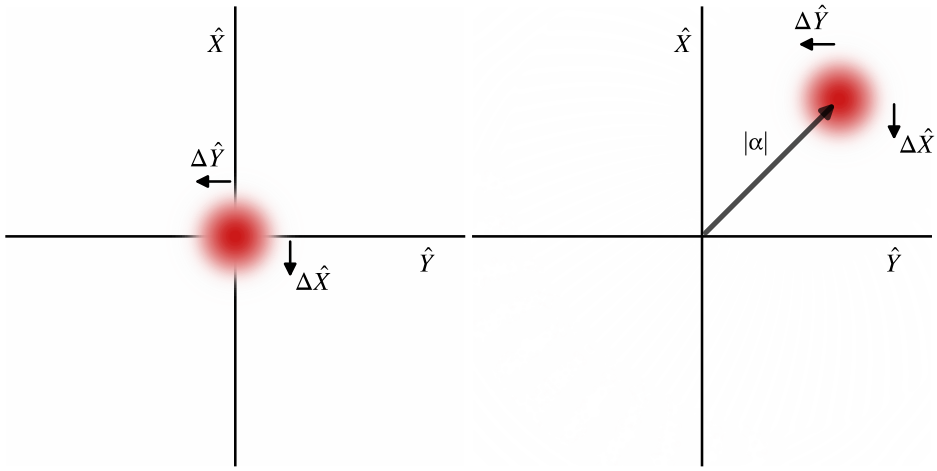

Figure 2.1: Displacement producing a coherent state (right) out of a vacuum state (left). The size of the red circle demonstrates the uncertainty, which is equally distributed over both quadratures. In time evolution the coherent state rotates counter-clockwise around the origin. Coherent and squeezed states were simulated with QuTiP [JNN13].

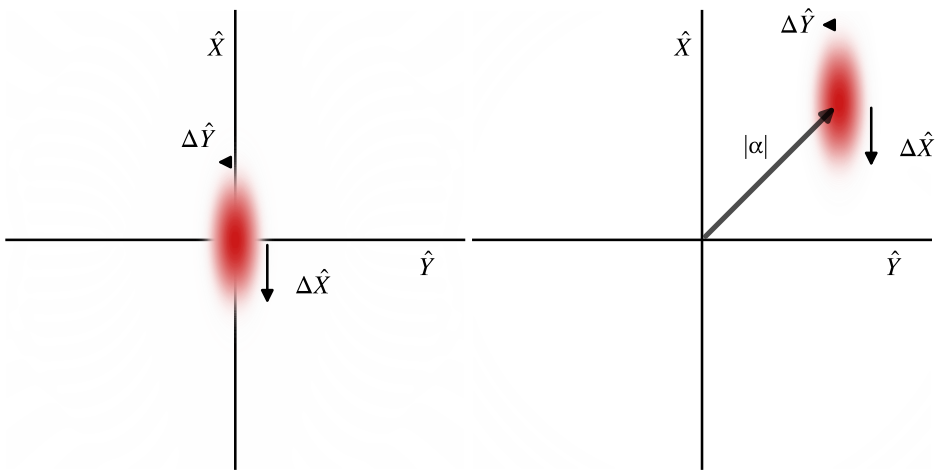

Figure 2.2: Squeezed vacuum (left) and displaced squeezed state (right). The uncertainty gets elliptical, allowing for reduced uncertainty on one quadrature. The squeezing ellipse rotated by the squeezing angle θ.

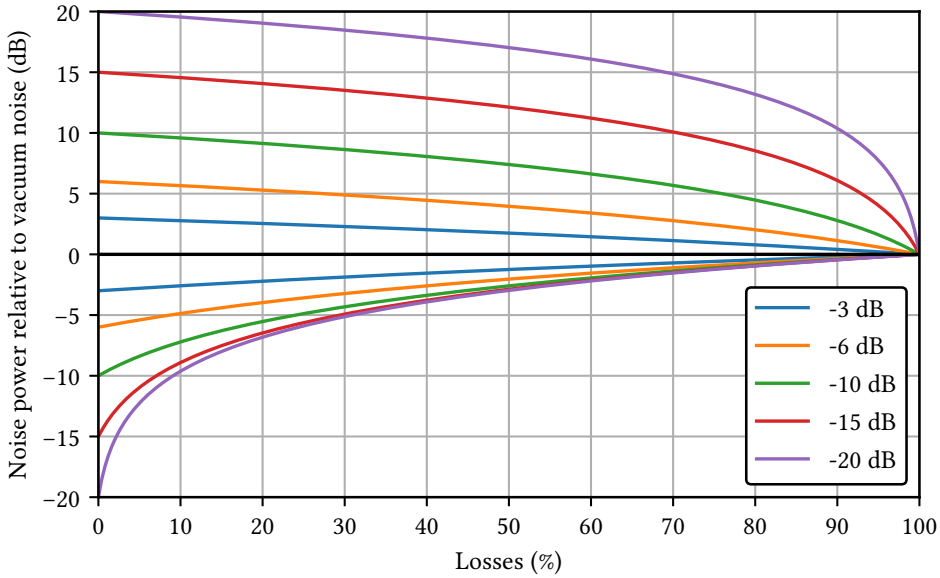

Figure 2.3: Influence of losses on achievable squeezing and anti-squeezing values. Squeezing is much more affected by losses than anti-squeezing.

Simplified with $\theta = 0$ the variances of the quadratures become

$$\left\langle \Delta^2 \hat{X} \right\rangle = \frac{1}{4} e^{-2r} \qquad (2.14)$$
$$\left\langle \Delta^2 \hat{Y} \right\rangle = \frac{1}{4} e^{2r}.$$

Here, it is clearly visible that the quadrature uncertainty $\Delta^2 \hat{X}$ gets reduced with higher squeeze factor r and $\Delta^2 \hat{Y}$ gets anti-squeezed. If $\theta = \pi$ the squeezing will be in $\Delta^2 \hat{Y}$.

2.1.3 Influence of losses on squeezed light

Optical experiments involve losses caused by imperfections, such as optical losses, imperfect mode matching or limited detection efficiency. In case of squeezed states, they not only cause a reduction of amplitude, but also reduced squeezing levels. The behavior can be modeled by overlapping the squeezed state with a vacuum state, as described by

$$\Delta^2 \hat{X}_{\theta,\,\mathrm{loss}} = (1 - L) \cdot \Delta^2 \hat{X}_\theta + L \cdot \Delta^2 \hat{X}_{\mathrm{vac}}\,, \qquad (2.15)$$

with the losses L. The influence on the squeezed variance is much higher than for the anti-squeezed variance, which becomes clear when comparing the numbers. Let the values be normalized to $\Delta^2 \hat{X}_{\mathrm{vac}} = 1$. Then, on higher squeezing levels, the variance for anti-squeezing is much higher than 1 and the variance for squeezing a small number between 0 and 1. Hence, adding loss with the factor L has clearly more influence on the squeezed variance. The influence of losses on both squeezing and anti-squeezing can be seen for multiple initial squeezing levels in figure 2.3.

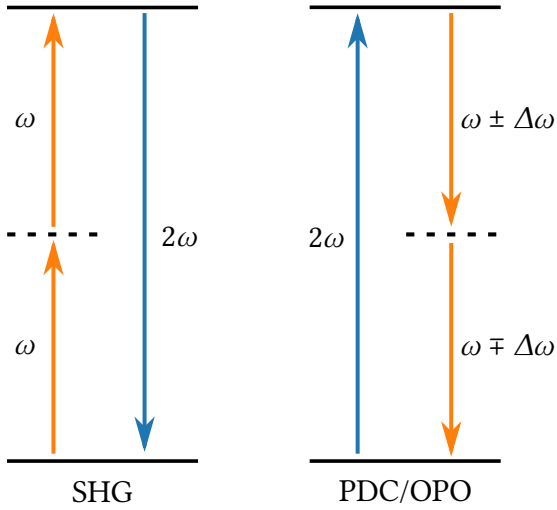

Figure 2.4: Virtual energy levels of the processes second-harmonic generation (SHG) on the left, converting to twice the wavelength, and parametric down-conversion (PDC) on the right, converting to the half wavelength. While the converted wavelength for the SHG process is completely defined by the pump, the $\Delta\omega$ in the PDC process depends on the phase-matching conditions.

2.2 Nonlinear crystals

The polarization $P(t)$ describes the response of an optical material to an applied electromagnetic wave $E(t) = E_0 \cos(\omega t)$. It can be Taylor-approximated

$$P(t) = \epsilon_0 \Big(\chi^{(1)} E(t) + \chi^{(2)} E^2(t) + \chi^{(3)} E^3(t) + \dots \Big), \tag{2.16}$$

with the i-th order susceptibility $\chi^{(i)}$ of a material. Normally the first term is sufficient, describing linear optics. Only in the case of very high E fields or materials with high second (third) order coefficient, the nonlinear terms play a role. If the higher-order terms become relevant, it results in the emergence of new frequencies. For example

$$E^2(t) = \Big(E_0 \cos(\omega t) \Big)^2 = \frac{E_0^2}{2} \Big(1 + \cos(2\omega t) \Big), \tag{2.17}$$

therefore the doubled frequency 2ω appears This process is called second harmonic generation (SHG) and converts the pump light to twice its frequency. Here, two photons of frequency ω combine to one photon of frequency 2ω, while satisfying the energy conservation with the energy being related to the frequency with $E = \hbar\omega$. The process can also be inverted by pumping the crystal at 2ω, which results in parametric down-converted (PDC) light at frequency ω. For parametric down-conversion the converted photons do not need to have the same frequency, but also general cases of difference-frequency generation (DFG) with $\omega \pm \Delta\omega$ are allowed, still conserving the energy. Two types of second-order processes are depicted in figure 2.4. Similar to parametric down-conversion with two different output frequencies, the up-conversion can be driven by two different frequencies, resulting in sum frequency generation (SFG).

2.2.1 Optical parametric oscillation

Optical parametric oscillation (OPO) is commonly used to create tunable infrared lasers [Boy08; Wu+00; Ari+02; PPF11], where the pump light is converted to two different wavelengths: the so called signal is used and the idler thrown away. Obviously, this way the conversion efficiency is limited to $< 50\,\%$. Therefore, we used degenerate optical parametric oscillation

(DOPO), where signal and idler have the same frequency and twice of the conversion efficiency can be reached. Parametric down-conversion can result in bright light (OPO) if driven above optical parametric amplification threshold and in optical parametric amplification (OPA) if pumped below threshold power.

Oscillation threshold

To understand the threshold condition for the generation of bright light, let us assume a simplified case. Signal and idler are degenerate $\omega_s = \omega_i = \omega$ and we have a cavity around the nonlinear crystal, which is resonant to ω with the same reflectivities on both sides $R_s = R_i = R$. Assuming perfect phase matching and a high reflectivity ($1 - R \ll 1$), the threshold condition can be expressed as [Boy08; GM65]

$$e^{2gL} - 1 = 2(1 - R)\,, \tag{2.18}$$

with the crystal length L and the gain

$$g = 2\omega n_s d_{\text{eff}} A_p\,,$$

where n is the refractive index of the crystal for signal and idler, d_{eff} the effective nonlinearity of the crystal and A_p the amplitude of the pump beam. For the realistic case of the single-pass gain being $2gL \ll 1$, the condition can be simplified to

$$gL = 1 - R\,. \tag{2.19}$$

Phase matching

For an optimal nonlinear interaction, the fundamental and harmonic light fields need to have a fixed phase relation while propagating through the crystal:

$$\Delta k = k_s + k_i - k_p = 0$$

Once having a significant phase mismatch Δk, the efficiency of the nonlinear process rapidly decreases. If the refractive index n is different for the fundamental and harmonic light fields, the wavefronts diverge while passing the crystal. The refractive index of typical optical materials increases with frequency, wherefore the requirement $n(\omega) = n(2\omega)$ usually can not be satisfied. In some cases birefringence or a strong temperature-dependency can be exploited to achieve phase matching, but that is not possible if the material is isotropic or if the conversion occurs between two waves of the same polarization [Boy08] (where the d_{33} coefficient is used) as we do in the cavities.

Another commonly used way to obtain high conversion efficiencies even though the refractive indices of fundamental and harmonic are not equal is quasi phase matching. Here, one accepts the drifting apart of the wavefronts, but inverts the conversion process by periodic poling of the susceptibility. Consider the wavefronts at ω and 2ω with slightly different refractive indices. After passing the coherence length, the wavefront of ω starts having a phase lead of $\geq \pi$, which destructively interferes with the light already converted. This case is depicted in

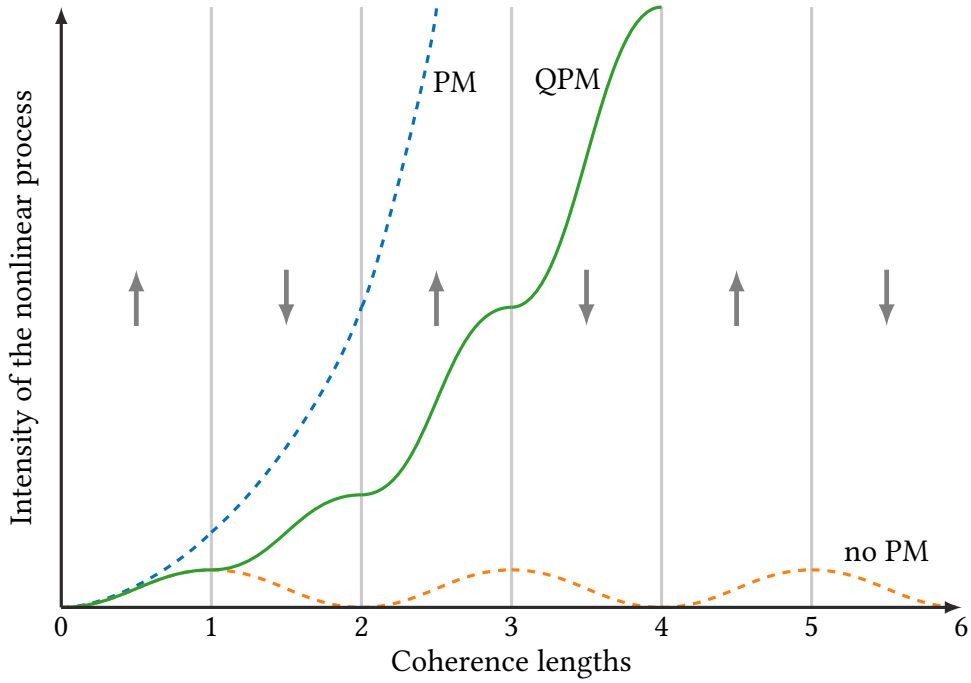

Figure 2.5: Comparison of intensity growth in nonlinear crystals. Optimal response for perfect phase matching (PM), response with phase mismatch, caused by uncompensated phase drifts (no PM), and response for quasi phase matching achieved by periodic poling of the nonlinearity (QPM). The periodic poling achieves a slightly lower nonlinear effect than with perfect phase matching, but allows to compensate for intrinsic differences of the refractive index between wavelengths. (Figure taken from Maik Schröder [Sch19].)

figure 2.5 (*no PM*), where the resulting light field vanishes after two coherence lengths. On the contrary, if the direction of the susceptibility in the crystal is inverted after one coherence length, the conversion again starts to increase, as shown in the (*QPM*) curve. In this way, quasi phase matching can be achieved with apart drifting wavefronts. The resulting effective nonlinearity is lowered by a factor of $2/\pi$ compared to perfect phase matching [Fej+92], which can be seen when comparing to the (*PM*) curve.

Bistability of degenerate operation

Degenerate OPOs (DOPO) have two possible phase states 0 and π of the converted light; this effect is called optical bistability [Nab+90; RY92; Lug+88]. When the oscillation starts, the phase state is randomly chosen by thermal fluctuations and vacuum noise, which can be exploited to generate quantum random numbers [Mar+12]. Considering figure 2.6, it becomes clear that there are two phase states of the converted light relative to the pump field, which are equivalent but shifted by π. This effect causes an intrinsic instability slightly above threshold, where small disturbances can lead to phase hops. The phase state stabilizes at continuous light fields, if driven clearly above threshold, but an instability remains. This makes DOPOs very sensitive to back-reflections, causing unwanted mode hops.

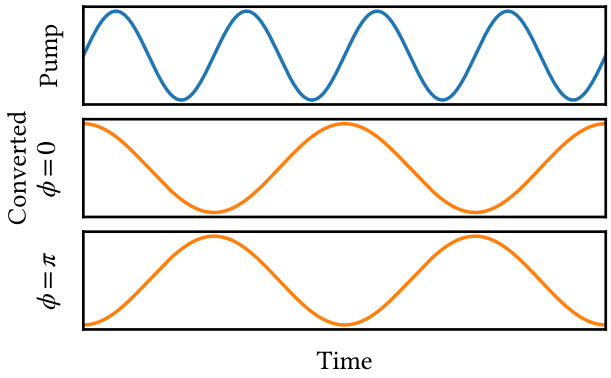

Figure 2.6: Possible phase states $\phi = 0$ and $\phi = \pi$ of degenerate down-converted light fields. When the oscillation starts, vacuum noise randomly determines the phase state.

2.2.2 Generating squeezed states

The second-order nonlinearity can produce parametric amplification, which results in squeezed states if applied to vacuum noise. The Hamiltonian of degenerate parametric down-conversion, pumped with ω_p and converted to signal $\omega_s = \omega_p/2$, is given by [GK05]

$$\hat{H} = \hbar\omega_s \hat{a}^\dagger \hat{a} + \hbar\omega_p \hat{b}^\dagger \hat{b} + i\hbar\chi^{(2)}(\hat{a}^2\hat{b}^\dagger - \hat{a}^{\dagger 2}\hat{b}),$$

with the pump mode b and the signal mode a. As we assume degeneracy, we do not differentiate between signal and idler.

Here, we use the parametric approximation, where we assume that the pump field is a strong coherent classical field and the pump depletion is negligible. Thus, the pump is in a coherent state $|\beta e^{-i\omega_p t}\rangle$ and the operators can be approximated with $\hat{b} \approx \beta e^{-i\omega_p t}$ and $\hat{b}^\dagger \approx \beta^* e^{i\omega_p t}$. When dropping the constant terms, the parametric approximation is

$$\hat{H}_{\text{parametric}} = \hbar\omega_s \hat{a}^\dagger \hat{a} + i\hbar(\eta^* \hat{a}^2 e^{i\omega_p t} - \eta \hat{a}^{\dagger 2} e^{-i\omega_p t}),$$

with $\eta = \chi^{(2)}\beta$. Transforming to the interaction picture [LLM81], the Hamiltonian results in

$$\hat{H}_{\mathrm{I}}(t) = i\hbar\left(\eta^* \hat{a}^2 e^{i(\omega_p - 2\omega_s)t} - \eta \hat{a}^{\dagger 2} e^{-i(\omega_p - 2\omega_s)t}\right).$$

Assuming degenerate operation ($\omega_p = 2\omega_s$), the time-independent Hamiltonian reads

$$\hat{H}_{\mathrm{I}} = i\hbar\left(\eta^* \hat{a}^2 - \eta \hat{a}^{\dagger 2}\right).$$

The corresponding time evolution operator

$$\hat{U}_{\mathrm{I}}(t,0) = \exp\left(\frac{-i\hat{H}_{\mathrm{I}}t}{\hbar}\right) = \exp\left(\eta^* t \hat{a}^2 - \eta t \hat{a}^{\dagger 2}\right) \tag{2.20}$$

$$= \exp\left(\tfrac{1}{2}(\xi^* \hat{a}^2 - \xi \hat{a}^{\dagger 2})\right) = \hat{S}(\xi) \tag{2.21}$$

equals the squeezing operator $\hat{S}(\xi)$ for $\xi = 2\eta t$, as described in equation 2.12. Hence, squeezed light can be produced by nonlinear crystals.

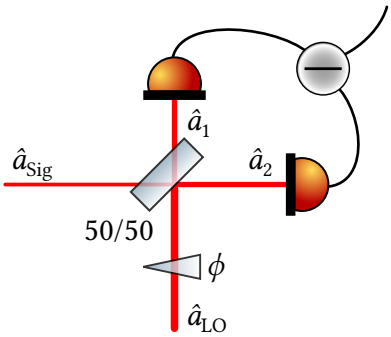

Figure 2.7: Scheme of balanced homodyne detection. The weak signal $\hat{a}_{\mathrm{Sig}}$ is overlapped with the bright local oscillator $\hat{a}_{\mathrm{LO}}$ on a 50/50 beam splitter to get access to phase fluctuations and arbitrary quadrature angles. Both outputs $\hat{a}_1$ and $\hat{a}_2$ are monitored with photodiodes of whose difference is the measurement result. With this measurement setup, the noise of the local oscillator cancels out and the weak signal is linearly amplified with the local oscillator's amplitude.

2.3 Detection of light

Having squeezed light, we need to measure it. Photodiodes allow us to convert light to current, where the light's intensity is linear to the resulting current, at least for perfect detectors.

2.3.1 Balanced homodyne detection

Squeezed light can be detected with a single photodiode, but only in the amplitude quadrature. As photodiodes measure the intensity, amplitude fluctuations become visible while being completely insensitive on phase fluctuations. The phase can be converted to amplitude using interferometric setups, as for example used in homodyne detection. Here, the weak signal beam is overlapped with a bright local oscillator on a beam splitter (see figure 2.7). In the relevant case of *balanced* homodyne detection a 50/50 beam splitter is used. The signal of each output path of the beam splitter is detected with a photodiode, which is subtracted from the other. In this procedure, the correlated noise of the local oscillator cancels out and shifting the phase between the beams allows for the selection of the measurement quadrature. If the local oscillator is much brighter than the signal, the signal gets linearly amplified by the local oscillator's amplitude, as we will see in this section, where I mainly follow Gerry and Knight [GK05].

The relation between input $(\hat{a}_{\mathrm{Sig}}, \hat{a}_{\mathrm{LO}})$ and output $(\hat{a}_1, \hat{a}_2)$ operators is given by

$$\begin{aligned} \hat{a}_2 &= \frac{1}{\sqrt{2}}(\hat{a}_{\mathrm{Sig}} + i\hat{a}_{\mathrm{LO}}) \\ \hat{a}_1 &= \frac{1}{\sqrt{2}}(\hat{a}_{\mathrm{LO}} + i\hat{a}_{\mathrm{Sig}})\,. \end{aligned} \tag{2.22}$$

The detectors measure the intensities $I_1 = \langle \hat{a}_1^\dagger \hat{a}_1 \rangle$ and $I_2 = \langle \hat{a}_2^\dagger \hat{a}_2 \rangle$. Then, the difference between these intensities is

$$\begin{aligned} I_1 - I_2 = \langle \hat{n}_{12} \rangle &= \langle \hat{a}_1^\dagger \hat{a}_1 - \hat{a}_2^\dagger \hat{a}_2 \rangle \\ &= i\langle \hat{a}_{\mathrm{Sig}}^\dagger \hat{a}_{\mathrm{LO}} - \hat{a}_{\mathrm{Sig}} \hat{a}_{\mathrm{LO}}^\dagger \rangle \end{aligned} \tag{2.23}$$

with the number operator $\hat{n}_{12} = \hat{a}_1^\dagger \hat{a}_1 - \hat{a}_2^\dagger \hat{a}_2$. The local oscillator $\hat{a}_{\mathrm{LO}}$ typically is a bright coherent beam, and hence, we assume it to be in a coherent state $|\alpha e^{-i\omega t}\rangle$, with the complex

value $\alpha = |\alpha| e^{-i\psi}$ and amplitude $|\alpha|$. Hence, we get

$$\langle \hat{n}_{12} \rangle = |\alpha| \left(\hat{a}_{\mathrm{Sig}} e^{i\omega t} e^{-i\theta} + \hat{a}^{\dagger}_{\mathrm{Sig}} e^{-i\omega t} e^{i\theta} \right) ,$$

with the phase shift $\theta = \psi + \pi/2$. As the signal field is derived from the same laser, we can set $\hat{a}_{\mathrm{Sig}} = \hat{a}_{\mathrm{Sig},0} e^{-i\omega t}$ and get the expectation value

$$\langle \hat{n}_{12} \rangle = 2|\alpha| \langle \hat{X}(\theta) \rangle ,$$

with

$$\hat{X}(\theta) = \frac{1}{2} \left(\hat{a}_{\mathrm{Sig},0} e^{-i\theta} + \hat{a}^{\dagger}_{\mathrm{Sig},0} e^{i\theta} \right)$$

being the quadrature at angle θ. Now, we can choose the angle θ with the maximum squeezing by shifting the phase of the local oscillator. The balanced homodyne detection approximation assumes the local oscillator to be much stronger than the signal. For noise measurements the variances is of particular interest and is given by

$$\langle \Delta^2 \hat{n}_{12} \rangle = 4|\alpha|^2 \langle \Delta^2 \hat{X}(\theta) \rangle .$$

Balanced homodyne detection allows for highly sensitive measurements, limited by quantum noise of the light. The ability to scan all quadratures allows the measurement of weak beams, such as squeezed vacuum. To achieve such sensitivities, there are important requirements to fulfill: The beam splitter's angle has to be properly adjusted to provide 50/50 balancing. Both incoming beams have to overlap nearly perfectly on the beam splitter, which is measurable with the visibility

$$V = \frac{I_{\mathrm{max}} - I_{\mathrm{min}}}{I_{\mathrm{max}} + I_{\mathrm{min}}} . \tag{2.24}$$

Here, I_{min} and I_{max} are the light intensities detected at the minimum and maximum of the interference fringe, respectively. Limited quantum efficiency of the photodiodes has a similar effect as a low visibility and is, therefore, also a relevant parameter. Furthermore, low photodiode noise is required, as the uncorrelated noise of the photodiodes does not cancel out in the subtraction. Excellent photodiodes are mandatory to measure high squeezing values. The next section examines the obstacles in the development of such detectors around 2 µm.

2.3.2 Limitations of InGaAs photodiodes

In squeezing experiments at infrared wavelengths usually InGaAs photodiodes are used, as they can reach high quantum efficiencies of more than 99 %, while having low dark current and noise levels [Vah+16]. InGaAs photodiodes are typically sensitive to around 1700 nm, which is appropriate for the commonly used wavelengths of 1064 nm and 1550 nm. Obtaining a high quantum efficiency and low dark noise becomes intrinsically difficult for higher wavelengths due to the low photon energy, resulting in a smaller gap to the temperature-depending noise levels. More indium doping can extend the sensitivity of InGaAs photodiodes up to 2.6 µm. But that results in lattice mismatch between the InGaAs layer and the InP substrate and limits the achievable thickness of the active layer [Gen+92]. The lattice mismatch is a source of high dark current and $1/f$ noise, worsening the relation between photon energy and dark noise [MZL88].

The achievable quantum efficiency depends on the absorption coefficient and the thickness of the active layer, which is limited by the critical thickness [Gen+92], where the semiconductor quality degrades significantly. High layer thickness leads to a recombination of free electrons and reduced quantum efficiency. This effect can be avoided by increasing the reverse voltage (at the cost of a rapid increase of the dark current). An overview of InGaAs photodiodes around 2 µm is described by Briggs et al. [Bri+19]. Even though, it is possible to create InGaAs photodiodes with high quantum efficiency using a buffer layer of AlInAs accounting for the lattice mismatch [Mos+86]. Here, a quantum efficiency of remarkable 95 % could be achieved with a dark current of only 35 nA, but those photodiodes are not commercially available.

To sum up, extending InGaAs photodiodes to 2 µm with excellent properties for interferometry is challenging. Other types of photo detectors might be an option, such as the currently most promising HgCdTe detectors [Adh+20]. But as of now, appropriate photodiodes for next-generation gravitational-wave detectors around 2 µm are not yet available. That mainly limits the achievable squeezing levels to significantly less than 10 dB. We tested different commercially available photodiodes, but except for the two detectors that we used, no other photodiode was close to a quantum efficiency of at least 90 % (section 4.2).

3 | Conversion of bright coherent states from 1064 nm to 2128 nm

The first major step of my experiment was the wavelength-doubling of our laser light in a nonlinear cavity. The approach employs laser sources at 1064 nm as currently used in gravitational-wave detection and converts the light via degenerate, cavity-enhanced optical-parametric down-conversion to 2128 nm. This nonlinear process is known to retain the stability and noise properties of the pump [Eck+91; Nab+90], allowing to fully take advantage of the already optimized NPRO lasers.

So far, optical-parametric oscillators have been used e.g. to provide tunable continuous-wave laser sources [Bos+96], wavelength conversion of pulsed lasers [ANR04], or even to generate quantum random bits, exploiting their inherent bistability [Mar+12]. Major parts of this chapter were published in Optics Letters [Dar+20a].

For this project I supervised Maik Schröder in his Master thesis [Sch19] with whom I built the setup. He changed the cavity design to have a fixed airgap (which I optimized as shown in section 3.1.2), designed and built the confocal cavity which is used to detect degeneracy of the output wavelengths, and made a first investigation in the system characteristics. For degeneracy monitoring we installed a confocal cavity, as described in section 3.2.2.

In the following, I characterized our setup together with Julian Gurs (who was the next Master student I supervised) to validate the performance required for interferometric light sources in gravitational-wave detection. This includes temperature tuning behavior of the oscillation wavelength, conversion efficiency, interferometric visibility, and power stability.

3.1 Experimental setup

The experimental setup (figure 3.1) for the following measurements mainly consists of the nonlinear cavity which is pumped by a 1064 nm NPRO laser and diagnostic devices. In the output were different diagnostic devices used for the measurements, such as photodiodes, a confocal cavity, a thermal powermeter and a spectrometer. For the visibility measurement, we used a second nonlinear cavity, intended to be used for the generation of squeezed vacuum, to create a second bright beam at 2128 nm to have two independently converted beams for the interference measurement.

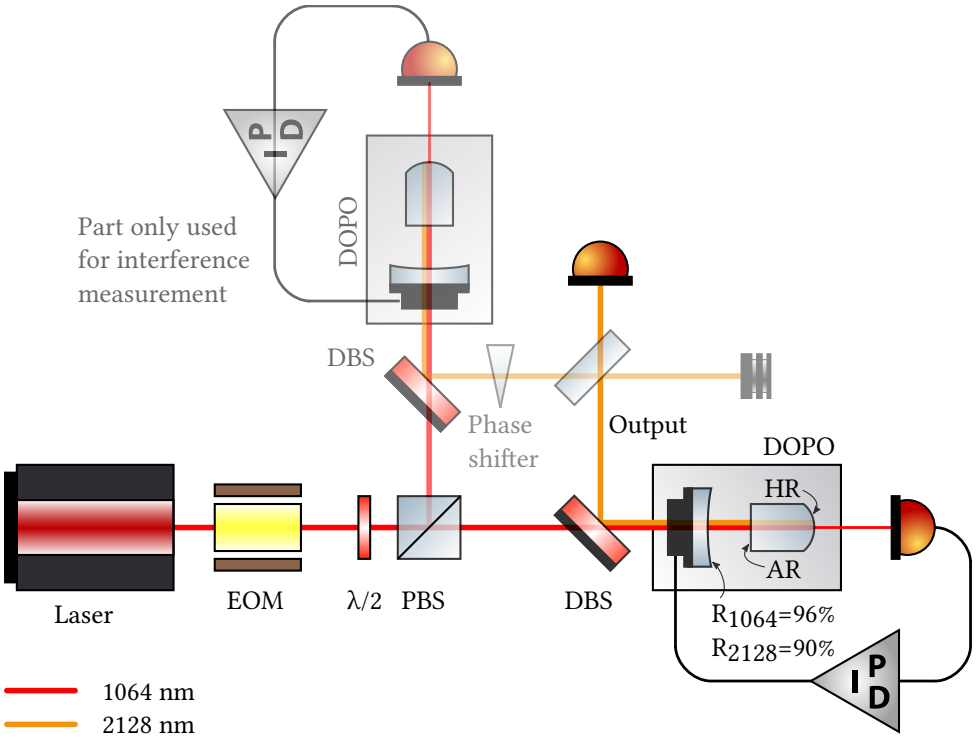

Figure 3.1: Simplified schematics of the 2 µm generation and analyzation setup. With a combination of half-waveplates and polarizing beam-splitters (PBS) the pump powers for both cavities can be individually adjusted. The converted light was split from the pumping beam with a dichroic beam-splitter (DBS). For diagnostic purposes, the converted light could be sent towards a spectrometer and confocal cavity. A second, identical DOPO was installed together with a phase shifter and 50/50 beam-splitter for the interference measurement (section 3.4).

3.1.1 Laser preparation

The 1064 nm pump light is generated by a nonplanar ring oscillator (NPRO) [KB85] Nd:YAG laser as currently used in gravitational-wave detectors [Fri+20]. Those lasers have a high beam quality ($M^2 < 1.1$) and a very narrow spectral linewidth of 1 kHz, which corresponds to a coherence length of 1 km. Our model has an output power of 2 W, whereas gravitational-wave detectors use higher powers. The divergent beam of the laser is collimated with a lens and the polarization is cleared with $\lambda/2$ and $\lambda/4$ plates to maximize the power through the optical isolator. The beam is distributed to both cavities using a polarizing beam splitter (PBS) and a $\lambda/2$ plate. Both cavities additionally have their own upwards directed PBS to individually control the power and to provide clear s-polarization.

The outcoming beam of the NPRO is slightly elliptical (figure 3.2), which is not corrected. Both mode matchings of the cavities are affected by the ellipticity, but the power losses are not relevant, here.

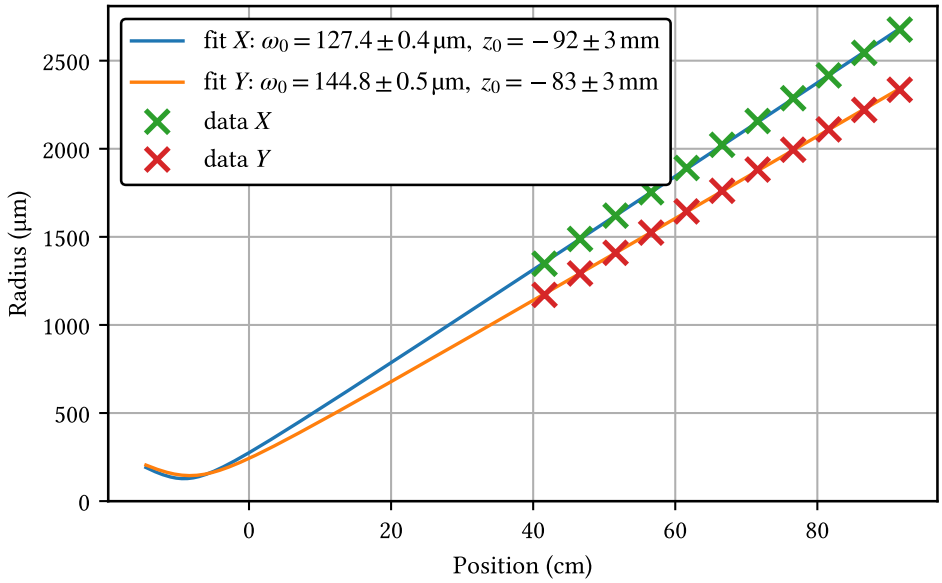

Figure 3.2: Mephisto beam shape. The waist of the divergent beam is inside of the laser, the beam is slightly elliptical. It was collimated with a $r = 100$ mm lens.

3.1.2 Nonlinear cavities

Core of the experiment are two nonlinear cavities, which are used for optical parametric oscillation to produce light of half of the frequency (above threshold) or produce squeezing (below threshold). Both cavities are built identically, only the pump power defines their specific role. The optical resonator is between the coupling mirror and the high-reflective (HR) coated curved end of the crystal (figure 3.3). That way, only one anti-reflective (AR) surface is in the cavity, which reduces the intracavity losses. Compared to a monolithic cavity, we have the advantage to lock it with a fast piezo and to being able to optimize the system for every wavelength in the region of 2128 nm. The design of the nonlinear cavity is based on a design of Axel Schönbeck [Sch18] and optimized for our purpose.

To distinguish the slightly differing nonlinear crystals, I use the same numbering as in the laboratory.

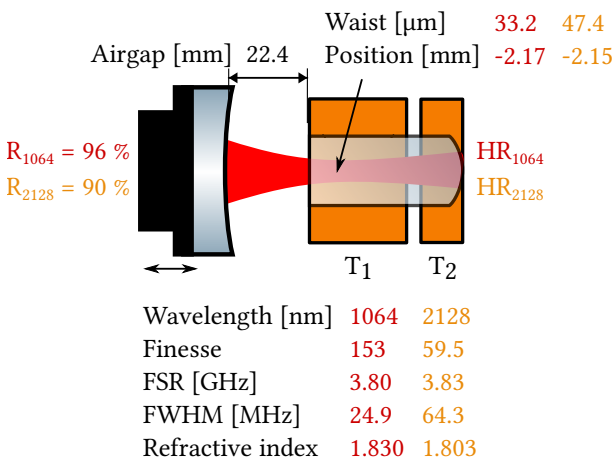

Figure 3.3: Nonlinear cavity scheme. The resonator between the coupling mirror and the end surface of the crystal is length-controlled using a ring-piezo on the coupling mirror. The phase matching with the optical length of the periodically poled domains is controlled with the temperature T_1. T_2 is used to provide resonance for both wavelengths at the same time.

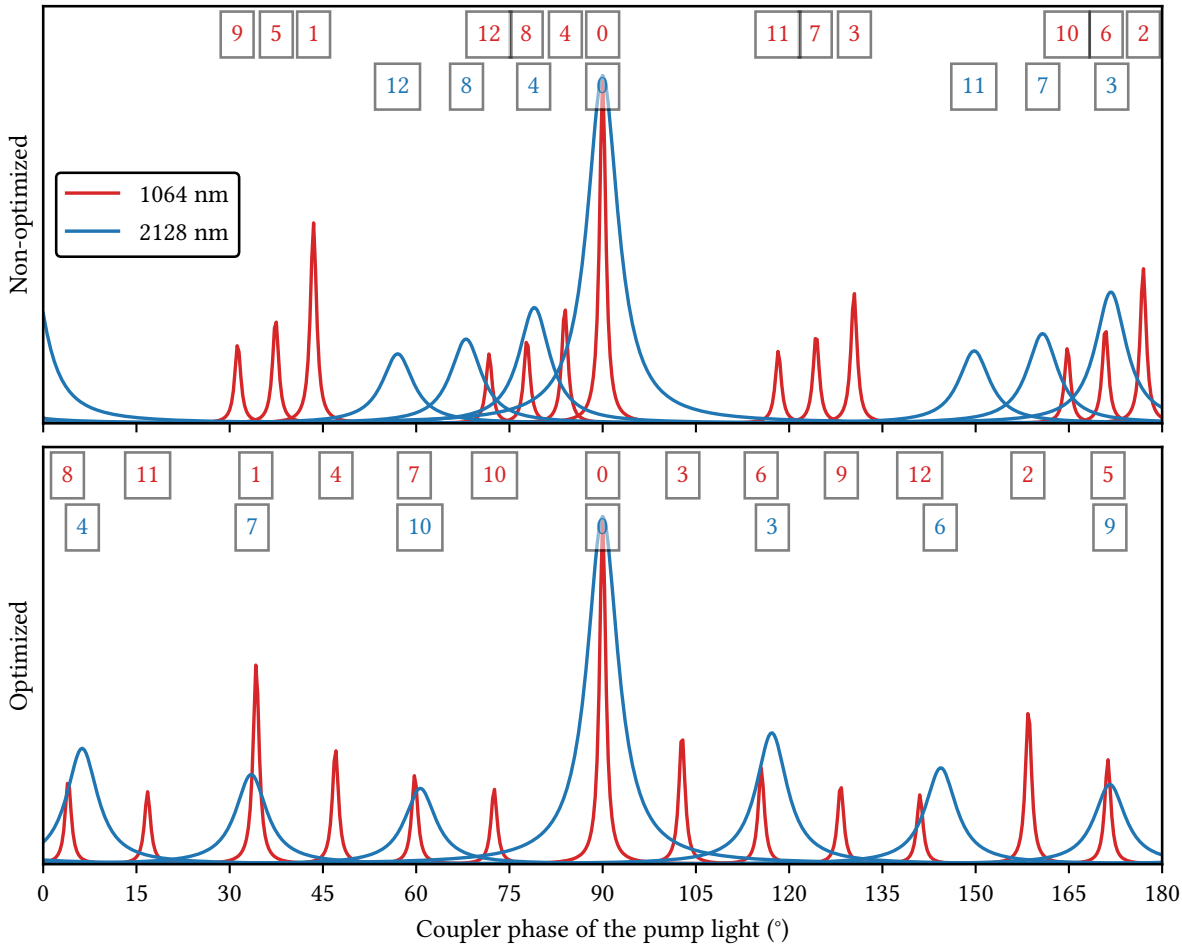

Figure 3.4: Airgap before (23.5 mm, arbitrary value) and after optimization (22.4 mm), with the corresponding order $m+n$ of the Gaussian TEM_{mn} modes. The modes up to 12th order of both wavelengths are spread equally over the coupler phase to make the cavity work as a mode cleaner. Similar to a triangular mode cleaner the vertical and horizontal modes are non-degenerate; in this case due to crystal anisotropy, but that effect is not included in the calculation. In the non-optimized case, the first 12 Gaussian modes highly overlap, making it difficult to select the TEM_{00} mode without contribution of other modes. With the optimization the main mode can be resonant while having high suppression of the other modes. For the calculation, the amplitude of the modes was chosen to be $1/\sqrt{m+n+1}$ to make the decreasing influence of higher modes visible.

General cavity properties

To get to know the optical system and to optimize it for minimized overlap of Gaussian modes, I simulated the cavity with Finesse/PyKat [BF14; BF17]. They are individually calculated for 1064 nm and 2128 nm, ignoring the nonlinearity, as Finesse is not capable of performing nonlinear calculations. The main parameter to optimize was the airgap between the AR side of the crystal and the coupler. Previously, the distance was adjustable, but we wanted to have it fixed to reduce one optimization parameter in the experiment. The cavity is stable with an airgap between 20 mm and 26.4 mm and should be operated somewhere in the middle of this range, where the waist is around its maximum. In this range, the airgap was optimized for a

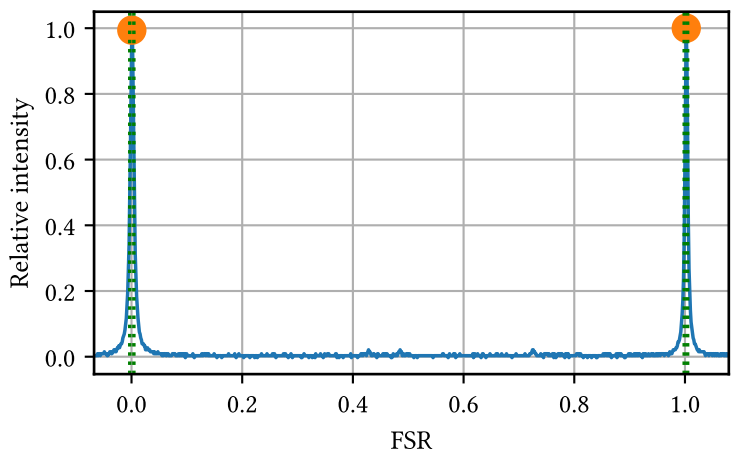

Figure 3.5: Rough finesse measurement at 1064 nm to verify the simulation, scanned with 30 Hz. Finesse of the left peak: 126, right peak: 167, mean value: 147. The differences are mainly caused by piezo nonlinearity.

good distinction of the Gaussian modes (figure 3.4) up to order 12, i.e. all transverse electromagnetic (TEM) modes TEM_{mn} with $m + n \leq 12$. In the cavity simulation all permutations of the same order $m + n$ are degenerate and not distinguishable in the scan. That is not true in a real crystal as it has different refractive indices in vertical and horizontal direction, wherefore an mn mode is distinguishable from an nm mode ($m \neq n$).

To verify a part of the simulation results, the finesse of the cavities was measured with a scan over one FSR of the pump beam. For both cavities it was in the expected range, as can be seen in figure 3.5. When scanning over a whole FSR, the nonlinearity of the piezo becomes significantly high, which leads to an underestimation of one peak and an overestimation of the other peak. Hence, the real finesse is somewhere between and the mean value of both peaks is rather close to a finesse of 150.

Nonlinear cavity properties

The nonlinear properties of the cavity are defined by the crystal, which is made of periodically poled potassium titanyl phosphate (PPKTP). As explained in section 2.2.1, pump and the two converted fields, signal and idler, have to be phase matched. The optical length of the periodically poled regions is controlled with the temperature T_1, which mainly changes the refractive index and slightly affects the (domain-) length of the crystal. To make all wavelengths resonant, the curved end of the crystal can also be temperature controlled with T_2 and the coupler is held on resonance of the pump with a piezo. The expected power P_{out} of the converted light can be calculated analytically [BSM95; Mar+01]

$$P_{\mathrm{out}} = 4\eta_{\mathrm{max}} P_{\mathrm{th}} \left(\sqrt{\frac{P_{\mathrm{in}}}{P_{\mathrm{th}}}} - 1 \right), \tag{3.1}$$

where η_{max} is the conversion efficiency at the maximum, P_{th} the threshold power where the conversion begins and P_{in} the input power. The threshold power P_{th} implicitly includes a variety of contributions, such as the strength of the nonlinearity, the beam size and the power buildup in the cavity which is derived from the finesse. To estimate the expected output power, I used the nonlinear cavity simulator NLCS [Las10] with the resulting FSR, waist and waist position from the Finesse simulation. The closest literature value for the estimation was $d_{33} =$

$\frac{\pi}{2} d_{\text{eff}} = 10.05\,\text{pm/V}$ for the transition 1984 to 992 nm [Man+18] and is expected to be a bit lower at higher wavelengths. In our real system, the effective nonlinearity is slightly lower than the estimated value, as will be discussed in section 3.3.

3.1.3 Coupling efficiency measurements

The coupling efficiency of the desired TEM_{00} mode into a cavity is usually measured by summing up the amplitudes of all minor cavity peaks and dividing by the main mode's amplitude. One therefore needs to scan the phase of the coupling mirror over a whole FSR and include many small peaks using an oscilloscope. To make the measurement faster and more reproducible, I automated the calculation process (`openqlab.analysis.cavity.modematching`) to detect the two main peaks and all smaller ones in between. For the differentiation between very small peaks and noise, a parameter can be tuned which adjusts the threshold. The result of the script can be seen in figure 3.6.

There are two systematical errors, which can lead to an overestimation of the coupling efficiency: Especially if the finesse of the cavity is low, additional modes can be hidden in the width of the main mode (e.g. the non-optimized modes at 2128 nm in figure 3.4). Other than that, modes with relevant amplitude can be hidden by noise, where the digitization noise is often dominant. Often only having 8 bit resolution, oscilloscopes can lead to significant bit noise when the main peaks are included. When the input range is selected appropriately, the peak height U_{max} will internally be close to the maximum possible integer number of $+127$ or -128, while being around 0 for all the minor modes. Due to the signed numbers of the internal representation, only 7 bit are accessible and thus, the minimal detectable value change of one bit flip is $U_{\text{max}}/2^7 \gtrsim 0.008\, U_{\text{max}}$. When taking into account, that a mode height has to be more than a bit to distinguish from bit noise, the lowest detectable mode is greater than one percent. Therefore, it becomes mandatory to increase the resolution of the minor peaks if the coupling efficiency is only some percent below 100 %. One solution is to limit the scanning range of the coupler, such that the main peaks are closely cropped. Now, a more sensitive input range can be selected without the analog-digital converter of the oscilloscope being saturated. Such

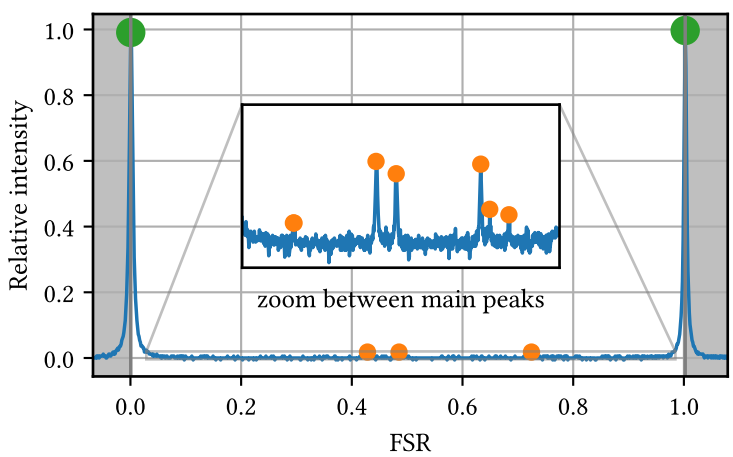

Figure 3.6: Mode matching of the squeezer. The scan over a full FSR including the main peaks misses some of the smaller unwanted peaks of higher modes due to limited resolution of the oscilloscope. Therefore, if the main peaks are excluded, a more precise (and lower) mode matching value can be found. Mode matching full scan: 94.6 %, zoom: 93.9 %. The script that was used for this automated mode matching evaluation has been included to `OpenQlab` [PDS] to make it also available to other users.

a measurement can be seen in the inset figure; to calculate the mode matching efficiency, the voltage of the main peaks has then to be recorded and entered manually.

The algorithm is implemented as follows, starting with a preparation of the data. The offset is set to zero by using the median value. Using the median is an easy solution providing good average values for non-resonance if the finesse is sufficient. If the median offset detection is not sufficient, a value can be provided manually. If the peaks yield negative values, the sign is flipped to calculated with unified data. The global maximum is used as preliminary peak height of the main mode U_{max}.

In the main algorithm, the SciPy [Vir+20] peak detection `find_peaks` returns all peaks surpassing the threshold, using the provided relative prominence parameter. The main mode has to be returned exactly two times, which is identified by requiring at least 90 % of the maximum's peak height for the second occurrence of the main mode. Finally, the coupling efficiency is calculated by dividing the sum of all minor peak heights by U_{max} using the average value of both main peaks.

As the measurement including the peaks of the main mode only provides an imprecise result, the script can also be run with the cropped data. Then, the voltage of the main mode U_{max} has to be provided by the user. To get feedback which modes have been found, the peaks are marked in a generated plot, as can be seen in figure 3.6.

3.1.4 Control scheme

Both nonlinear cavities need to be actively stabilized to hold them on resonance. We use the Pound-Drever-Hall locking scheme [Dre+83] for that purpose, as it provides a clear and robust error signal (depicted in figure 3.7). Here, an EOM is used to modulate phase sidebands at 28 MHz onto the laser beam. A photodiode with an integrated demodulation circuit is used

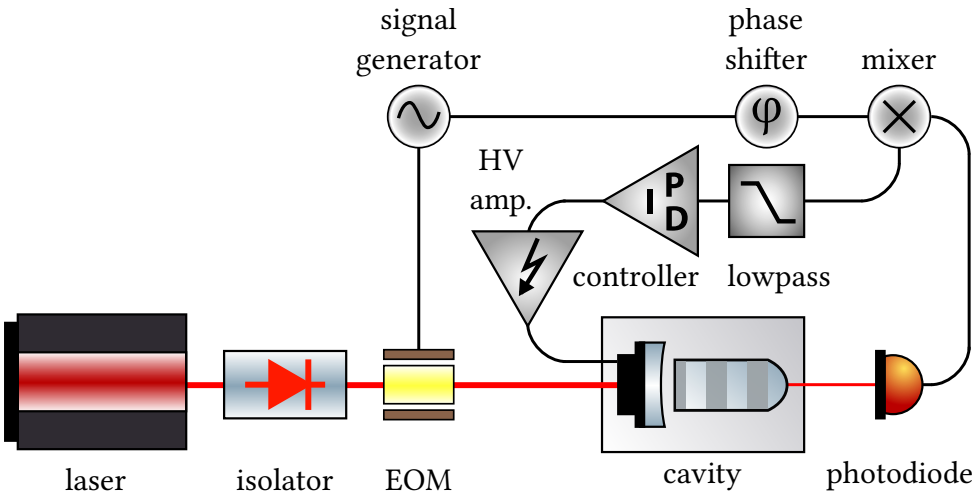

Figure 3.7: Pound-Drever-Hall control scheme of the experiment. A 28 MHz RF signal is producing phase sidebands on the light with the EOM. The phase information is demodulated by mixing the transmitted signal of the photodiode the same RF signal, combined with a lowpass filter. Using the resulting error signal, the controller (NQontrol) calculates the feedback for the piezo of the coupling mirror.

in transmission of the cavity to extract the error signal. This way, an error signal is created which essentially is the derivative of the intensity on the photodiode, making it possible to distinguish if an off-resonant cavity is too long or too short. For the length stabilization I used a self-built digital control system, as described in [Dar+20b] and in section 5.2, which sends a high-voltage amplified feedback signal to the piezo of the coupling mirror.

Now, having a controllable cavity with an error signal, the lock can be optimized for low noise and high control bandwidth using a variety of digital filters (for details, see section 5). For optical cavities, the achievable bandwidth is mainly limited by piezo resonances as they occur around 10 kHz in our nonlinear cavities. Strong filter optimization for high control bandwidth and low noise (optimal control) inherently leads to reduced robustness [Bec05] if system parameters slightly change, which is observable in oscillations if the laser power is changed as it effectively changes the system gain. Therefore, I optimized the filters for robustness for daily lab work where often huge changes of pump power are necessary. Further details on the transfer function optimization can be found in section 5.2.3.

As the nonlinear effect of the crystals depends on the effective optical domain length, their temperatures have to be precisely controlled. For reliable operation a temperature stability of 10 mK is required. The temperatures are controlled with a modular digital control system using peltier elements for heating and cooling. Each cavity is stabilized with one satellite, providing control for both required temperatures. The self-built system, based on a commercial temperature controller, is described in section 5.3.

3.2 Temperature dependencies

Wavelength-doubling via degenerate optical-parametric conversion requires precise matching of the periodically poled domain lengths of the crystal and of the optical cavity length for both the pumped and converted wavelength. The temperature can be used to fine-tune the phase matching in the crystal by adjusting the domain length and mainly the refractive index. The resulting optical domain length defines to which wavelengths the input beam will be converted and thus, whether degeneracy between signal and idler can be reached. To characterize the 2 µm light source and its behavior, we measured how the performance of the OPO depends on the temperature of the crystal.

3.2.1 Output wavelength versus phase matching temperature

Tuning the crystal temperature T_1 (of the larger crystal region, see figure 3.3) varies the wavelengths of the signal and idler beams, as it influences the phase-matching condition of the nonlinear crystal. The main effect results from the temperature-dependent refractive index, while the thermal expansion has a relatively small contribution [SSD16]. Figure 3.8 shows how the wavelengths of signal and idler depend on the temperature, measured with a spectrometer (Bruker Equinox 55). Our measurement shows the expected temperature dependency near degeneracy, $\Delta\omega = \eta\sqrt{T - T_0}$ [GM65], where $\Delta\omega$ is the difference in frequency between signal and idler and η a system-specific constant. Only in a small temperature region degeneracy could be reached, requiring a fine tuning of the phase-matching temperature.

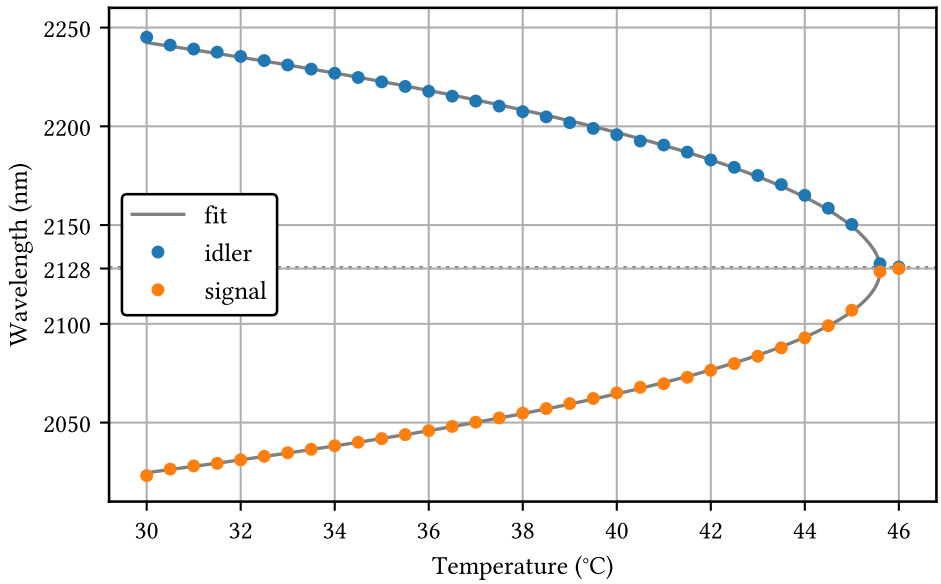

Figure 3.8: Measured signal and idler wavelengths versus crystal temperature ($T_1 = T_2$). The temperature of degeneracy is about 45.1 °C for this crystal. Below this temperature the difference between signal and idler wavelengths increases. At degeneracy the output power drops quickly when the temperature was further increased and the conversion stopped completely at temperatures exceeding 46 °C.

When increasing the crystal temperature, the output power of the converted light stays roughly constant up to the point of degeneracy. Above this point, the output power quickly drops as energy conservation and phase matching condition could no longer be satisfied simultaneously.

3.2.2 Detection of degeneracy of signal and idler modes

As degeneracy is a requirement for the experiment, it has to be monitored continuously. Due to the low usability of our old spectrometer and its limited resolution, a spectrometer measurement is not appropriate for permanent monitoring of degeneracy. Hence, we designed a confocal cavity (figure 3.9). In a confocal cavity, all even and odd resonator modes are degenerate, meaning that there is one peak of indistinguishable even modes and one of odd modes. The advantage here is, that a perfect mode matching to the TEM_{00} mode is not necessary and it can even be placed at an angle to avoid back reflections. Now, if the incoming beam contains two different wavelengths, four peaks per free spectral range will be visible, whereas in the degenerate case only two (one for even and one for odd modes) resonances will be present. An important detail is that the FSR of the confocal cavity must not be a multiple of the nonlinear cavity's FSR, because in this case, non-degenerate states would stay undetected.

In the latest setup the confocal cavity was placed behind a PBS in a side arm and used for continuous monitoring of degeneracy. For most of the beam optimization of the converted light, it is important to ensure degeneracy, as the coatings are slightly wavelength dependent. In the case of the 50/50 beam splitter, the balancing changes depending on the current mode of the light.

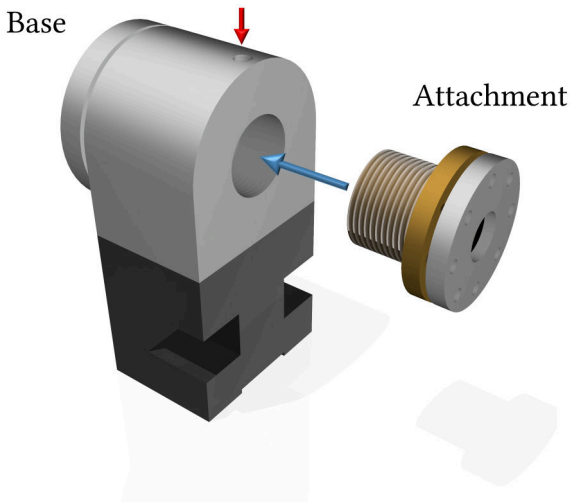

Figure 3.9: Confocal cavity to detect degeneracy. Details on design and behavior of the cavity can be found in [Sch19]. Figure created by Maik Schröder.

3.2.3 Output powers versus crystal temperatures

For better understanding of the crystal's tuning behavior, both temperatures were scanned while recording the power of the converted light with a photodiode (figure 3.10). Both temperatures were scanned downwards with a step size of 100 mK, where T_2 was in the inner loop, i.e. for each temperature T_1 the temperature T_2 was scanned from 40 °C to 20 °C. The measurement was taken after a settle time of 1 s together with an actual temperature measurement, causing the small deviations from the 0.1 K grid. The crystal was pumped only slightly above threshold power to make the influence of the phase-matching visible. Improved phase-matching reduces the threshold power and thus results in higher conversion in that region.

The result for crystal 3 can be seen in figure 3.10, which is another crystal than in the measurement of figure 3.8 and therefore causing different phase-matching temperatures. Temperature T_1 of the crystal had the main influence, defining the optical distance of the periodic poling. The changing phase-matching conditions caused a periodic modulation of the converted power (and thus of the effective conversion threshold). Degeneracy could be reached in the yellow region on the right, next to the diagonal. Figure 3.11 in detail shows where in this region the conversion can be degenerate. At temperatures above the region where degeneracy can be reached, the conversion completely stops.

3.2.4 Finding degeneracy

While the down conversion to *some* combination of frequencies is stable and robust, finding a stable region of degeneracy was the only unreliable aspect of the experiment. There were days when the degeneracy was the most stable mode and days when it was almost impossible to obtain degeneracy with the previous temperatures. The laboratory was permanently temperature and humidity controlled, but on some days the air conditioning did not work as intended and if temperature or humidity changed, the crystal temperatures had to be adjusted. We made multiple such temperature maps with different as well as equal laser wavelengths. For higher laser wavelength, the crystal temperatures have to be increased. With constant en-

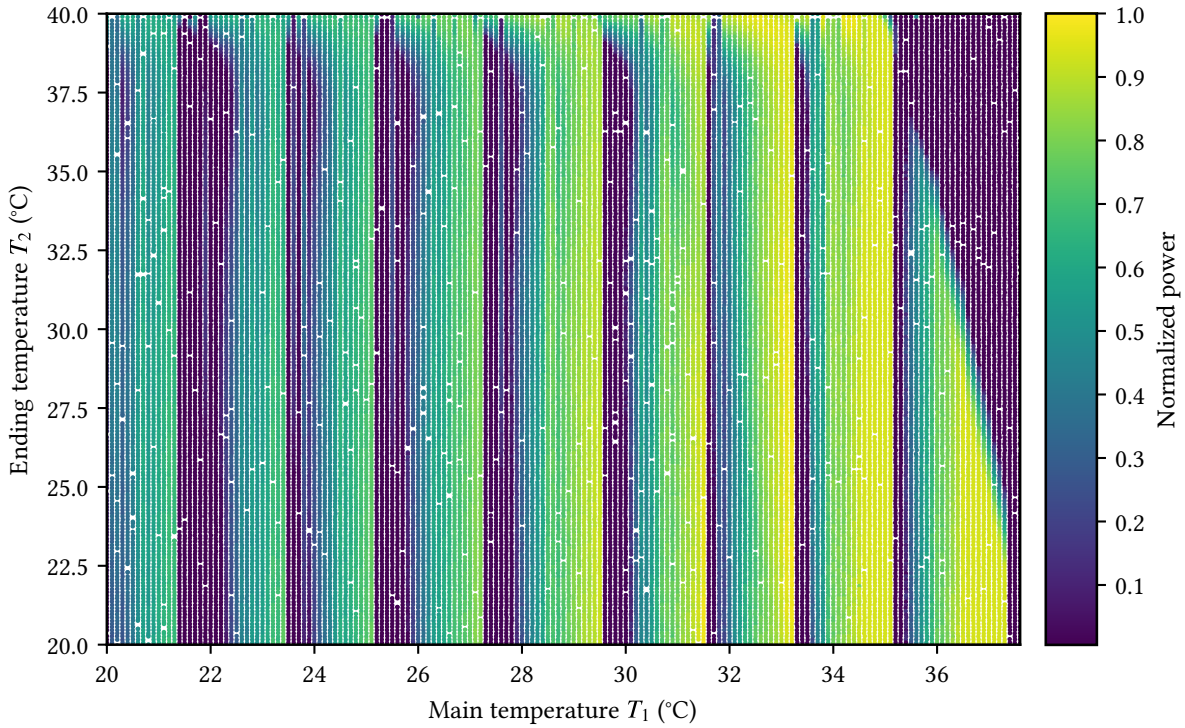

Figure 3.10: Power of the converted light depending on both crystal temperatures (crystal 3) to get an overview of the temperature landscape. The OPO was pumped slightly above the threshold power to increase the visibility of small system changes. Similar to crystal 2 in figure 3.8 degeneracy can be reached in the area right at the right border. In the region at the top right the power completely drops even on high pump powers. Temperature T_2 can slightly compensate T_1, but with a much smaller influence, as can be seen at the diagonal near $T_2 > 35\,°\mathrm{C}$.

vironment conditions, the phase-matching temperatures are reproducible and a temperature map can be reused.

The cavity is only resonant if the length L is a multiple of half of the wavelength

$$L = n\frac{\lambda}{2};$$

which means, when scanning the cavity only every second peak of the pump light is resonant to a degenerate peak of the converted light. The peaks are not directly distinguishable and the only way to verify the correct peak was to detect if it was possible to obtain degeneracy on this cavity resonance. To do so, it was necessary to operate the DOPO at phase-matching conditions and to force mode hops while observing degeneracy. If degeneracy was not reached, the other conversion peak usually succeeded. This procedure took typically some minutes. Afterwards, the correct peak could be held continuously on resonance as long as the environment conditions did not change significantly.

To understand the behavior of the degenerate mode, I created a 2D map and scanned both crystal temperatures downwards (figure 3.11) in a subarea of the power map (figure 3.10). Similar to the previous measurement, for each T_1 the temperature T_2 was scanned downwards. Here, the step size was 200 mK and I inserted the output power manually, if the beam was degenerate, increasing the settle time to a few seconds. Data points were only taken if the converted

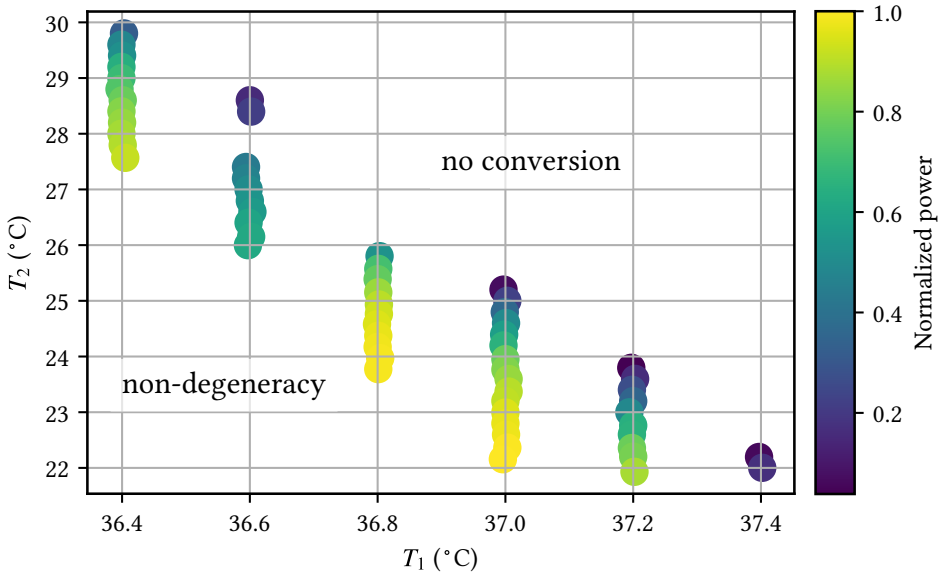

Figure 3.11: Map of degenerate converted light power, scanned with decreasing temperatures (crystal 3). Only in the case of degeneracy (monitored with the confocal cavity) the converted power was recorded. The output power increased with lowered temperature, but the degeneracy became more likely to be lost. At 36.6 °C the missing points are not supposed to be a real effect, but only randomly lost degeneracy.

light was degenerate. At high temperatures, no conversion occurs. When the temperature is lowered, the power in the degenerate mode increases. At even lower temperatures, the beam becomes non-degenerate. As clearly can be seen, the influence of T_1 is much greater than of the small temperature region T_2. The traces were taken with decreasing T_2 at a constant T_1, which makes each vertical line a continuous measurement. So, the typical behavior while temperature is scanned from high to low (in this case T_2) is:

1. There is no conversion.
2. The conversion starts with low amplitude in the degenerate mode.
3. The converted power increases up to a power with the typical maximum conversion efficiency.
4. When the temperature further decreases, the mode becomes unstable and switches to non-degeneracy, while preserving similar power.

It is important to note that the down-scanning of the temperatures is crucial, as degeneracy can not be enforced while scanning upwards. Then, due to the hysteresis, only rarely the desired mode appears. This shows the meta stability of the degenerate mode, which is not necessarily the dominant mode, at least in the region of highest conversion power.

Instead of running temperature curves to find degeneracy, it turned out to be more efficient to knock at the optical table. When the temperatures are in the degenerate region of figure 3.11, the desired mode can easily be found, this way. This task can also be automated by using the autolocking function of NQontrol. The degeneracy can be monitored and if it is lost, the cavity could directly get a small pulse with the piezo to change the mode.

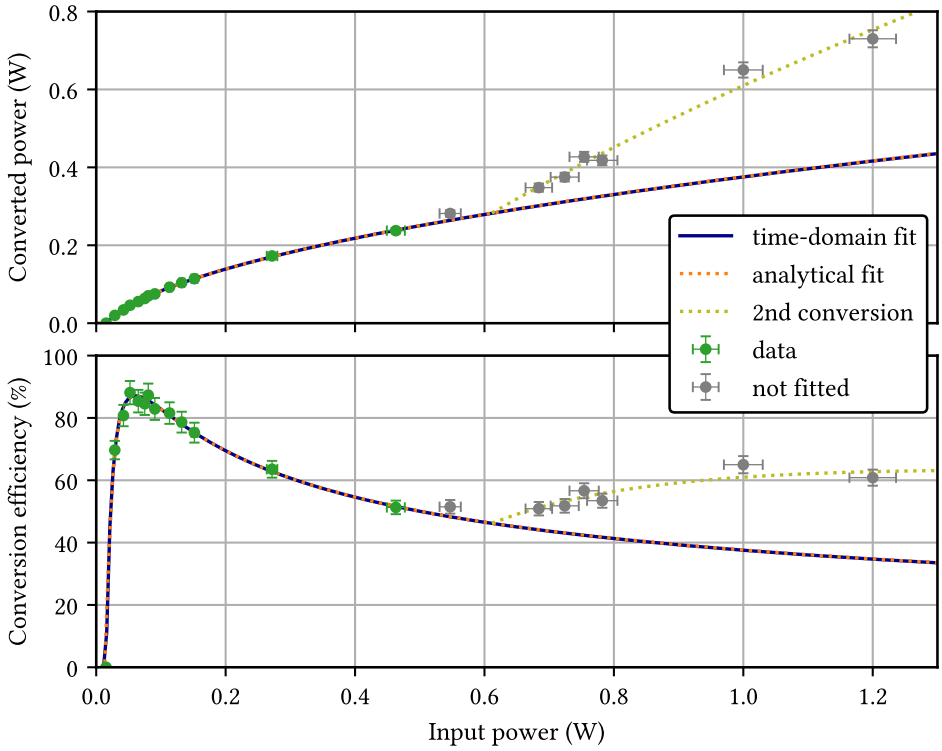

Figure 3.12: Power of the converted light (top) and external conversion efficiency (bottom). The indicated error bars correspond to the measurement accuracy of the thermal power meter of 3 %. The blue lines show our best fit to the data from a time-domain simulation model, while the orange dashed line shows a fit to an analytical formula for the converted power. At the point of maximum conversion efficiency, 52 mW of pump power was converted into 46 mW of output power. Above 0.5 W the converted power is higher than expected by the theory, therefore, those points were excluded from the fit (see text). They can be fitted assuming an additional conversion with a threshold power of 0.61 W and an efficiency of 34 %.

All in all, the instability decreased when we implemented polarizing beam splitters and were able to isolate the back-reflections of the confocal cavity. The degeneracy is expected to become even more stable in the future by using an enhanced optical isolator. The isolator we used so far, produced back-reflections which permanently triggered mode hops and, therefore, could not be placed directly in the optical path.

3.3 Conversion efficiency

The conversion efficiency η was measured versus the pump power by inserting a thermal power head into the pump and output fields, respectively. Figure 3.12 shows the measured power levels and the calculated external conversion efficiency, i.e. not corrected for power loss from mode-matching, reflection loss of the crystal's AR coating, internal absorption, as well as residual transmission through the resonator.

The measured data points can for low pump powers be fitted by using equation (3.1). Addi-

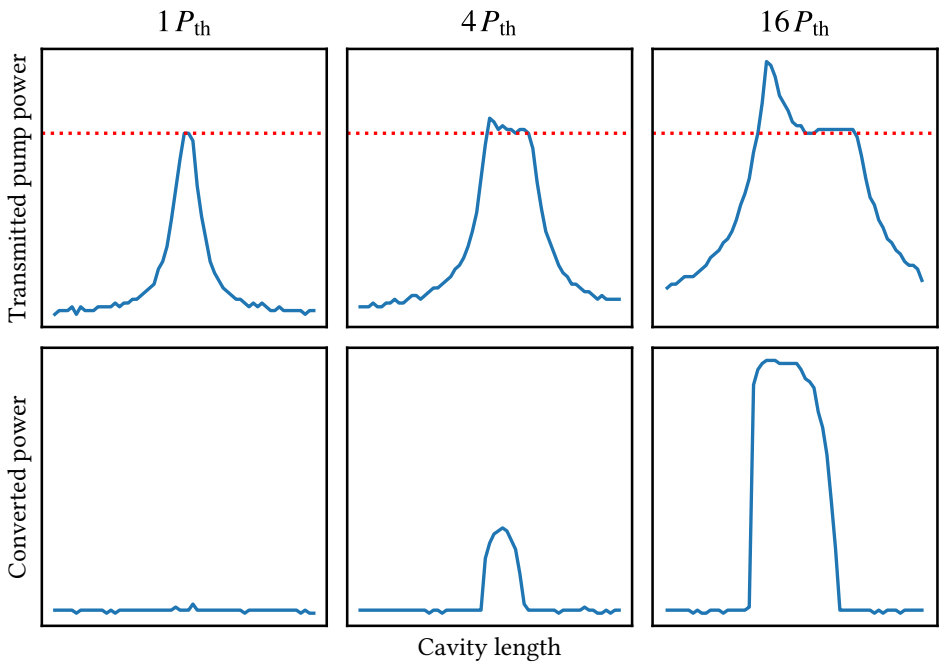

Figure 3.13: Cavity peaks at and above threshold power. Above threshold the pump depletion is clearly visible in a flattened maximum. The threshold power is marked in red. At 4 P_{th} the conversion reaches its maximum efficiency. The peak at 16 P_{th} shows an artifact, caused by local heating which degrades the phase matching while scanning over the peak.

tionally, we fitted a numerical model to the measured data using the time-domain simulation program NLCS [Las10]. As free parameters for the simulation, we used the effective nonlinearity d_{eff} and maximum external conversion efficiency η. We obtained $d_{eff} = 5.07$ pm/V, which includes internal loss of the DOPO resonator as well as additional phase shifts impeding perfect phase-matching. We infer a lower limit $d_{33} = \frac{\pi}{2} d_{eff} = 7.96$ pm/V on the nonlinear coefficient for the harmonic transition from 1064 nm to 2128 nm in quasi phase-matched PPKTP. This value is lower than the expected nonlinearity of $d_{33} = 10.05$ pm/V, which we assume to be caused by the cavity, as nonlinearities are usually measured in single pass.

The result for the maximum external conversion efficiency was $\eta = (87.1 \pm 0.4)$ % at an incident pump power of 52 mW. Correcting for the imperfect mode matching of the pump beam (94 %), we infer an internal conversion efficiency greater than 93 %.

Far above the pump power of optimal conversion, i.e. above 600 mW, the output power at 2128 nm was higher than predicted by the fit in figure 3.12. We assume that this was due to imperfect constructive interference of up-converted (re-converted) light with the pumped cavity mode, allowing for a second down-conversion process at higher threshold power. The data can be fitted assuming an additional conversion process with 0.6 W threshold power and 34 % efficiency. But operation at these powers should in any case be avoided to retain a stable and well controllable system.

Above threshold, the converted light impacts on the shape of the resonance peak of the pump light. At threshold power not only the conversion starts but also the pump is depleted, as shown in figure 3.13. Below threshold, the pump has the form of a typical cavity resonance

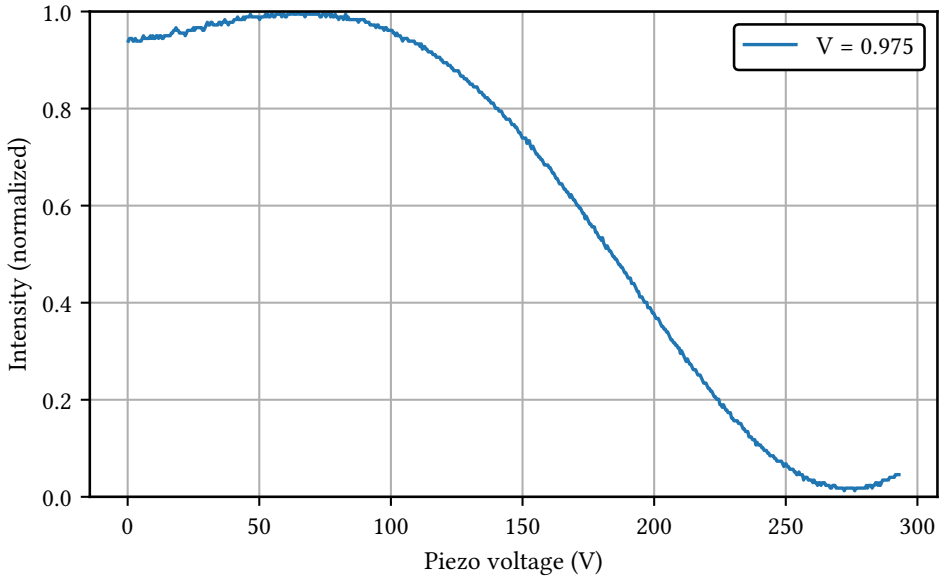

Figure 3.14: Demonstration of spatial mode quality and frequency stability. Shown is the interference fringe with visibility $V = 0.975$. The signal is generated by overlapping two independently converted 2128 nm beams on a 50/50 beam splitter. The phase difference was scanned by applying a high voltage ramp to a piezo-mounted mirror. The achievable phase difference was limited by the travel range of the piezo, compared to the long wavelength.

peak, but at input powers above threshold, the top of the peak starts to flatten. This plateau becomes more pronounced with increased pump power. Without conversion (i.e. at phase matching temperatures significantly above the point of degeneracy) the peaks would retain their Lorentzian shape also at high pump powers. At high power (16 P_{th}), a deformation of the peak above threshold power becomes visible. It can be explained by local thermal heating impeding the phase-matched conditions.

3.4 Interference of converted beams

The down-converted light should be usable in an interferometer and thus, retain the interferometric properties of the pump laser. As a first verification step, we duplicated the DOPO setup and measured the visibility between the two independently down-converted light fields at 2128 nm. If one of the DOPOs would introduce high phase or amplitude noise or the beam shape would be deformed, the visibility would decrease significantly. For this, the beams were overlapped on a 50/50 beam splitter. A piezo-mounted mirror allowed us to scan the relative phase between the two fields. The resulting interference fringes were monitored on a photodiode in one of the beam splitter output ports, see figure 3.14. We observed a stable and stationary interference pattern, indicating quasi-identical operation of the two DOPOs and high coherence between the two fields. A maximum interferometric visibility $V = 0.975$ was achieved, as defined in equation (2.24).

The visibility is a measure for the coherence properties of light. Deviations from $V = 1$ are furthermore caused by non-perfect beam overlap, differing beam powers, unequal splitting, as

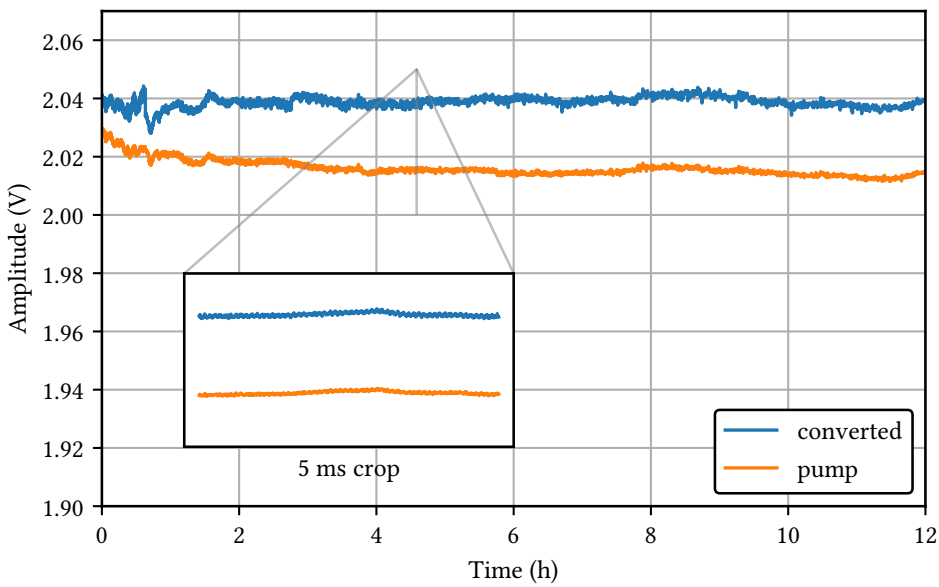

Figure 3.15: Long and short term stability of the pumped and converted light. The first two hours show larger disturbances, which reduce after the optical setup has thermalized and traffic around the lab area reduced during the night. Note the scale on the y-axis.

well as phase and amplitude fluctuations [SH10, p. 477-484]. Our measured visibility is the sum of all these imperfections, which results in a lower limit for the coherence properties of the converted fields. We assume that our visibility value was limited by imperfect beam overlap and even higher values would be achievable with careful alignment. We conclude that the two individual wavelength conversions preserve coherence properties to a high degree and therefore that the conversion approach is suitable for interferometric applications.

3.5 Power stability

Converting the wavelength should retain the stability properties of the pump beam, without introducing additional power drifts or amplitude noise. We measured the intensity of the pumped and converted light with separate photodiodes for twelve hours at a sampling rate of 200 kHz. Figure 3.15 shows the long and short term intensity stability, over the full time span and a zoom into a 5 ms segment. Both traces show small disturbances which are mostly correlated between the pump and the converted light. The relative error margins, starting from a settling time of 3 hours, are 0.11 % (pump) and 0.15 % (converted).

Figure 3.16 shows the corresponding spectra in the mHz and the kHz regime, calculated with LPSD [HRS02; TH06]. The conversion adds on average 4 dB to the noise level from 1 mHz to 500 mHz and 1 dB at frequencies 0.2 kHz to 100 kHz. The overall stability of the 2 µm light is thus similar to the stability of the NPRO pump laser.

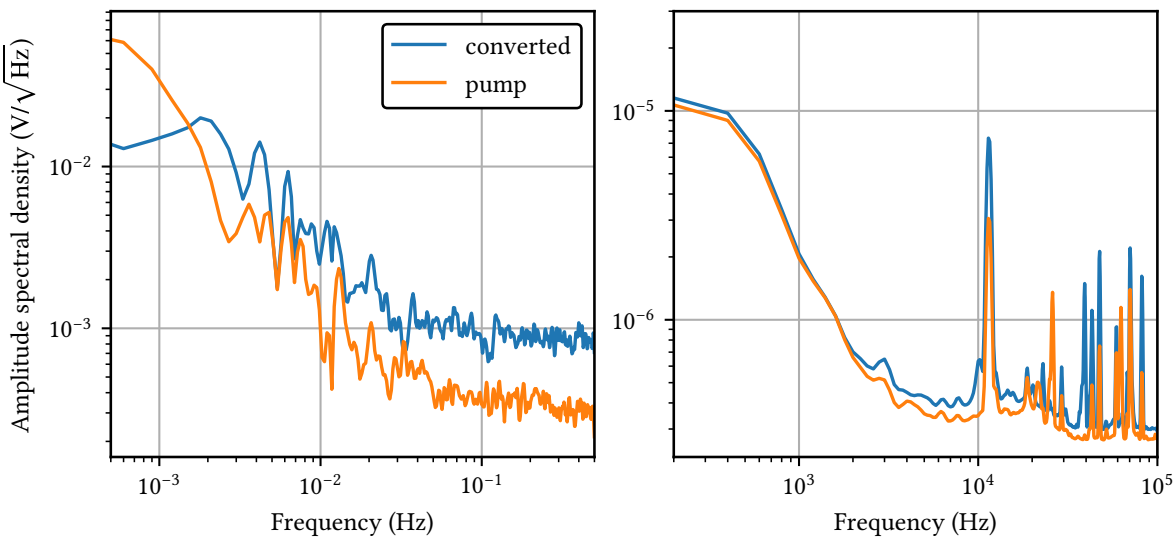

Figure 3.16: Spectra of pumped and converted light in the mHz and the kHz regime. The conversion nearly obtains the stability (on average 4 dB to the noise level from 1 mHz to 500 mHz and 1 dB at frequencies 0.2 kHz to 100 kHz).

3.6 Conclusion and outlook

With the current setup, the conversion works as expected, with an internal conversion efficiency of 92 %. The value of an effective nonlinearity allows for an adaption to different conversion powers and to shift the point of maximum conversion efficiency. As the laser source should be appropriate for interferometers, the coherence properties are important and are shown to be good.

In order to be used as light source for gravitational-wave detectors, the 2 µm light power has to be in the range of several tens or even several hundreds of watts. This can be solved either by laser amplifiers, typically fiber amplifiers, or by direct conversion of high-power pump light. For the conversion of high-power pump light, some adaptions have to be made to move threshold power and the point of maximum conversion efficiency to higher powers. One important measure will be to reduce the interaction with the nonlinear crystal by lowering the cavity's finesse or by increasing the beam diameter.

There are several boundary conditions which have to be considered for the adaption: The finesse of the pump light should be high enough (roughly 30) to provide a reasonable mode separation. To avoid exceeding the conversion threshold of unwanted modes, a finesse of at least around 10 for the 2 µm light seems necessary. In both cases, the lower finesse limits are educated guesses basing on simulations and system knowledge. If the beam size is increased, the cavity has to be redesigned, clipping avoided and mode separation optimized again. According to the manufacturer, the crystal height can not be increased to more than 1 mm, because the periodic poling requires high electrical field strength which is limiting in the manufacturing process. When avoiding beam shape changes the threshold power can be increased to about 5 W with lowered coupler reflectivities, which results in maximum conversion efficiency at 20 W. Adopting to much higher threshold power would require such a low

finesse, that the double-resonances could probably not be achieved anymore. Therefore, the next step would be to characterize the light source at about 20 W to 30 W.

4 | Generation of squeezed light at 2128 nm

The second central part of my project was to demonstrate a novel approach to generate and measure squeezed states of light at wavelengths around 2 µm and measure the light's uncertainty below vacuum noise. We published the central parts of this chapter in [Dar+21].

Usually, a second-harmonic generator (SHG) is used for frequency-doubling to provide pump light for the squeezer. As the vacuum noise is squeezed at the laser wavelength, the local oscillator is directly provided by the laser, only mode filtered with a mode cleaner cavity. This common approach requires a stable and now-noise coherent light source at the desired wavelength.

Due to the lack of lasers around 2 µm with comparable performance to the NPRO lasers at 1064 nm, our approach is to reuse the existing lasers and generate the local oscillator by degenerate parametric down-conversion. Hence, we directly use the laser light to pump the squeezer, resulting in a vacuum noise reduction at 2128 nm. Then, the local oscillator needs to be a bright, wavelength-doubled beam, whose generation was described the preceding chapter.

For this part of my thesis, I supervised Julian Gurs for doing his Master thesis [Gur21] that was to build the squeezed light source. To get some initial squeezing is comparatively straight forward, but the optimization process is slow and requires to investigate to every detail of the setup.

4.1 Experimental setup

The experimental setup (see figure 4.1) is slightly modified and extended compared to the setup described in section 3.1. Two nonlinear cavities are pumped with continuous-wave 1064 nm light from an NPRO laser. Here, one resonator was pumped above the lasing threshold (around 20 mW) for DOPO and produced about 46 mW at 2128 nm from about 52 mW at 1064 nm. The other resonator was pumped below the threshold power and therefore produced a well defined light beam with a TEM_{00} mode in a squeezed vacuum state at 2128 nm.

To detect the squeezed light in arbitrary squeezing quadratures, a balanced homodyne detector was installed (section 4.1.1), where the local oscillator and the squeezed vacuum are overlapped. For the squeezing detection and optimization, it is necessary to permanently monitor the wavelength degeneracy of the local oscillator. If the beam is non-degenerate, the

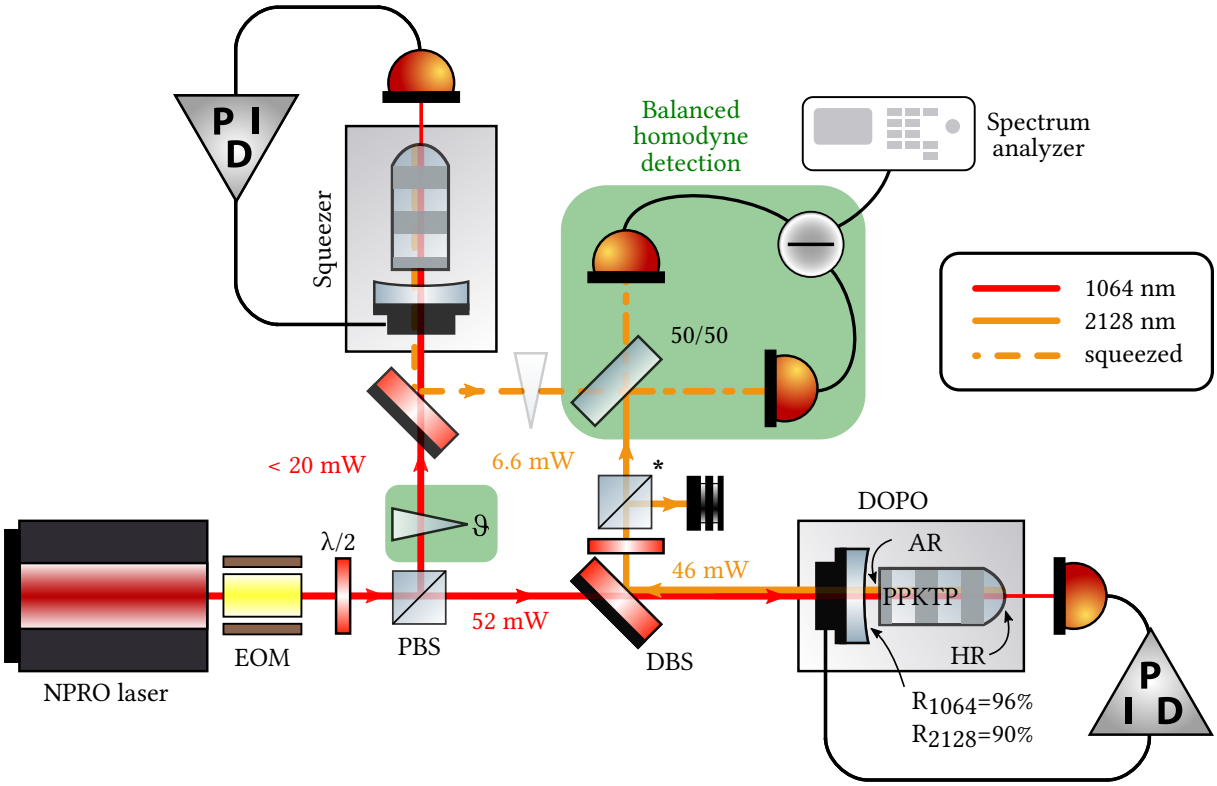

Figure 4.1: Schematics of the experiment. The NPRO laser provided up to 2 W output power at the wavelength $\lambda = 1064$ nm for the two identical nonlinear cavities: squeezer and DOPO. The squeezed light was detected with a balanced-homodyne detector. EOM, electro-optical modulator; PBS, polarizing beam-splitter; DBS, dichroic beam-splitter; * upward pointing PBS with a beam dump, providing *s*-polarized light. The transparently illustrated phase shifter was moved to be in front of the squeezer (see section 4.1.2).

squeezing level decreases or disappears completely. After finding out that the phase shifter piezo produces significant beam pointing, we moved it to the front of the squeezer preventing its influence on the beam overlap (section 4.1.2). Otherwise the pointing made it impossible to maximize the beam overlap while scanning the phase shifting piezo. Optimizing the beam overlap using the homodyne detector is possible, but limited at high visibilities. Therefore, we added a mode cleaner cavity for better optimization of the beam overlap (section 4.1.3).

4.1.1 Balanced homodyne detection at 2128 nm

The generated squeezing was analyzed with a balanced-homodyne detector (BHD). For this, it was overlapped with a bright beam from the DOPO on a 50 % beam splitter and both outputs were sent to photodiodes (extended InGaAs, Thorlabs FD05D), whose photo currents were then subtracted from each other. This method allows high amplification while avoiding additional electronic noise. The readout angle of the balanced-homodyne detector could be adjusted with a phase shifter, i.e. a piezo-mounted mirror, that was located in front of the squeezed-light cavity to suppress induced pointing loss. Our self-made electronics operated the photodiodes at a reverse bias voltage of 1 V and achieved a detection bandwidth of 30 MHz. The quantum efficiency of the extended-InGaAs photodiodes slightly increases with higher reverse voltage,

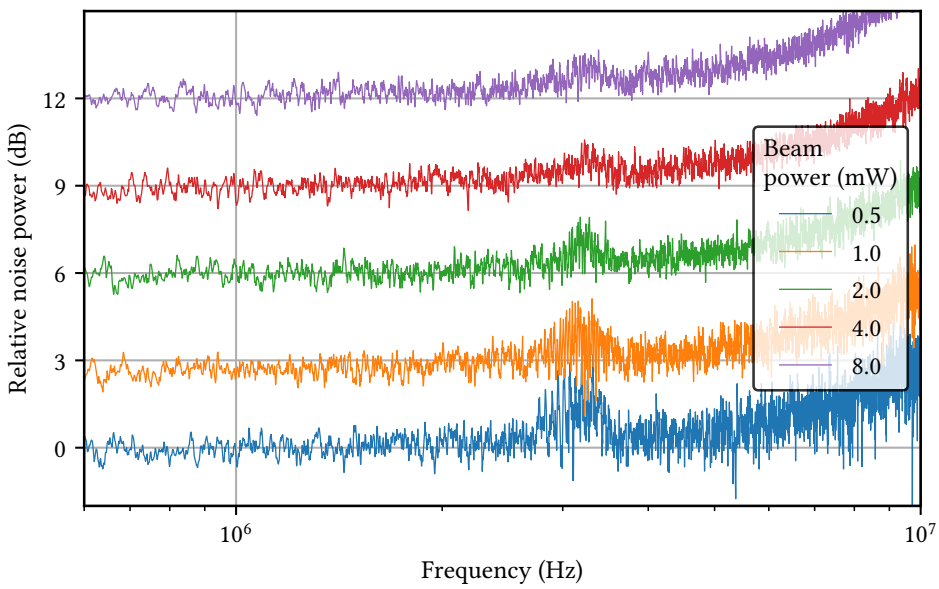

Figure 4.2: Homodyne detector linearity. The detector is linear up to at least 8 mW. Noise at 3 MHz and increasing amplitude around 10 MHz are artifacts from the dark noise.

but the dark-current and noise rise rapidly in this case. We have found a reverse voltage of 1 V to be a useful balance between quantum efficiency and noise. With the photodiodes' windows removed, we measured a quantum efficiency of (92 ± 3) % with a thermal power-meter (accuracy 3 %) and precise multimeters. Further details can be found in section 4.2. Linearity of the detector is reached up to a light power of 8 mW as can be seen in figure 4.2.

4.1.2 Phase shifter pointing mismatch

For a while, we were limited in the optimization of the beam overlap between local oscillator and squeezer. The visibility was on a plateau and worsened in each direction, but the value was only around 96 %. For optimization, we had to scan the phase between the beams with the phase shifter piezo, which produced significant pointing when it was scanned. With a sensitive adjustment of the mounting screws it was possible to slightly lower the pointing, but we were not able to remove it. Therefore, we placed the phase shifter in front of the squeezer, which completely removed the overlapping issues, as the output of the cavities stays stable. At this position the pointing does not have a significant influence on the squeezing level: Pointing reduces the mode matching of the squeezing cavity and thus, effectively slightly lowers the pump power. Moderate changes of the pump power, at an operating point in the range 0.5 to 0.8 $P/P_{\text{threshold}}$, only slightly affect the squeezing, as can be seen in figure 4.7. That position change allowed the optimization to the final squeezing levels.

4.1.3 Beam overlap

Imperfect beam overlap effectively produces optical losses in squeezing experiments. The first optimization to maximize the beam overlap can be done by maximizing the visibility on one of homodyne detector's photodiodes, which is described in section 3.4, where it was used to show the interference properties. The last percent of beam overlap can be reached by matching the spatial mode of both beams to the same reference cavity. For the reference cavity, we used existing mirrors with a relatively low reflectivity of 90 %, because the custom-built mirrors have a delivery time of months and it was not yet clear, if the beam overlap was the limiting factor. We had a finesse of 27, which allows the detection of additional modes around 1 %. Using a finesse in the order of 1000 enables the detection of much smaller unwanted modes and, hence, to increase the beam overlap. This is planned for the next iteration.

4.1.4 Monitoring and power adjustments

The final setup can be seen in figure 4.3, providing additional details: In front of the nonlinear cavities are upwards-directed polarizing beam splitters (PBS), allowing for independent power adjustments and ensuring a clean vertical polarization (*s*-pol). Semi-transparent mirrors behind the cavities allow to split the beam, e.g. to monitor the leaking light at 2128 nm and to simultaneously see the Gaussian mode in the coupling process. The first PBS after the DOPO is required for simultaneous monitoring of degeneracy and is used to provide light for other experiments. As the polarization is rotated to *p*-pol, a back-rotation with a waveplate is necessary, completed by another upwards-directed PBS to ensure a clean polarization. Using the PBSs has two more advantages: most of the converted power has to be dropped to avoid saturation of the photodiodes anyway, and additionally, back-reflections are reduced which makes the conversion more stable. All used PBSs at 2128 nm are custom-built and optimized for an angle of 9° to avoid direct back-reflections.

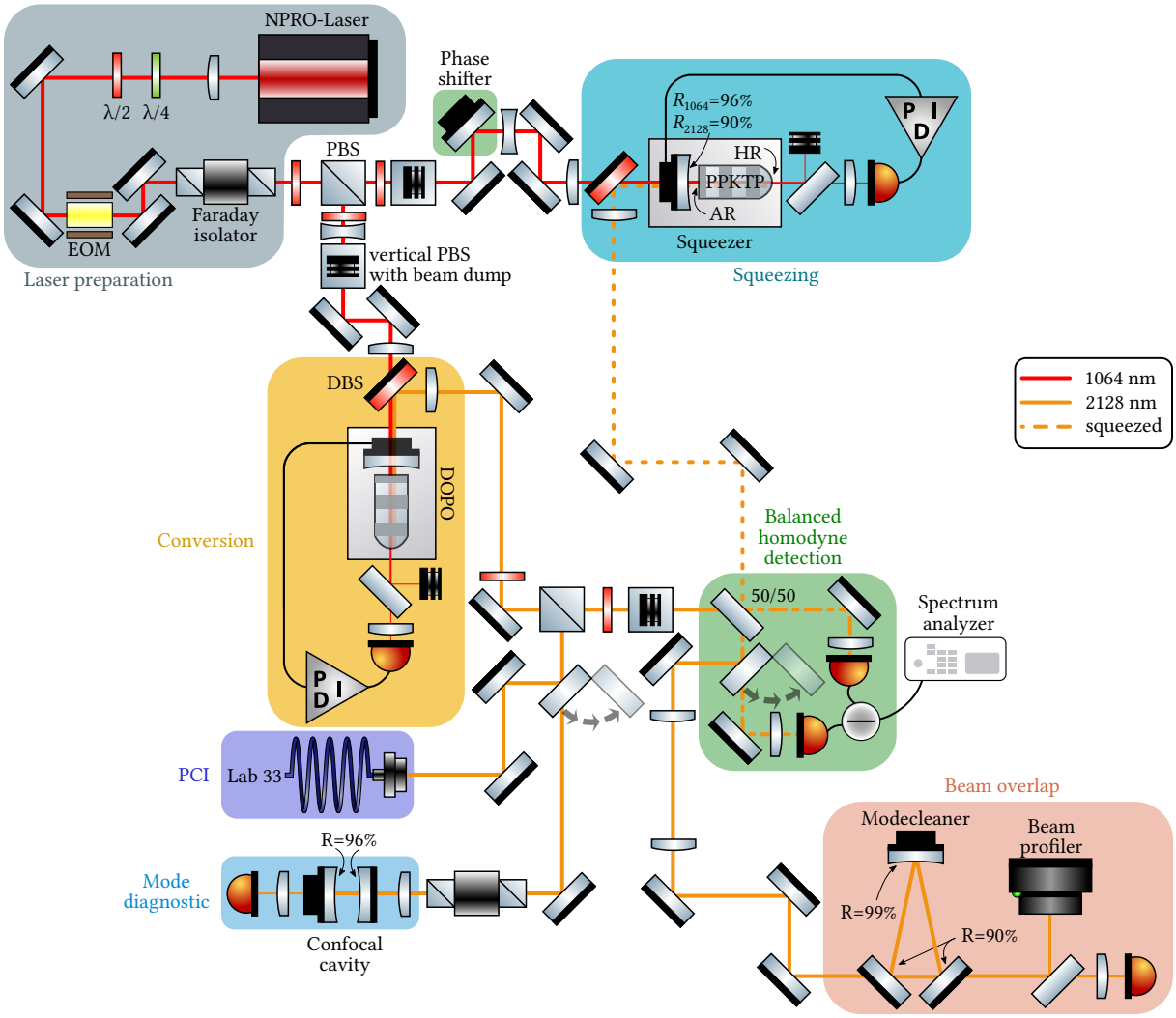

Figure 4.3: Complete scheme of the laser setup. On the top left is the pump light generation with our Mephisto laser. The polarization is cleaned with $\lambda/2$ and $\lambda/4$ plates and the beam height changed to 5 cm. For a Pound-Drever-Hall lock of the nonlinear cavities, the electro-optical modulator (EOM) imprints phase sidebands at 28 MHz and the Faraday isolator protects the laser from back-reflections. A polarizing beam splitter (PBS) is used to distribute the light to both cavities, where a vertically inserted PBS with beam dump on top provides a clean vertical polarization (s-pol) and makes the light power individually adjustable. The DOPO, used as local oscillator, and the squeezer are identical nonlinear cavities. The converted (squeezed) light is split from the pump light by a dichroic beam splitter. Two PBSs are used to reduce the power from 60 mW (where conversion is most stable) to below the saturation limit of the photodiodes. Furthermore, the reflected light of the first PBS is used for permanent degeneracy monitoring with a confocal cavity and the second PBS is used to clean the s-polarization again. The beams of both cavities are overlapped on a 50/50 beam splitter to be detected by a homodyne detector. With a flip mirror, the light of both cavities can be redirected to a mode cleaner for accurate beam overlapping. To prevent pointing of the piezo, the quadrature selecting phase shifter is placed in front of the squeezer.

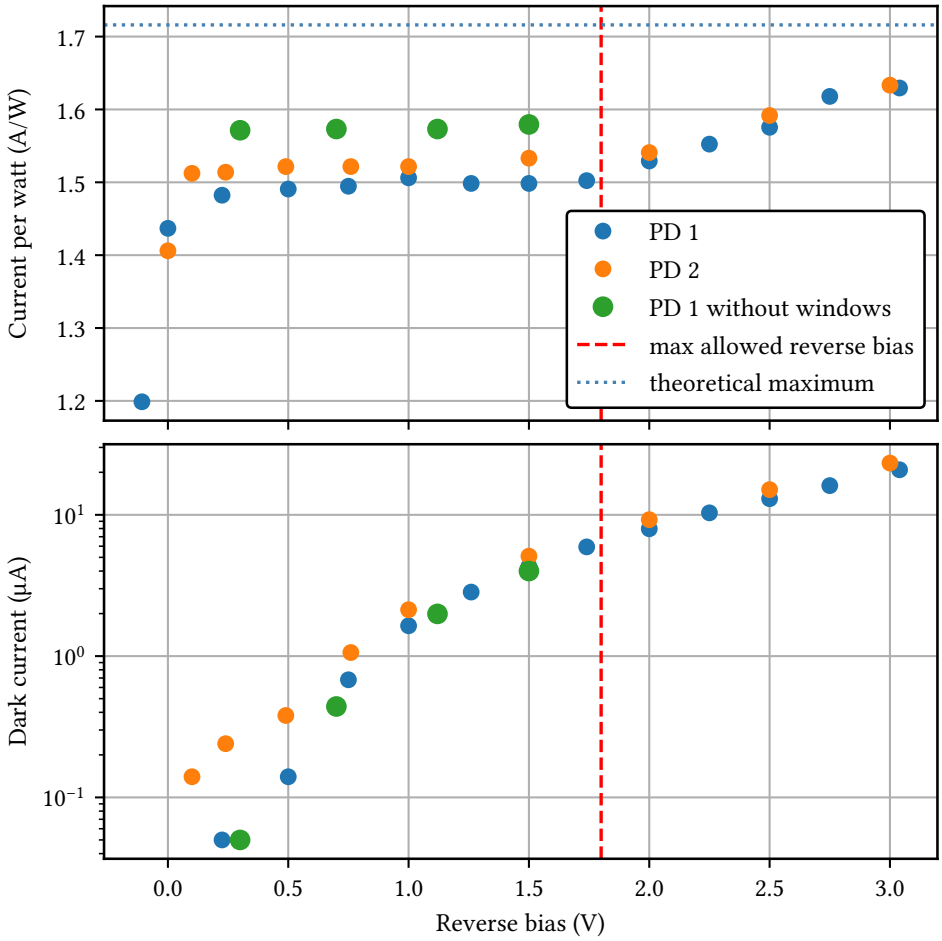

Figure 4.4: Photo-current divided by the power of the incident light, as the measurement without window was made with slightly increased power. Having low reverse bias, the photo current drops rapidly and with a bias voltage surpassing the allowed value of 1.8 V, the photo current increases further. Simultaneously, the dark current continuously rises with increasing reverse bias, making a compromise between photo current and dark current necessary.

4.2 Photodiode quantum efficiency

The quantum efficiency of the photodiodes contributes substantially to the optical losses. A precise quantum efficiency measurement is inherently difficult, because systematic inaccuracies do not cancel out and the accuracy of available powermeters is limited. Squeezed light can also be used to measure the quantum efficiency, but then all other loss sources have to be precisely known and thus, our squeezing measurement additionally gives a lower bound to the photodiode's quantum efficiency [Vah+16]. For other wavelengths, such as 1064 nm and 1550 nm, InGaAs PDs with more than 99 % efficiency are available [Vah+16], but around 2 µm photodiodes with high quantum efficiency do not exist yet.

To measure the quantum efficiency, the number of incoming photons is compared with the

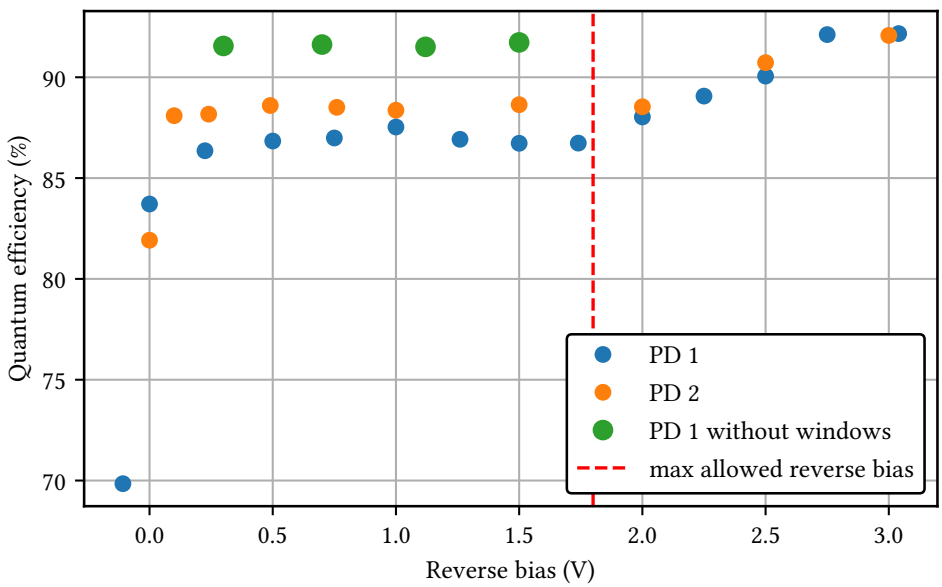

Figure 4.5: Quantum efficiency of the photodiodes used in the homodyne detector (Thorlabs FD05D). For the second measurement with removed window we only took data points at promising reverse bias levels to get a value for the actual quantum efficiency.

number of electrons of the photo current:

$$Q = \frac{n_\mathrm{e}}{n_\mathrm{ph}} = \frac{hc}{e\lambda}\frac{I}{P}$$

The dark current has to be subtracted, to ensure that only a light signal contributes to the current. If the dark current is taken into account, we get

$$Q = \frac{n_\mathrm{e}}{n_\mathrm{ph}} = \frac{hc}{e\lambda}\frac{I}{P} \cdot \frac{I_\mathrm{light} - I_\mathrm{dark}}{I_\mathrm{light} + I_\mathrm{dark}} .$$

We measured the power of the incoming beam with a thermal powermeter with an accuracy of 3 %, which is completely dominating the uncertainty, and the resulting photo current using a multimeter. Applying a reverse bias to the photodiodes leads to increased response, as well as higher dark current, as can be seen in figure 4.4. A moderate reverse bias is sufficient to get a maximum of quantum efficiency, while the dark current constantly rises with increased voltage. Using a voltage in the range of 0.5 V to 1 V turned out to be a good compromise. The photodiodes are covered by small windows for protection, their removal improved the gained quantum efficiency from about 88 % to 92 % (see figure 4.5), as the windows have a limited transmissivity.

While the two photodiodes (FD05D) in the homodyne detector were unexpected efficient, all measurements of different photodiodes revealed disappointingly low quantum efficiencies. Different models (Hamamatsu G12183-005K, Thorlabs FD10D, Laser Components, IG24x500S4i) were in the range of 70 % to 80 % and even other diodes of the FD05D type did not exceed 83 %. Hence, we had picked two photodiodes for the homodyne detector which yield a relatively high quantum efficiency.

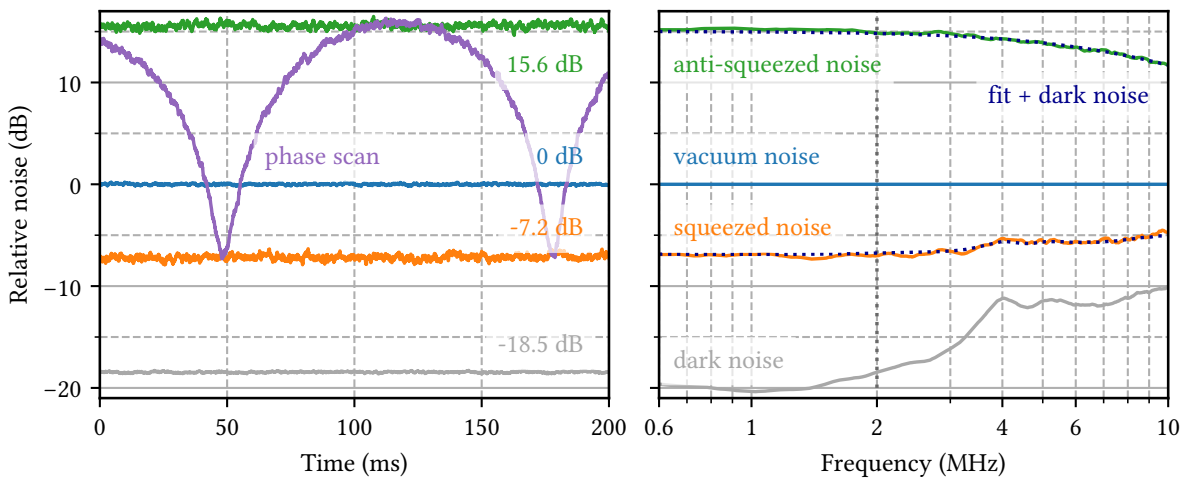

Figure 4.6: (Left) Zero-span noise measurement at a sideband frequency of 2 MHz. We achieved a squeezed noise reduction of (7.2 ± 0.2) dB below the vacuum noise, accompanied with an anti-squeezed noise in the orthogonal quadrature of (15.6 ± 0.2) dB. The noise arches were obtained by scanning the BHD readout angle. All traces were recorded with a resolution bandwidth (RBW) of 300 kHz and a video bandwidth (VBW) of 300 Hz. Dark noise and vacuum noise were additionally averaged 10 times using the same RBW and VBW.
(Right) Spectrum of the generated squeezed light in the regime 0.6 MHz to 10 MHz, fitted with the equations (4.1) and (4.2), where the dark noise was added to the fitting curves. All traces were averaged 10 times.

4.3 Squeezing at MHz sideband frequencies

Figure 4.6 presents noise variances from BHD measurements recorded with a spectrum analyzer, normalized to the vacuum noise. The left panel shows a zero-span measurement at 2 MHz, while the right panel shows the spectrum in the range 0.6 MHz to 10 MHz. Electronic dark-noise was not subtracted from these traces.

We obtained a non-classical noise suppression of (7.2 ± 0.2) dB at a sideband frequency of 2 MHz and a local-oscillator power of 6.6 mW. This squeezing level extended to lower frequencies, as shown in figure 4.6 (right), before the dark-noise clearance quickly decreases as the BHD's transfer function was optimized for the MHz regime. At our measurement frequency, electronic dark-noise was dominated by the dark-current of the photodiodes. It was not subtracted from the measurements and reduced the achieved noise suppression by about 0.3 dB. We estimate the error on the squeezed/anti-squeezed noise levels to ± 0.2 dB, as the BHD readout angle was not yet servo controlled and therefore prevented longer measurements at the optimal quadratures.

Random fluctuations of the phase between the squeezed-light beam and the local oscillator in the setup lead to a coupling between the squeezed and anti-squeezed light-field quadratures, which we denote here as $\hat{X}_1$ and $\hat{X}_2$, respectively. For a small amount of gaussian-distributed phase noise with an rms value of Θ, the measured quadrature variances $\Delta^2 \hat{X}^m_{1,2}$ are given by [Tak+07]

$$\Delta^2 \hat{X}^m_{1,2} = \Delta^2 \hat{X}_{1,2} \cos^2 \Theta + \Delta^2 \hat{X}_{2,1} \sin^2 \Theta \,. \tag{4.1}$$

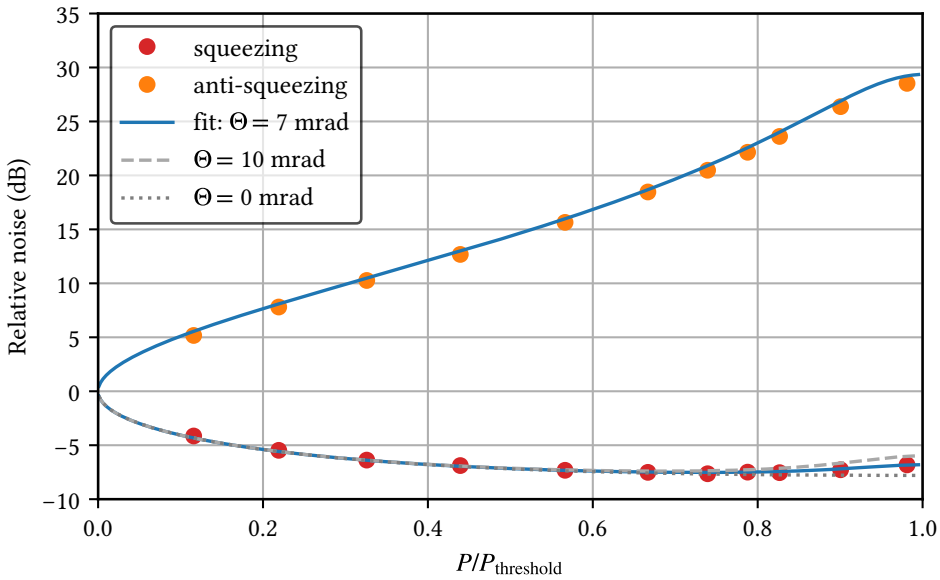

Figure 4.7: Dependence of squeezed and anti-squeezed noise levels on the pump power, as a fraction of threshold power. The data points were taken by using max hold for anti-squeezing and min hold for squeezing, comparing to the respective max/min hold vacuum noise reference. At high pump powers, the observed squeeze noise level degraded due to phase noise.

As phase noise becomes particularly relevant for large variances of the anti-squeezed quadrature, an upper bound can be determined by a measurement of the squeezing and anti-squeezing levels for various pump powers P up to the threshold power $P_{\text{thr}} = 20\,\text{mW}$. The quadrature variances themselves can be described by [Tak+07]

$$\Delta^2 \hat{X}_{1,2} = 1 \mp \eta \frac{4\sqrt{P/P_{\text{thr}}}}{\left(1 \pm \sqrt{P/P_{\text{thr}}}\right)^2 + 4(\Omega/\gamma)^2}\,, \tag{4.2}$$

where the upper sign corresponds to $\hat{X}_1$ and the lower sign to $\hat{X}_2$. Here, the variance of the vacuum ground state has been normalized to 1; η is the overall detection efficiency; $\gamma = 2\pi \cdot 64\,\text{MHz}$ is the linewidth of our squeezed-light cavity; and $\Omega = 2\pi \cdot 2\,\text{MHz}$ is the measurement sideband frequency. Combining equations (4.1) and (4.2), we fitted our measurements (figure 4.7) and obtained an rms phase noise of $\Theta = (7 \pm 1)\,\text{mrad}$. This phase noise is likely dominated by high-frequency fluctuations introduced by the locking loops of the cavities, as well as residual high-frequency fluctuations of the main laser beam. However, it is not limiting our squeezing results and we therefore did not yet implement steps to reduce it.

4.4 Optical loss analysis

State of the art squeezed light sources are entirely limited by optical loss, which arises from absorption, scattering, imperfect mode matching and imperfect quantum efficiency of the photodiodes. The total optical efficiency η can be derived from a combination of the squeezed and

anti-squeezed variances $\Delta^2\hat{X}_1$ and $\Delta^2\hat{X}_2$ (with dark noise subtracted),

$$1-\eta = \frac{1-\Delta^2\hat{X}_1\Delta^2\hat{X}_2}{2-\Delta^2\hat{X}_1-\Delta^2\hat{X}_2}\,.$$

Inserting the measured values of −7.2 dB squeezing and 15.6 dB anti-squeezing, we arrive at an efficiency of $\eta = (83.9 \pm 0.5)\,\%$.

We have estimated the loss contributions in our setup from the measured quantum efficiency of the photodiodes (details in section 4.2) and manufacturers' specifications of the optics. These are summarized in table 4.1.

Table 4.1: Overview of optical efficiencies

Source	Efficiency (%)
Resonator escape efficiency	98 ± 1
Propagation efficiency	> 99
BHD visibility $(98 \pm 1)\,\%$	96 ± 2
Photodiode quantum efficiency	92 ± 3
Total value as product of estimated efficiencies	85 ± 4
Total value from squeeze and anti-squeeze values	83.9 ± 0.5

The escape efficiency of the squeeze resonator is given by $T/(T+L)$, where T is the coupling-mirror transmissivity, and L is a sum of all round-trip losses, such as from an imperfect anti-reflective coating on the crystal, scattering and absorption loss, as well as residual transmission through the non-perfect reflecting back face of the crystal. It was calculated using the values of the manufacturers of crystal, coating and coupling mirror.

Propagation loss towards the homodyne detector is likely small, due to the use of high-quality optics and infrared-grade fused silica substrates, and has been estimated to <0.1 % per surface. The beam overlap (*visibility*, see equation (2.24)) between the local oscillator and squeezed beam at the balanced-homodyne detector contributes quadratically, and therefore has a high impact. We measured a visibility of $V = (98 \pm 1)\,\%$. As stated in section 4.1.3, this could be improved by coupling both beams to a high-finesse mode-cleaner cavity, which is planned for the next iteration. Finally, we include the non-perfect quantum efficiency of our photodiodes, around 92 % according to our measurements, which should be around 75 % with windows and without reverse bias, according to the manufacturer and a measurement in [Man+18]. The quantum efficiency of the photodiodes is still the largest individual loss source and the limiting factor to measure higher squeezing levels.

Within its relatively large error bars, our estimated value for the overall efficiency is in good agreement with the one obtained from the squeezing and anti-squeezing measurement.

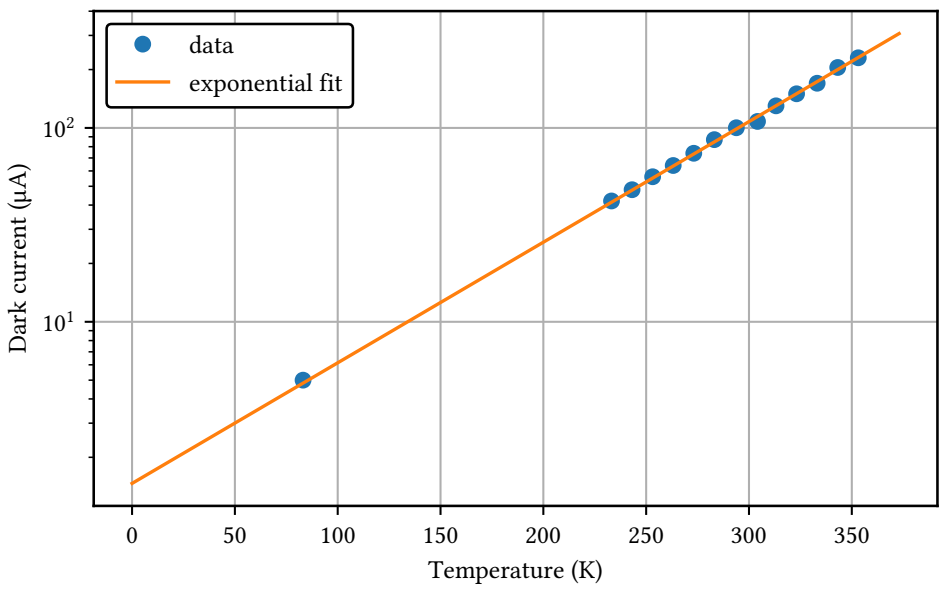

Figure 4.8: Dark current temperature dependency of a Thorlabs FD05D photodiode. The photodiode was cooled with liquid nitrogen and the temperature monitored using an infrared camera. The gap in the data points origins in the limited temperature range of the camera and the lowest point was cooled as much as possible. We get an exponential dark current decrease from 97.5 µA at 20 °C to 4.4 µA at the temperature of liquid nitrogen 77 K.

4.5 Cooling of photodiodes

Photodiodes can be cooled for dark noise reduction, however, this is usually only specified down to −40 °C, at least for all our tested photodiodes. The increased quantum efficiency at high reverse voltage above specification provoked our hope to improve the photodiode's efficiency while lowering the dark noise through cryogenic cooling. A first simple investigation measurement is shown in figure 4.8, where we cooled the photodiode (Thorlabs FD05D, a specimen which had more dark current than the photodiodes we used in the homodyne detector) with liquid nitrogen while monitoring the temperature using an infrared camera. Extrapolating down to 10 K, cooling the photodiodes could possibly reduce the dark current by a factor of 50 and allow to get some percent more quantum efficiency with increased reverse voltage. Further investigations with a cryostat, however, showed that this is not the case: Even though the photo current is not much affected by cooling to 10 K, at high frequencies such as our squeezing sideband frequency at 2 MHz we could not measure any temperature influence on the noise level. The noise level still rapidly increases with reverse bias, therefore the usage of high reverse bias at low temperatures is not an option. First measurements of a noise spectrum of a cooled photodiode showed however that cryogenic cooling is an interesting option for squeezing at acoustic frequencies. Julian Gurs further investigated the cooling potential and could confirm our expectation that cooling reduces the $1/f$ noise and, hence, gets more important towards lower frequencies and will be important to measure high squeezing levels in the audio band. A more detailed analysis by Julian Gurs is forthcoming.

4.6 Conclusion

With 7.2 dB, we have measured the highest squeezing levels around 2µm, so far, using the new approach of combining squeezing with wavelength-doubling to squeeze at twice the laser wavelength. This allows to reuse the existing, highly optimized NPRO laser type that are currently running in gravitational-wave detectors.

The squeezing value of (7.2 ± 0.2) dB is mainly limited by the quantum efficiency of the available photodiodes. The second important loss contribution is the beam overlap between local oscillator and squeezed vacuum, which can be improved in the next step using a high-finesse mode cleaner cavity. Our phase noise is insignificant for the achievable squeezing levels, even though we did not implement any noise reduction methods.

We expected the squeezing levels to be limited by the quantum efficiency of the photodiodes. Nevertheless, we could measure a quantum efficiency of the two photodiodes in the homodyne detector to be (92 ± 3) % with reverse bias and removed windows, as described in section 4.2. This high efficiency might seem inconsistent, but the overall losses can be calculated from the squeezing measurement of (7.2 ± 0.2) dB and are (16.1 ± 0.5) %. That means, the squeezing measurement already confirms the quantum efficiency to be greater than 84 %.

In principle, detection losses can be avoided by using an optical-parametric amplifier (OPA), which is a similar nonlinear crystal as used for conversion and squeezing. It amplifies the overall signal and the reduced quantum noise, making losses behind the device less important. But to be a worthwhile option, the losses corresponding to the additional nonlinear cavity need to be significantly less than the 8 % we get from direct photodiode usage.

The next steps towards application in a gravitational-wave detector prototype would be to measure squeezing at acoustic frequencies and, by the way, improve the squeezing level. For the transition to acoustic frequencies, back-scattering has to be shielded as the noise level is very sensitive to stray light at low frequencies. Furthermore, the $1/f$ noise of the photodiodes will become significant and can be reduced by cryogenic cooling, which should be implemented to maximize the squeezing.

5 | Digital control systems

Control systems are an essential part of optical experiments. A common use case on an optical table is to hold cavities on resonance or to stabilize lasers to a frequency reference. Early in the project, the idea was to digitize all the required control loops and to build a replacement for the analog servo controllers which were formerly used in the group. Therefore, besides working in the lab, I programmed the digital control system NQontrol (see section 5.2), which was directly implemented and tested in the lab. This way, early feedback was possible to find bugs and optimize usability in the lab. With the realization of a funded digital temperature control project (section 5.3) and with supervision of a Bachelor thesis in the topic of filter design automation (see section 5.2.4), digital control systems became a significant part of my project. The temperature control system is used to stabilize the temperatures of the nonlinear crystals.

This chapter contains three main parts. First, I introduce control systems in general while focusing on the theoretical aspects to understand the background of NQontrol, combined with an introduction on how to work with control systems. A project description of NQontrol follows, where its control performance is evaluated and possibilities of automatic filter optimization are investigated. The chapter closes with a project description of the digital temperature controller Raspitemp.

5.1 Introduction to control systems

This section is a brief introduction to feedback control systems as used in NQontrol. I mainly follow Bechhoefer's tutorial for feedback systems [Bec05]. In general, control systems compare a measured value with a set point and give a feedback on the system to minimize the error signal.

Control systems are usually described by a theory which assumes linear and time invariant (LTI) systems. Linear means that the system answer X_i of the superposition of signals s_i should equal the sum of the individual answers

$$\sum_i X_i\left[s_i(t)\right] = X_i\left[\sum_i s_i(t)\right].$$

Those assumptions mean that the systems should not have nonlinear effects, a hysteresis or other path dependencies. That is usually a good approximation, especially in states with low disturbances when the system is well controlled.

5.1.1 System dynamics

In general, system dynamics can be formulated as a vector function f which describes the change of system states in dependence of n independent internal states $\vec{x}$ and m independent inputs $\vec{u}$:

$$\dot{\vec{x}} = \vec{f}(\vec{x}, \vec{u}) \tag{5.1}$$

The internal states are usually not completely accessible, wherefore system control depends on p measurable outputs $\vec{y}$ which are described by

$$\vec{y} = \vec{g}(\vec{x}, \vec{u}). \tag{5.2}$$

A full description of system dynamics can be extremely complicated, but for linear systems it simplifies to the matrix description

$$\begin{aligned} \dot{\vec{x}} &= \boldsymbol{A}\vec{x} + \boldsymbol{B}\vec{u}, \\ \dot{\vec{y}} &= \boldsymbol{C}\vec{x} + \boldsymbol{D}\vec{u}, \end{aligned} \tag{5.3}$$

where $\boldsymbol{A}$ is a $n \times n$ matrix describing the system dynamics and $\boldsymbol{B}$ is a $n \times m$ matrix describing the input coupling. The $p \times n$ matrix $\boldsymbol{C}$ defines the output coupling to the externally visible variable $\vec{y}$ and the $p \times m$ matrix $\boldsymbol{D}$ is a direct feed of disturbances from the other inputs.

For real systems, $\boldsymbol{A}, \boldsymbol{B}, \boldsymbol{C}, \boldsymbol{D}$ are unknown and have to be estimated by using impulse answers or transfer functions to determine the external system dynamics. In time domain a complete system description can theoretically be done with a Dirac pulse (δ function); then, the response of the system is monitored over time. In reality a perfect Dirac pulse is obviously impossible to create, requiring an approximation with a sharp high-amplitude pulse. Such a pulse can lead to nonlinear effects or damage the system (which also is a nonlinear effect) and therefore, a step function is usually used, which provides an equivalent description. A step answer of a mode cleaner, used to test the NQontrol system, can be found in figure 5.10.

5.1.2 Frequency domain

The system can also be described in frequency domain, providing a more intuitive way for the design of feedback filters and to understand the system. Here, we use the Laplace transform, which is similar to the Fourier transform, but commonly used in control-theory with some minor advantages

$$\mathscr{L}[y(t)] \equiv y(s) = \int_0^\infty y(t)e^{-st}\mathrm{d}t. \tag{5.4}$$

Differential equations of n-th order transform to n-th order algebraic equations. For example, the first order lowpass

$$\dot{y}(t) = -\omega_0 y(t) + \omega_0 u(t)$$

becomes

$$sy(s) = \omega_0[-y(s) + u(s)],$$

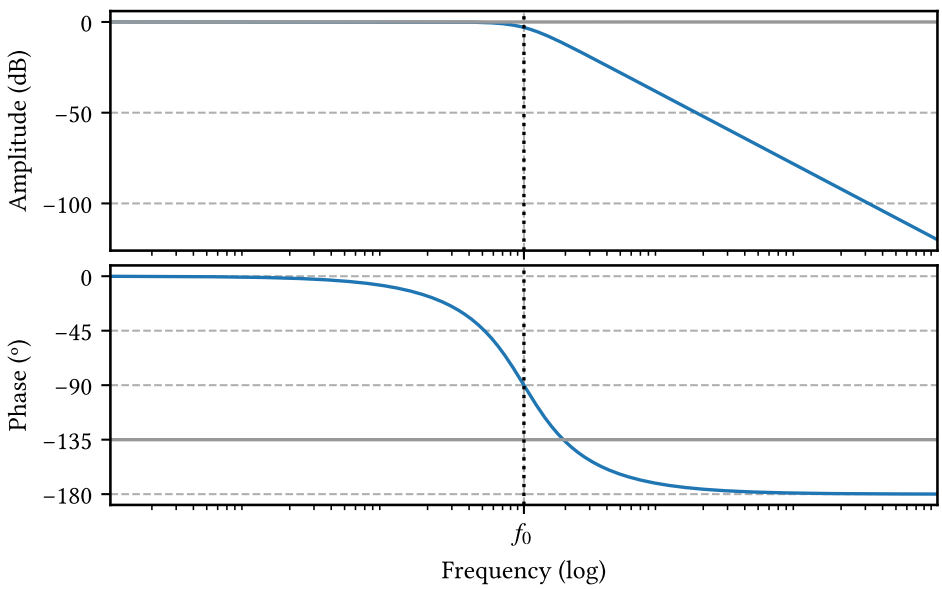

Figure 5.1: Bode plot of the example lowpass filter. The frequency f_0 with -3 dB damping is called corner frequency.

which leads to the transfer function

$$G(s) \equiv \frac{y(s)}{u(s)} = \frac{1}{1 + s/\omega_0},$$

with $\omega_0 = 2\pi f_0$, where f_0 is the characteristic frequency of the lowpass. The transfer function, also known as frequency response analysis, is the relation between output and input signal of the system versus the signal's frequency. This can easily be measured with a network analyzer, which sweeps the frequency of an input sine wave and compares amplitude and phase with the output signal. Bode plots are usually used to visualize the resulting data, as they combine a double-logarithmic amplitude plot with the corresponding phase. The theoretical transfer function can be evaluated at different frequencies by using $s = i\omega$ and taking the absolute value for the amplitude

$$|G(i\omega)| = \frac{1}{\sqrt{1 + \omega^2/\omega_0^2}}$$

and

$$\arg G(i\omega) = -\frac{1}{\tan \omega/\omega_0}$$

for the phase, which can be seen in figure 5.1 for the lowpass example.

5.1.3 Feedback

Now having a system description and characterization techniques, we can introduce a feedback controller to stabilize the system. The feedback requires an error signal $e(t) = r(t) - y(t)$, which is the difference between control signal (set point) r and system output y, to feed a manipulation signal back to the controlled system and minimize the error (figure 5.2). Hence, the

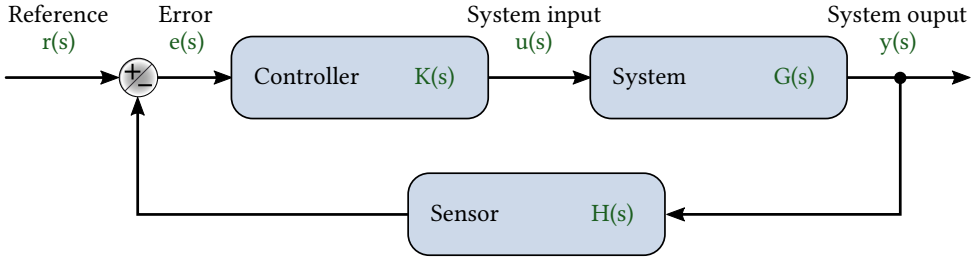

Figure 5.2: Feedback control scheme with included sensor noise $H(s)$.

output should follow the control signal as precisely as possible. Adding the controller $K(s)$, by multiplying in frequency domain, extends the description of the system to

$$y(s) = K(s)\,G(s)\,e(s)$$

and closing the loop results in

$$y(s) = \frac{K(s)\,G(s)}{1 + K(s)\,G(s)} r(s) = \underbrace{\frac{L(s)}{1 + L(s)}}_{T(s)} r(s),$$

with the loop gain $L(s) \equiv K(s)\,G(s)$. For $|L| \to \infty$, $y(s)$ tracks $r(s)$ as desired. Now the new system $T(s)$ should be "better" than the uncontrolled system $G(s)$, which usually means suppression of noise or even stability at all. In case of optical cavities, an uncontrolled system is completely unstable, which makes a feedback controller mandatory to establish resonance between the cavity and the corresponding laser.

To measure the system outputs y, one has to use sensors that introduce additional noise, such as electronic noise, shot noise and thermal noise. There is a fundamental trade-off between the suppression of disturbances and the amplification of measurement noise. Including the additional noise term $\xi(s)$ to the error signal

$$e = r - \xi - y$$

and disturbances $d(s)$ to the output leads to

$$y(s) = \frac{KG}{1 + KG}[r(s) - \xi(s)] + \frac{1}{1 + KG}\,d(s). \tag{5.5}$$

Especially when equation (5.5) is rewritten to

$$e_0(s) \equiv r(s) - y(s) = [1 - T(s)] \cdot [r(s) - d(s)] + T(s)\,\xi(s),$$

where e_0 is the tracking error which is the difference between desired output and actual output, the trade-off becomes clearly visible. For large T, the disturbances d are highly suppressed but the measurement noise ξ is amplified, and vice versa. At unity gain $|KG| = 1$ a phase lag of $-180°$ leads to amplification of disturbances and hence an unstable system. The phase margin is defined as difference between phase lag and $-180°$ at unity gain. To have a stable system the phase margin should be at least 45°, corresponding to a phase lag of $-135°$. The task of control optimization now is to find the optimal frequency-dependent gain that leads to a large suppression of disturbances but at the same time does not introduce too much sensing noise. One usually wants high gain for high noise suppression at lower frequencies with enough phase margin. As soon as the phase lag gets too high the gain should be as low as possible.

5.1.4 Zeros and poles

Arbitrary transfer functions can be described as a quotient of two polynomials. Limiting the order of polynomials to a system dependent value makes sense to avoid overfitting and approximates the real system. In general, a polynomial transfer function looks like

$$G(s) = \frac{y(s)}{u(s)} = \frac{b_m s^m + b_{m-1} s^{m-1} + \cdots + b_1 s + b_0}{s^n + a_{n-1} s^{n-1} + \cdots + a_1 s + a_0} .$$

It can be rewritten to the form where poles $p_1, \ldots, p_n$ and zeros $z_1, \ldots, z_m$ are directly visible:

$$G(s) = b_m \frac{(s + z_1)(s + z_2) \cdots (s + z_m)}{(s + p_1)(s + p_2) \cdots (s + p_n)}$$

Control systems as well as filters can be described with these *zpk* (zeros, poles, gain) transfer functions.

5.1.5 Control filters

To get an idea of possibilities in filter design, I present a small overview of the filter types implemented in NQontrol, which are the typical set of tools to create advanced controllers. They can be extended by arbitrary zeros and poles (see section 5.1.4), which allows for even more complex filters. As the filters in NQontrol have second order, two tuning parameters are available for each filter, which are e.g. the frequencies where the slope starts and stops in case of integrator and differentiator. Then, there is an overall gain acting on the complete transfer function of all combined filters. Note, that the here presented second order filters differ from the common filters of PID controllers. For PID controllers each filter is adjusted by one gain and not by two parameters, as two different frequencies. Without specific filters, when closing the loop with a defined gain the controller effectively acts only has a proportional (P) gain.

With only the proportional gain it might not result in a properly controlled system, as it does not guarantee to reach the set point. Imagine a radiator in a cold environment. As the system gets closer to the set point, the feedback value approaches 0, so the set point will not be reached, resulting in an equilibrium temperature below the set point.

Integral filter An integral (I) filter integrates over the past time to correct for remaining errors over time. Without integration and the resulting high gain at low frequencies, the controlled system would never reach the desired set point if any residual forces act on it. The feedback is given by

$$H_{\mathrm{I}}(s) = \frac{s - \omega_0}{s - \omega_{\mathrm{s}}},$$

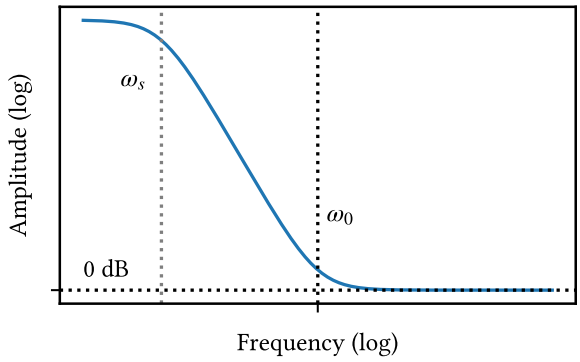

with the corner frequency ω_0 and ω_{s} where the gain stops being increased towards lower frequencies. In the example of the radiator, a remaining error will sum up in the integral and lead to a control signal which will continuously heat and reach the set point.

Differential filter The differential (D) filter acts on the derivative of the error signal and therefore reacts fast on changes. Its transfer function is defined by

$$H_{\mathrm{D}}(s) = \frac{\omega_{\mathrm{s}}}{\omega_0} \cdot \frac{s - \omega_0}{s - \omega_{\mathrm{s}}},$$

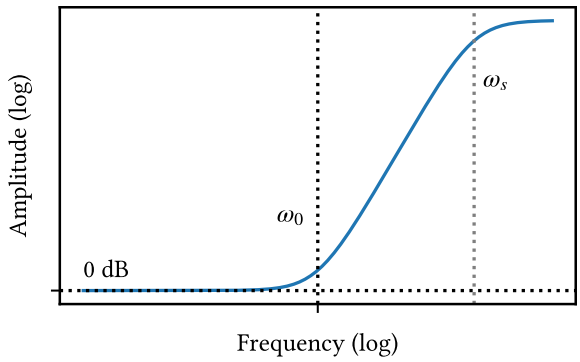

where ω_{s} is the frequency where the gain stops increasing towards higher frequencies. The faster the error signal changes, the greater the feedback signal will be. In the heating example, the D controller will counteract a sudden temperature change of the environment. Hence, in general the D gain responds quickly to high-frequency disturbances.

Notch filter A notch filter can be used to suppress strong resonances. It allows to increase the overall gain while suppressing a specific frequency region which otherwise would produce oscillations. In an asymmetric variant it can also act as a very sharp cutoff filter. The filter is conveniently represented in frequency domain as described by

$$H_{\mathrm{N}}(s) = \frac{s^2 + \omega_0^2}{s^2 + \omega_c s + \omega_0^2},$$

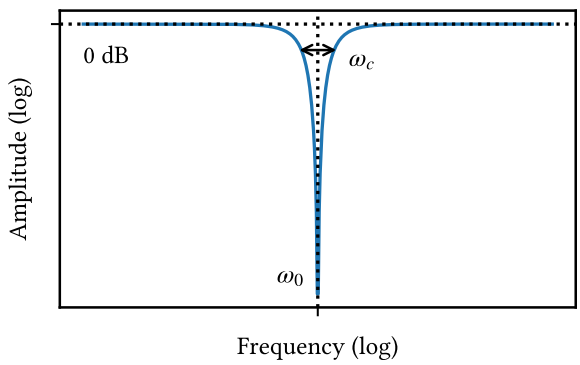

with the central frequency ω_0 and the width ω_c of the suppressed frequency band.

5.1.6 Feedback optimization and stability

After having a controlled system, the question arises how a system can be optimally controlled. Having multiple filters leads to a system with many depending variables, which makes the optimization process inherently difficult. One usually wants the maximum possible bandwidth, high noise suppression and very low gain above the bandwidth limit to avoid coupled noise at high frequencies. But filter design for minimized noise is not necessarily identical to design with the fastest response to set-point changes or huge disturbances. In reality it is even worse: optimal (here: fastest response or highest noise suppression) control is typically rather unstable if the system parameters change slightly. For example, if the light power in a cavity increases, the effective system gain increases and thus, can lead to oscillations even if the filter was optimized beforehand for the lower input power. To sum up, in most cases one does not want *optimal* control, but *good* and *robust* control.

Multiple manual and mathematical heuristics have been developed to obtain useful parameters for the classical PID controllers. One of them is the Ziegler-Nichols method [ZN42], which is used by the temperature controllers of Raspitemp (section 5.3). Here, the critical P-gain, where the system oscillates continuously, is used together with the oscillation period to calculate the P-, I- and D-gains. If more complex filters are available, the system behavior can be further optimized, but the simple heuristics cannot be used anymore.

In our digital control system (section 5.2), we have five second order filters available and, hence, a completely different approach is required for fine tuning. We use the common technique of *loop shaping* of a transfer function in frequency domain. Therefore, an open-loop transfer function of the controlled system itself is taken and the transfer functions of the filters are added by calculations to shape the complete closed-loop system with added feedback. For a first appropriate shape, the resulting transfer function should have a typical "look": High gain at low frequencies, unity-gain (0 dB) crossing at the highest possible frequency with a phase lag below 135° and low gain above this point. Now, the optimal shape of the transfer function depends on many system parameters and can be further fine-tuned while observing the real controlled system. One of the trade-offs which cannot be optimized only by the shape of the transfer function is the gain at frequencies well below unity-gain. High gain leads to high suppression of noise and disturbances, but at the same time imprints the sensor noise on the system. Depending on the sensor noise level, for each frequency exists an optimal gain which balances out noise suppression and sensor noise. Having explained some of the approaches and challenges for control systems, we will come back to the optimization topic when presenting the automation of the design process in section 5.2.4.

5.1.7 Practical example: optical cavity

In the case of an optical cavity, the error signal near resonance is fairly linear and the assumption of an LTI system is sufficiently good for a controlled state. The length of the cavity has to be held at a constant multiple of $\lambda/2$ against temperature drifts, acoustic noise and laser drifts on a level of much less than $\Delta\nu_{\text{linewidth}}/\Delta\nu_{\text{FSR}} \cdot \lambda \approx 7\,\text{nm}$ for our nonlinear cavities. In this corner case, the fluctuations of the output light power would be around 50 %. Since the cavity is not stable enough to stay in the linear regime of the error signal for long enough to obtain a

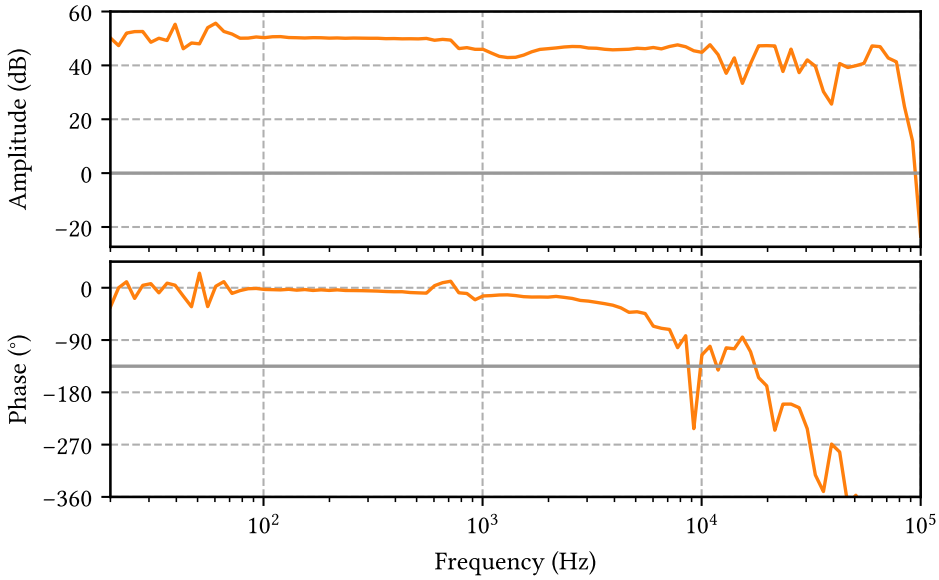

Figure 5.3: Transfer function of the nonlinear cavity that produces the local oscillator field. Towards 10 kHz the phase delay, caused by the piezo, becomes relevant and limits the achievable control bandwidth.

transfer function, first of all it hast to be controlled with a non-optimized filter. An integrator around 500 Hz has shown to be an appropriate first guess. Figure 5.3 shows the corresponding open-loop transfer function, where a network analyzer was used to sweep a sine wave from 20 Hz to 100 kHz to add a disturbance to the system. The measured transfer function is the relation between system output (error signal) and system input (sine added to the control signal in front of a HV amplifier). From the Bode plot it can be seen that piezo resonances start at around 10 kHz and at higher frequencies the phase lag becomes more than 180°.

Adding just a simple negative feedback (*P* gain) would not create a controllable system, as the system gain is high up to more than 30 kHz where the inherent phase lag is too high and would lead to oscillations. The control requires more complex filters, which are described in section 5.1.5. Here, the combination of a 1.5 kHz integrator and a 2.5 kHz lowpass leads to a fairly controlled system with a control bandwidth of about 500 Hz; its transfer function can be seen in figure 5.4. With more filters, the bandwidth can be increased further.

5.1.8 Going digital

Digital control loops enable a high flexibility in filter design, where even complex filters easily can be implemented and changed. Furthermore, integrations in other systems and extra functions, such as an autolock (section 5.2.5) are available. The main downside is the necessity of lowpass filtering of the input signal to avoid aliasing effects and, hence, additional phase delay. Due to the finite sampling rate of digital systems even more phase delay is added. Finally, the limited discrete resolution of analog-digital and digital-analog converters produces quantization noise, which can limit the achievable performance.

For digital control the continuous-time systems are transformed to discrete-time systems. The

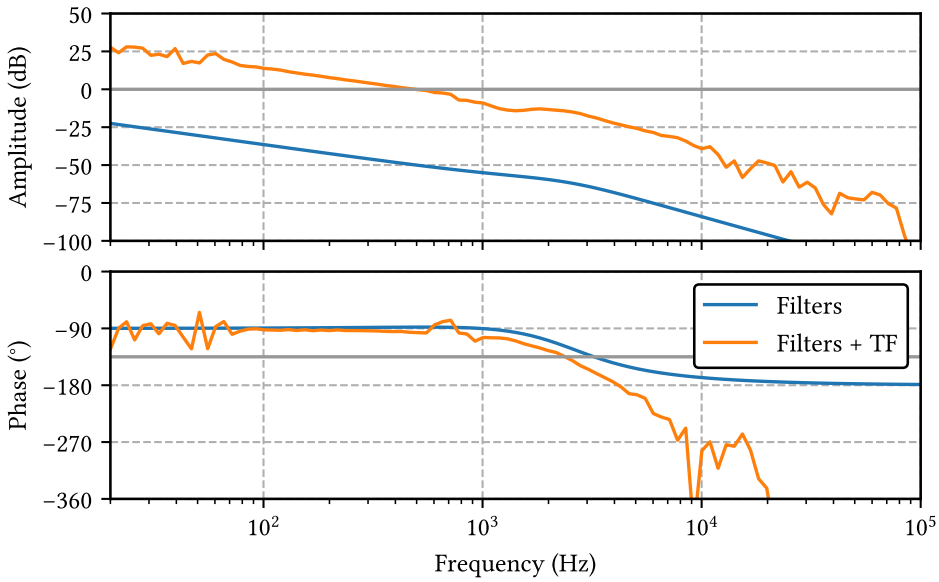

Figure 5.4: Transfer function (TF) with applied integrator (1.5 kHz), lowpass (2.5 kHz) and overall gain of −30 dB. Here, the plateau of the amplitude around 2 kHz prevented increasing the overall gain, as the system started to oscillate.

system state vector is now evaluated in time steps $x[n]$ to $x[n+1]$, where the time between the discretized steps from n to $n+1$ is the inverse of the sampling rate $T_{\text{sample}} = 1/f_{\text{sample}}$. Similar to the Laplace transform, for discrete systems the z-transform is used for a frequency-domain analysis

$$x(z) \equiv \mathscr{Z}(x[n]) = \sum_{n=-\infty}^{\infty} x[n]\, z^{-n}\,.$$

The discrete transfer function then becomes the quotient of polynomials

$$G(z) = \frac{y(z)}{u(z)} = \frac{\sum_{n=0}^{N} b_n z^{-n}}{1 + \sum_{m=1}^{M} a_m z^{-m}}\,.$$

Higher order systems can be broken down into consecutive sections of second order

$$G(z) = \frac{b_0 + b_1 z^{-1} + b_2 z^{-2}}{1 + a_1 z^{-1} + a_2 z^{-2}}\,, \tag{5.6}$$

normalized such that $a_0 = 1$.

5.2 NQontrol – A new open source digital control system

Usually, in our group the control loops for devices like mode cleaners and nonlinear cavities use analog servos. With those, the filter optimization process is rather slow, as it requires the change of electronical components to tune the parameters of advanced filters like for example a notch filter. Furthermore, for each new control loop a new analog servo is needed.

Therefore, I started a side project to build a digital servo control system that should be able to handle all control loops of the experiment. The core implementation of the second order sections, made by Sebastian Steinlechner and tested by Stephan Grebien, was already working when I adopted the project. I have mainly written the core Python interface, which is the base for the graphical user interface and provides a programming interface simplifying the process of measurement automatization in the lab. The GUI was primarily written by Luis Dekant and is an easy way to control the experiment for the standard use cases.

The main content of this section has been published Review of Scientific Instruments [Dar+20b].

5.2.1 Design considerations

Several considerations have influenced the design of our control system, which can be summarized as follows:

1. The control system should be based on an *established hardware platform*, commercially available and long-term supported, such that new systems can easily be set up for years to come.
2. A wide input voltage range, with differential sensing and standard connectors, should *not introduce new external interfacing* electronics.
3. Ideally, the system should *simultaneously support all locking loops* of an experiment, or be sufficiently modular to support those.
4. A *control bandwidth* (unity-gain point) of at least 10 kHz should be realizable, with *low electronic noise* and *high resolution* to be able to compete with analog designs.
5. The system should *operate in real time*, for deterministic behavior of the control loops with an amplitude-phase response that does not depend on system load.
6. Hardware *programming should be accessible* with little more than the standard programming training.
7. Control loop filtering should go beyond PID control, allowing for *arbitrarily defined biquadratic filters*.
8. There should be an *easy-to-use remote-control interface*, allowing quick results for daily lab work, as well as being accessible for continued development.

Based on items (1)-(5), we decided that a modular system with a dedicated, real-time processor would best fit our requirements. Such systems are e.g. based on the PXI platform, or vendor-specific implementations. Because of existing experience in our institute, we settled on the ADwin [Jäg] platform. This platform also mostly fulfills (6), as it is programmed in a relatively easy to use BASIC dialect and the development environment is easily set-up and well documented. Items (7) & (8) then are the design considerations for the software that we developed for this platform, and that I will further describe in the following sections.

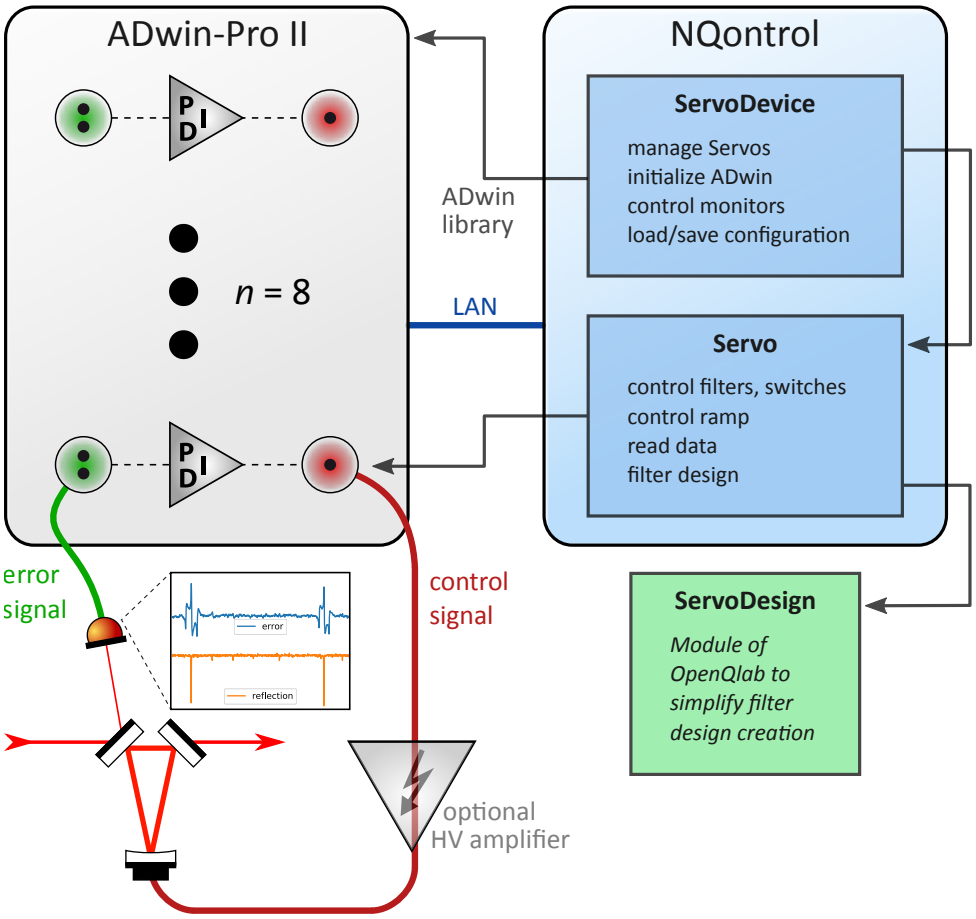

Figure 5.5: System overview to show the relations between the experimental control loop, the real-time system (ADwin-Pro II) and our software package. The real-time system runs independently and is accessible via local network. `NQontrol` changes the state of the real-time control loops and provides an interface for the user. It mainly consists of the classes `ServoDevice` that represents the whole real-time device and `Servo` which represents one of the eight controllers.

5.2.2 Implementation

System description

We use an ADwin-Pro II system with a 1 GHz ARM processor, 2×8 simultaneously sampling 16-bit analog inputs and 2×8 16-bit analog outputs. The system itself runs some variant of the Linux operating system, which is however inaccessible to the end user, and handles the ADwin-proprietary communication with the hardware modules. It also provides a shared memory region that is accessible to a connected computer through a gigabit Ethernet connection for fast exchange of data. On top of this software platform, our high-priority real-time control code runs with a fixed cycle frequency, which we chose to be 200 kHz.

The controller has eight independent control channels, each equipped with a filter module running as part of the real-time application. The filter modules each take two analog input channels and provide one analog output channel, depicted in figure 5.6. The input and output channels have a resolution of 16 bit, where the voltage range of the input channels can

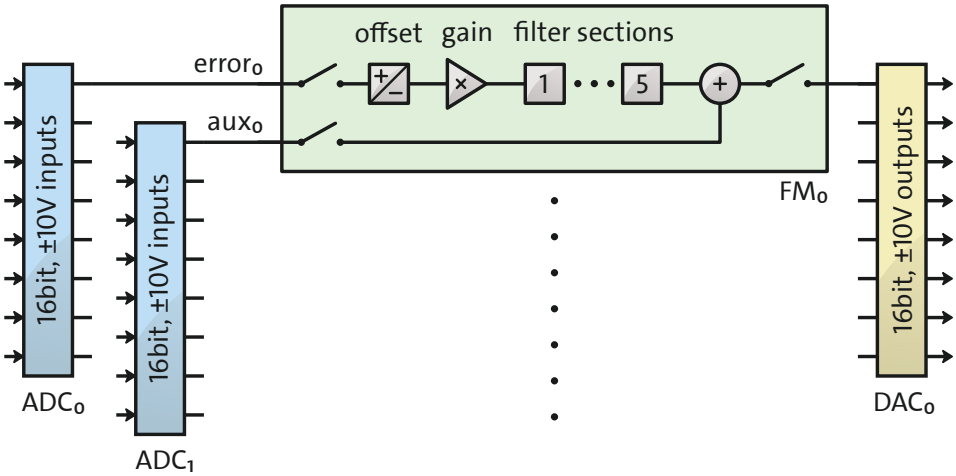

Figure 5.6: Block diagram overview of the individual channels in the digital control setup. Each of the eight channels provides offset correction, gain and a filter section. Additionally, an auxiliary signal can be added to the output, e.g. for frequency-response analysis.

be adjusted at four steps from ±1.25 V to ±10 V. One input channel is used for the error signal, while the other serves as an auxiliary signal that can be used for e.g. response function measurements, monitoring or as a trigger input for lock automation.

On the software side, the filter modules have enable switches for the inputs and output and offer offset and gain correction. They run with double-precision (64 bit) floating point arithmetic, to reduce rounding errors during the filter calculation. The actual filter response is given by five second-order sections, described below, that can be individually activated.

A user-selectable combination of signals can be sent to four additional analog outputs, such as a copy of the input, auxiliary and output channels, to allow for easy monitoring.

Second-order sections

The implementation of control filters on a digital real-time system requires a time-domain form of the corresponding discrete transfer function $G(z)$ from equation (5.6). We use second-order sections to calculate the filter output. A discrete linear time-invariant filter produces the output of the next time step given by

$$y[n] = \sum_{i=0}^{N} b_i x[n-i] - \sum_{i=1}^{M} a_i y[n-i] \,. \tag{5.7}$$

Using the coefficients of $G(z)$, the time-domain equation of a second-order section results in

$$y[n] = b_0 x[n] + b_1 x[n-1] + b_2 x[n-2] - a_1 y[n-1] - a_2 y[n-2] \,.$$

Our real-time code uses the *direct form II* for calculating the filter

$$y[n] = c_0\big(x[n] - (c_1 + c_3)w[n-1] - (c_1 + c_4)w[n-2]\big) \,, \tag{5.8}$$

using the five double-precision coefficients $c_0 = b_0$, $c_1 = a_1$, $c_2 = a_2$, $c_3 = b_1/b_0$, and $c_4 = b_2/b_0$, as well as two *history* variables $w[n-1]$ and $w[n-2]$, given by

$$w[n] = x[n] - c_1 w[n-1] - c_2 w[n-2]\,.$$

Software

Our software implementation consists of two parts: a high priority real-time process running on the ADwin device and a platform-independent Python program which controls the real-time process via a network connection, controlling its state and providing filter coefficients (see figure 5.5). Using this combination it is easy to change and optimize the control parameters via a standard computer that does not need to run a real-time operating system.

The real-time process is written in the ADbasic dialect required by the ADwin hardware system. This dialect provides a fairly high-level interface to the data acquisition and output cards. It is cross-compiled on a PC, resulting in an ARM binary that can run on the real-time core of the ADwin hardware. The core task of the real-time process is the continuous evaluation of equation (5.8) for each second-order filter section. Running at a fixed sampling rate of 200 kHz, the platform supports eight concurrently running loops, each with five individually configurable second-order sections, leading to a total of 40 sections.

Each sampling interval starts by reading in the current voltage levels at all input channels simultaneously. For each channel, a settable offset and gain are applied to the converted input values before the second-order sections are calculated. Each channel's inputs and outputs can be disabled if not used. Finally, the analog-to-digital converters are pre-populated with the resulting values and scheduled for automatic conversion at the beginning of each sampling interval. This way, timing jitter because of varying calculation time during each iteration is minimized. The real-time process can also provide triangular ramps with user-selectable frequency and amplitude for all channels. Several bit-flags control the status of each loop, such as whether specific second-order sections and inputs/outputs are enabled. These bit-flags, together with filter coefficients and ramp settings, can be set via the network interface. In addition, a subset of input and output channels are streamed via the network connection, for monitoring and recording. The traces are stored in a shared FiFo-buffer (first-in-first-out) which is accessible by the computer to read the data.

On the computer-side, our `NQontrol` Python package connects to the ADwin system and provides a high-level interface. It acts as an object oriented library with a simple structure: The `ServoDevice` represents one ADwin device containing eight `Servo` objects. Those servo objects correspond to a specific channel on the physical device and take care of the communication and monitoring with the real-time code. To simplify the creation of complex filter designs, each `Servo` contains a `ServoDesign` object that is implemented in our library `OpenQlab` [PDS]. It provides several convenience functions for creating sequences of filters with up to second order in pole-zero representation, such as integrators, differentiators, lowpass filters and notch filters. It will show a Bode plot representation of the filters' combined transfer function and can apply the filter to a (measured) transfer function of the plant, i.e. the system that is to be controlled. This allows for a quick iteration in optimizing a set of filters for the individual control task. We implemented the filter design part in continuous Fourier space, as this is the representation that is probably most common and familiar to physicists. The filters

are automatically transformed into their discrete form before being uploaded as second-order section coefficients into the real-time code.

For example, programming the first control loop to act as an integrator with a corner frequency of 5 kHz, then enabling the output and producing a triangular ramp with 30 Hz frequency is achieved with the following code sample. It will also open a plotting window on the computer, which will show a live update of the voltages appearing at the inputs and outputs.

```
from nqontrol import ServoDevice
device = ServoDevice(1)
s = device.servo(1)
s.servoDesign.integrator(5e3)
s.applyServoDesign()
s.outputSw = True
s.enableRamp(frequency=30)
s.realtimePlot() # running in a subprocess
# to prevent blocking the command line
s.disableRamp()
```

On top of the Python interface, we have created a web-based, responsive GUI using the Dash framework [Plo], providing an even higher-level interaction with the real-time control system. Through this GUI, no programming knowledge is required to use the control platform, further lowering the entry barrier to digital control in physics experiments. Both `NQontrol` and `OpenQlab` make heavy use of the Python libraries `numpy` [Oli06], `Pandas` [McK11] and `SciPy` [Vir+20].

5.2.3 Performance

To be an adequate replacement to analog control systems, the digital implementation should have a comparable performance. Important performance characteristics of a control system are robustness, noise suppression and recovery time from an external disturbance. To evaluate these properties on a realistic example for feedback control in quantum optics, we set up a test system in which an optical resonator is locked to a transmission maximum with sub-nanometer precision. This test system was then controlled with the digital control implementation presented here, and additionally with a conventional control loop employing analog electronics (operational amplifiers and discrete components) based on a design that has been in use in our group for many years.

System characterization

To determine the usable bandwidth of our control system, we measured its transfer function for a unity gain configuration (Figure 5.7). A significant phase lag of 45° is accumulated at a frequency of 10 kHz, while the amplitude stays flat for frequencies almost up to the Nyquist frequency (100 kHz), with a −3 dB point at around 80 kHz. As stated in section 5.2.2, to keep timing jitter to a minimum, the real-time code always uses a full computing cycle of 1/200 kHz = 5 µs for the filter calculations. A phase lag of 45° at 10 kHz corresponds to a time delay of 12.5 µs, thus another 7.5 µs of delay are added by the hardware conversion processes.

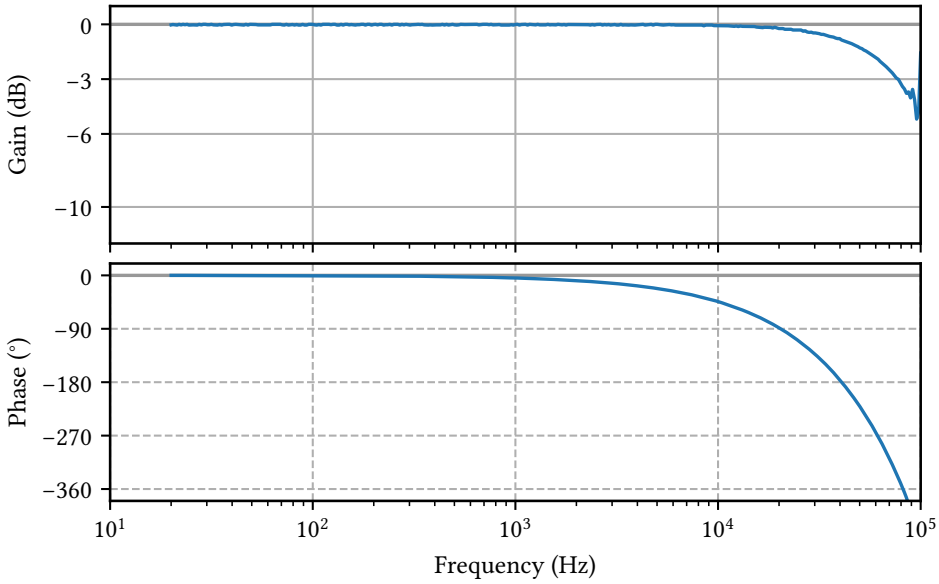

Figure 5.7: Transfer function (Bode plot) of the real-time system running at 200 kHz, for a gain setting of 1. From 10 kHz onwards, the phase delay exceeds 45° and limits the achievable control bandwidth.

For a required control bandwidth below around 10 kHz the phase delay only has a slight impact on the system performance.

In the same unity-gain configuration, we measured an output noise level of the system of 480 nV/$\sqrt{\text{Hz}}$ when the analog input was left open. The digital-to-analog conversion on its own showed a noise level of 260 nV/$\sqrt{\text{Hz}}$.

Test system

We used a triangular optical ring-cavity [Ueh+97] for the performance tests as it is a typical system where length stabilization to sub-micrometer accuracy is needed. The cavity had a round-trip length of 42 cm and a finesse of about 1000, leading to a FWHM linewidth of roughly 700 kHz. One of the cavity mirrors was mounted on a piezo actuator, which could be driven with 0 … 30 V for precise adjustment of the round-trip length. An error signal for keeping the cavity on resonance was obtained via the Pound-Drever-Hall (PDH) method [Dre+83]. Figure 5.8 shows the measured transfer function of the cavity setup itself. Since this transfer function can only be measured when the cavity is already held on resonance, `NQontrol` was used to obtain an initial unoptimized lock. Then, a swept-sine signal was added onto the piezo actuator drive voltage and its response function to the system's error signal was measured. Dividing this response function by the combined drive voltage results in the desired transfer function of just the cavity system by itself.

Using the measured transfer function, we designed a combination of control filters that together provide high gain at low frequencies and cross the unity-gain point (0 dB) with a phase margin of more than 45° to the phase delay of 180° which would lead to an amplification of disturbances. The unity-gain frequency should be as high as possible and at higher frequencies the gain should stay well below 0 dB to avoid an unstable, oscillating system. Using those base

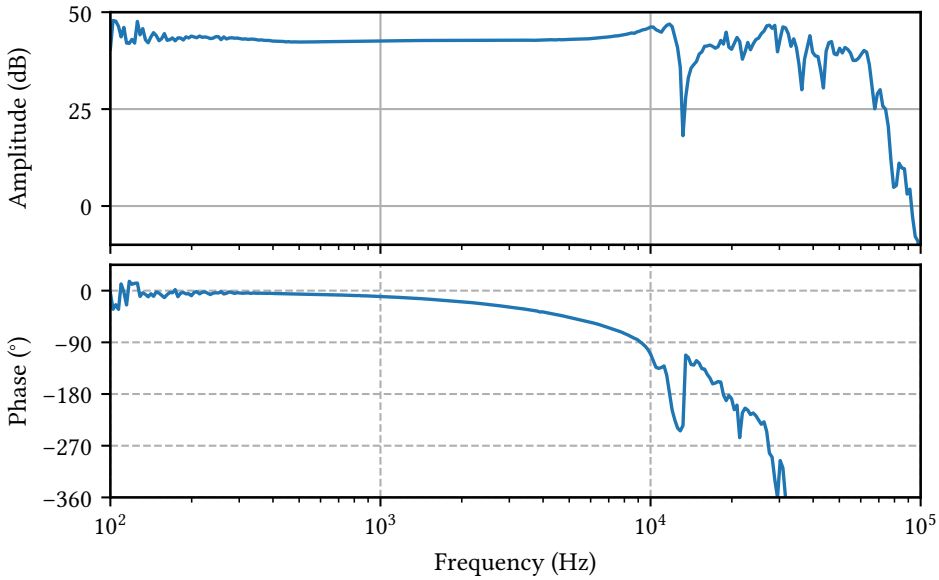

Figure 5.8: Bode plot showing the transfer function for our test system. Below 10 kHz the response is rather flat, but at higher frequencies the system possesses dispersion-shaped mechanical resonances. Their associated phase delay makes it practically impossible to achieve stable control beyond 10 kHz and limits the achievable control bandwidth to several kHz.

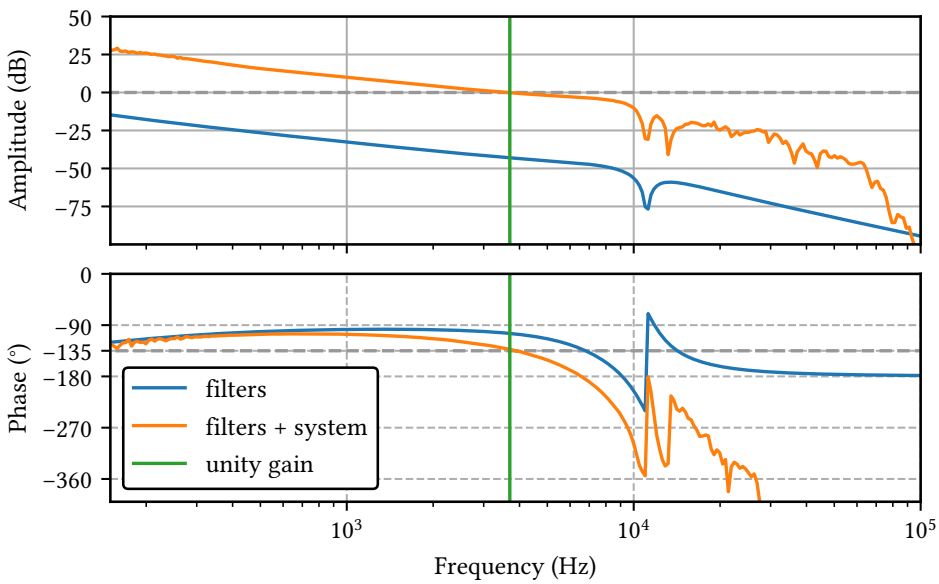

Figure 5.9: Bode plot of the designed filters as given in table 5.1 for the control of our test system (blue). The orange curve shows the calculated combination of these filters together with the transfer function of the test system (see figure 5.8), i.e. the overall open-loop transfer function of the control system. This design achieves a 3.7 kHz control bandwidth (unity-gain crossing) with a phase margin of 45°. The unity-gain level and −135° phase delay are indicated by the dashed grey lines.

Table 5.1: Filter design values used for controlling our optical cavity test system, with corner frequencies and quality factors, where applicable.

implementation	filters
digital	integrator 100 Hz integrator 10 kHz 2nd-order lowpass 9 kHz, $Q = 1$ 2nd-order notch 11.1 kHz, $Q = 1$
analog	integrator 100 Hz integrator 4 kHz 2nd-order lowpass 9 kHz, $Q = .707$ 2nd-order notch 11 kHz, $Q = 1.5$

assumptions, the filter design was tested on the real cavity and has been further optimized for low amplitude noise behind the cavity. The resulting filter design and a combination with the system response can be seen in figure 5.9 and the corresponding values in table 5.1.

Because of the additional phase delay from the digital feedback loop, the chosen filter values were not the same for the analog and digital implementation, but optimized for each case.

Comparing implementation performance

A control system can be characterized by its response to an external disturbance, e.g. by a step-like change in one of the system parameters. The quality of the feedback is determined by the time the control system needs to reach the set point again, and whether it is prone to overshooting and oscillating around the set point. In our cavity test setup, we implemented such a step response by adding a 100 mV step onto the voltage of the piezo element. Measuring the power in transmission of the cavity, this caused a drop down to about 20 % of the transmission compared to the value on resonance. The response to this step for both the analog and digital implementation is depicted in 5.10. Both controllers were able to cope with the disturbance and the system settled again within less than 0.5 ms.

Another key characteristic of a good control system is noise on the controlled quantity, i.e. how well external disturbances are reduced, and how little additional noise is introduced by the control and sensing system itself. In our case, a good (out-of-loop) noise figure was the amplitude noise on the transmitted light through the cavity, expressed as relative intensity noise $\mathrm{RIN} = \Delta P/P$. For an ideal, noiseless control loop, this amplitude noise would have equaled the amplitude noise on the laser light before it entered the cavity. This is the baseline measurement indicated in 5.11 as *laser noise*. Environmental noise (acoustic noise and cross-coupling of laser phase noise), control noise (from electronics and the piezo element) and sensing noise (from the PDH photodiode) added onto this baseline, resulting in the noise measurement after the cavity. We compared the noise level obtained with our conventional analog control circuit with the digital system and obtained similar results. At frequencies below 5 kHz, both control implementations were most likely limited by sensing noise, as evidenced by the fact that further increasing the gain actually increased the noise level. Above 5 kHz, the digital

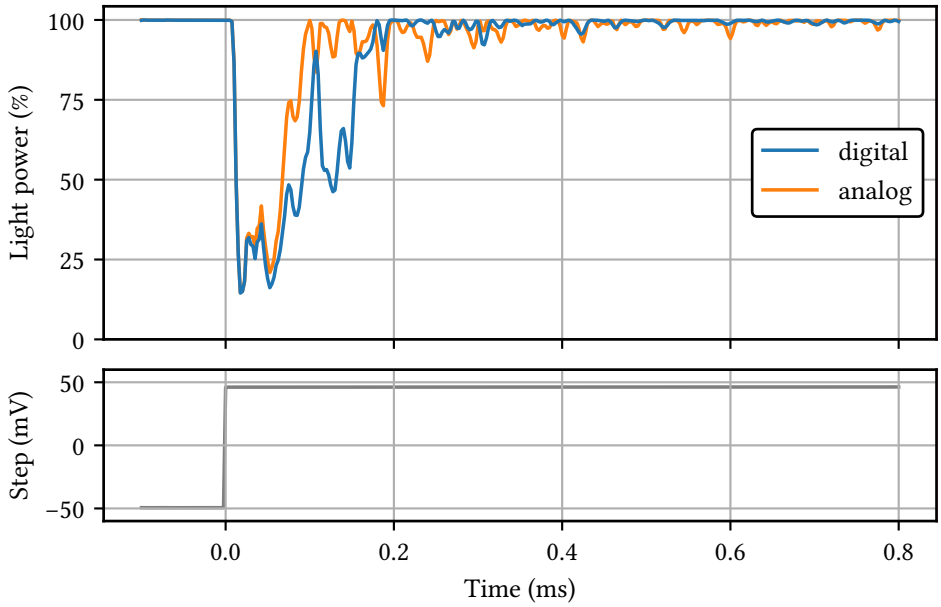

Figure 5.10: Step response of digital and analog control implementation to a 100 mV step in piezo voltage occurring at $t = 0$ s. Both systems settled back to nominal transmitted power after less than 0.5 ms.

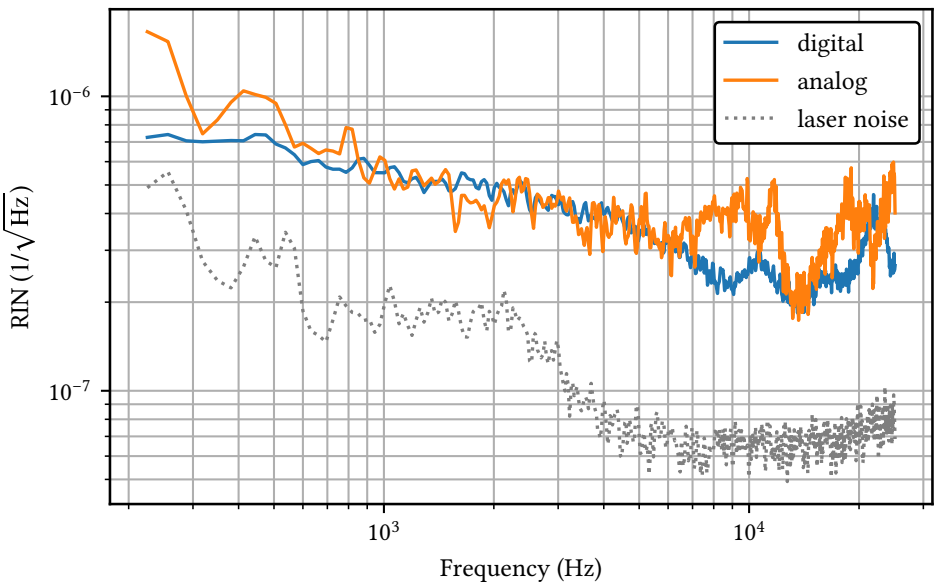

Figure 5.11: Measurement comparing the relative intensity noise (RIN) levels of digital and analog implementation for our test setup. For all measurements, the same light power was detected ($U_{\text{pd}} = 6.13$ V, equivalent to about 1.4 mW). At the measurement frequencies, the laser was not shot-noise limited. Photodiode dark noise was at least one order of magnitude below the measured values and thus not subtracted.

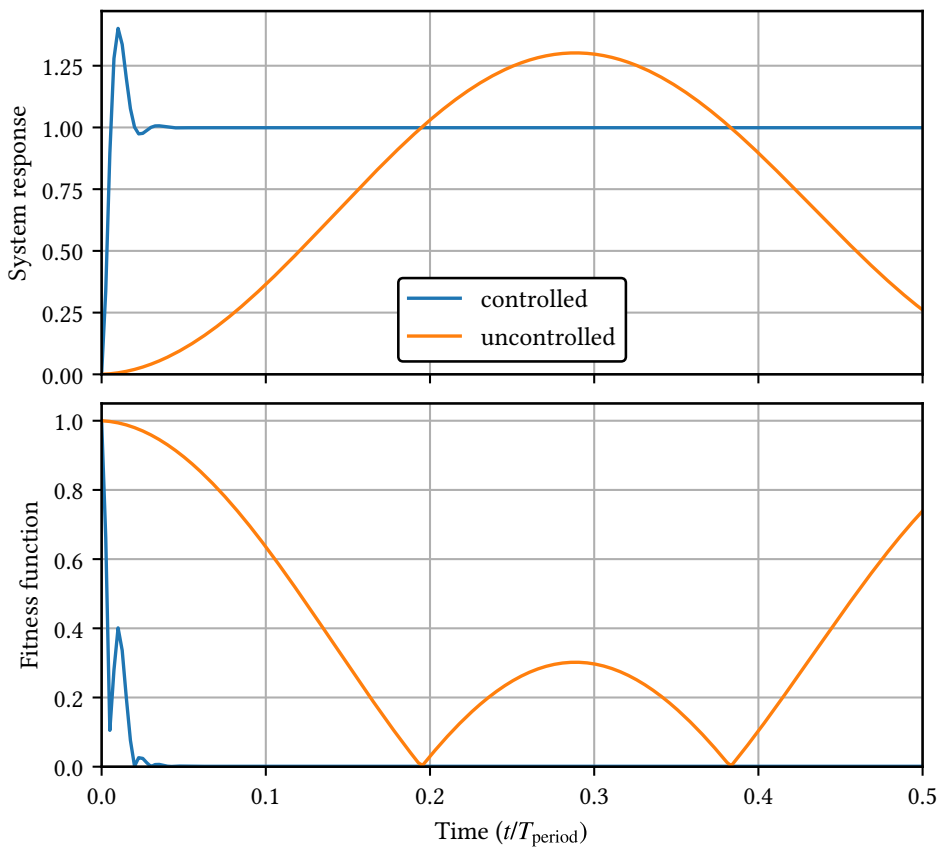

Figure 5.12: System responses to a step function which changed the set point from 0 to 1 at $t = 0$ to compare a controlled and an uncontrolled harmonic oscillator. On the bottom the results of the fitness functions are shown, quantifying the deviation from the set point. For evaluation of the filter performance, the fitness function is integrated over time.

control implementation was less noisy. This might be explained by a slightly detuned notch filter in the analog implementation, because of component tolerances and their temperature drift. Here, the flexibility and quick turn-around time of filter adjustments in the digital control system came to full strength. More importantly, however, we were able to show that the digital control system did not introduce additional noise from the analog-digital-analog conversion steps and is therefore a suitable replacement for analog controllers in the feedback control tasks of our experiments in quantum optics.

5.2.4 Filter design automation

Even when working with a flexible digital system the filter design is a complex task, requiring much experience to get fast and robust controllers. Thus, the idea rose to automate the optimization task and I supervised Luis Dekant in his Bachelor thesis [Dek19] in a project to examine optimization algorithms for filter design. Automation options were explored in the scope of the thesis on how an implementation in NQontrol would be possible.

The general concept is to define a fitness function

$$J = \int_0^t |e(t')|^\alpha \, \mathrm{d}t' \,,$$

which crunches the overall rating of the controller down to a single value that should be minimized. It evaluates the error in a time range from a disturbation event to a specified time t. Either a δ peak or a step function can provide as testing disturbation. Figure 5.12 shows two example step responses with the corresponding fitness functions. The fitness function crucially defines the *optimal* behavior of the control system. As discussed in sections 5.1.3 and 5.1.6, there is a trade-off between sensor noise and disturbance suppression, as well as the needed duration to respond on set point changes versus noise suppression. Hence, the exponent α : ($\alpha > 0$) can be used to choose if the filters should be optimized for fast response ($\alpha > 1$) or for low noise ($\alpha < 1$).

Now having defined, what *optimal* control means for the specific system, an optimization method is required to find the best filter parameters. As NQontrol uses five second order sections, each having five parameters, there are 25 continuous variables which need to be optimized to find the global minimum. Of course, there is not *one single* global minimum, because the transfer function is invariant to filter positions. There are two approaches to run the optimization algorithms: The usage of a virtual model of the system, where a δ or step function is calculated and applied to the fitness function or the direct optimization of the real system, where the answer on the step function is directly measured and similarly evaluated.

Simulations

Simulating a system is the straight-forward way to test algorithms, combining the advantage for being able to make calculations in parallel and hence to speedup time needed for optimization. Within the Bachelor thesis mainly a primitive test system was chosen as model for optimization algorithms: A harmonic oscillator with the differential equation

$$x(t) + \frac{b}{m}\dot{x}(t) + \frac{k}{m}\ddot{x}(t) = \frac{u(t)}{m} \,.$$

Here, it was enough to have one single second order filter with its five variables to get a well controlled test system. This simple system can remain in a controlled state with extremely high gain that would be unrealistic for real systems as they would need enormous powers and sensor noise would be highly amplified. Consequently, we modified the fitness function to add a gain-dependent noise term

$$J = \int_0^t \left(|e(t')|^\alpha + a \cdot |g e_s(t')| \right) \mathrm{d}t' ,$$

with the gain g, the weight a and the noise term $e_s(t)$. To be able to run the filter optimization via simulation for real systems, a variety of preconditions need to be fulfilled:

- The noise term has to be similar to the real noise.
- The filters have to be limited to realistic system boundaries, especially limited control currents.

- The modeled representation of the real system is critical and needs to match the real system very well.

To optimize a system through simulations, a state-space model needs to be generated from a measured transfer function. Especially fitting the transfer function of a real test cavity has shown to be limiting. We tested this way of fitting the transfer function with Matlab which resulted in a good-looking fit with 12th order and it was possible to algorithmically find optimized filters for a well-controlled simulated system. But, nevertheless, neither working filters of the real system led to a controlled simulated state, nor the other way around. As a consequence, the most promising approach seems to be to use the simulation only for testing of algorithms and to follow an automation approach, in which a real system is optimized starting from roughly working filters.

Optimization algorithms

Here, I will give a tiny overview of optimization algorithms used by Luis Dekant. As stated before, the main difficulty is to find the global minimum in a huge unknown landscape. Considering the 25-dimensional parameter space, it is obvious that we cannot guarantee to find the global minimum, but just to find a reasonably optimized point. It hence makes sense to use a known starting point or to use the system knowledge to define feasible parameter boundaries. For example, any pole or zero belonging to frequencies beyond the sampling rate is useless to consider in the parameter range. Furthermore, the real part of any pole or zero must not be positive, as it leads to an intrinsically unstable system. The following algorithms were tested in the Bachelor thesis:

Basin hopping [WD97] was used for the first tests, because of the simple usage and the integration in SciPy. It is a combination of a random walk with local minimization. Starting from an initial point, it makes a random displacement step and then uses a local minimizer. This local minimum is compared with the previous and depending on its value accepted or rejected. A *temperature* parameter defines how likely a new local minimum is accepted if the function value is higher than before. That approach allows a broader minimum search when the optimizer is in an area of small local minima. For the local minimization, different algorithms can be chosen, such as Newton's method or gradient descent. The optimization is finished when the global minimum candidate stays the same for a specified number of iterations.

Particle swarm optimization (PSO) [KE95; SE98] was used as a comparison and to have an evolutionary algorithm, because they tend to converge to robust solutions. Here, the swarm consists of N particles which all have a vector position in the (25-dimensional) parameter space and a velocity. The first positions are randomly selected and the velocity is selected based on a *personal experience* and *swarm experience*. Then, the position of a particle at the next time step $n+1$ is evaluated with

$$\vec{x}_{n+1} = \vec{x}_n + \vec{v}_{n+1} \,.$$

For each particle the optimization function is calculated and the new velocity vector is chosen such as

$$\vec{v}_{n+1} = \vec{v}_n + c_k \cdot r_1 \cdot (\vec{p}_{\text{best}} - \vec{x}_n) + c_s \cdot r_2 \cdot (\vec{g}_{\text{best}} - \vec{x}_n)\,,$$

where $\vec{v}_n$ is the previous velocity of the particle. Furthermore is $\vec{p}_{\text{best}}$ the personal best position of the particle, $\vec{g}_{\text{best}}$ is the best global position. With the cognitive factor c_k and the social factor c_s, the behavior can be tuned to be more personally or more socially optimized. The factors r_i are random weights.

Now, the algorithm can be differentiated in the two variants *local* and *global best* PSO, with a continuous transition. In the local version, neighbors are defined and instead of using the global best position $\vec{g}_{\text{best}}$ only the best position of the defined neighborhood is used. The global best PSO converges faster whereas the local variant is less likely to oversee a global minimum.

When applying to NQontrol, the PSO needs be used with useful boundaries to provide a manageable parameter space. Then, it provided fast and reproducible results for the testing harmonic oscillator with one second order filter. For the adaption to real systems, the number of particles has to be much higher than the 25 dimensions and a reasonable number of neighbors has to be found, depending on the optimization time to spend. Additionally, for the real system with noise and sometimes inaccurate measurements, modifications are necessary that prevent the algorithm from choosing a good result that was only measured once. Tests with PSO and a temperature controller showed that the proposed *optimal* results usually were one-time measurements that had the lowest noise by chance, which was not reproducible. Such measurements can be avoided by using a very long measurement duration of the fitness function or, better, by implementing a finite history where only the best positions of the previous N iterations are taken into account.

Performance of optimization algorithms

Both presented algorithms were tested for performance and reliability using optimization runs for ten randomly selected harmonic oscillators. The algorithms optimized the control filters for each system ten times to produce reliability statistics. Figure 5.13 shows the progress of the optimized fitness function and figure 5.14 the corresponding step responses of the final results. Both algorithms usually find good control filters for the test systems, but the particle swarm is more reliable and usually faster. Basin hopping often needs less steps, but sometimes hangs in local minima without finding a globally good minimum. Furthermore, it is critical with the algorithm to find proper optimization parameters for step size and temperature to get valuable results. To sum up, an algorithm like the particle swarm is a good starting point for optimization of control filters.

Adaption on real-world systems

The adaption of automatic filter optimization on real-world systems solves the issue of imperfect model building, but at the same time creates novel challenges. First, the initial state – in simulations always perfectly defined – has to be reproducible and well-defined withing a huge number of repetitions. For a system like an optical cavity it has to be in a controlled state, which requires monitoring of the locking state and reliable relocking (see section 5.2.5).

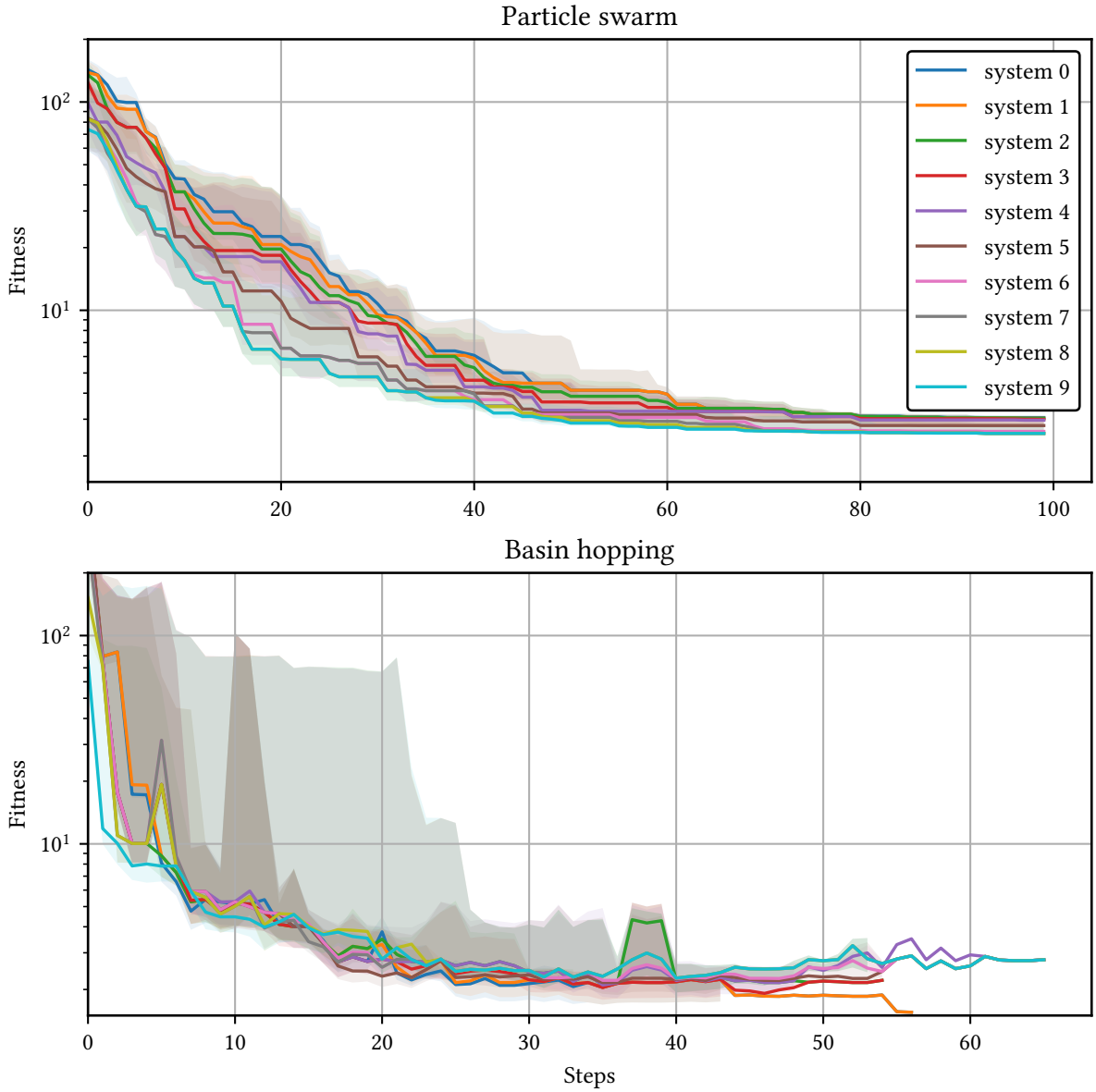

Figure 5.13: Fitness history (lower value is better) of both optimization algorithms for ten different systems and ten runs per system. The median fitness is shown with the lines and the shadow is the standard deviation of all runs of a system. As the algorithms are too different, the number of steps cannot be compared between them. The particle swarm was running with useful physical boundaries for the systems, as the parameter space would otherwise be infinite (except for the limited size of data types in computers). The basin hopping was started with an uncontrolled initial state within these boundaries. Basin hopping sometimes found better solutions, but often returned unusable control filters. When starting with a controlled initial state, the results are better but still fail sometimes to control the system. The particle swarm optimization was more reliable and always found good filters.

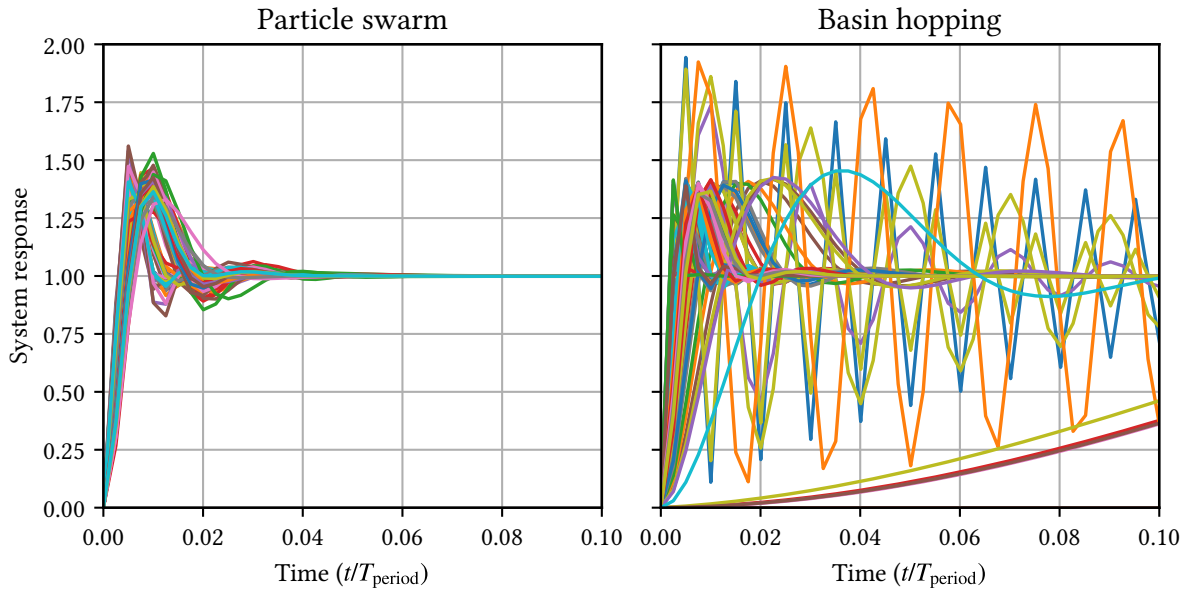

Figure 5.14: Step responses of all optimized results. Here is clearly visible that the particle swarm was always able to find a well-controlled state, but basin hopping sometimes failed completely. Basin hopping has more critical parameters (such as step size and temperature) to tune and is prone to stay in local minima.

Then, even for the same parameters, the step answers and, consequently, the result of the fitness function varies from time to time, as real systems have noise and fluctuations. This makes the usage of many optimization algorithms impossible, especially if they try to find the optimization direction with very small parameter changes. Some algorithms calculate the derivative between two close points to determine the optimization direction. As the result for small parameter differences is mainly dominated by noise, they would often run in random directions. Additionally, the algorithm should be appropriate for a global minimum search and should not stay in a small local minimum. And to reach robust control, small changes in system parameters should not lead to oscillations or the complete loss of control.

To sum up, evolutionary algorithms seem to be the method of choice, as they in general optimize for robust systems with good performance. If individual solutions show high performance, but small deviations lead to loss of control, they are likely to not reproduce over multiple generations. Running the optimization algorithms on real systems would be extremely slow if one wanted to find the global optimum of 25 variables, while the repetition rate to test filters would be around 1 /s to 10 /s to have sufficient time for the measurement and eventually relocking. A promising approach would, therefore, be to use roughly working filters as starting point and let the algorithm optimize it for some hours or over the weekend.

5.2.5 Autolock

If we consider the optical cavities from the experiment, we see that the assumptions of LTI systems are not fulfilled in general. If huge signals are applied (superposition of multiple low-amplitude signals), the cavity runs completely out of resonance and looses its controlled

state. To solve that issue, we programmed an autolock feature which brings the system back to control and the linear regime. The autolock proved to be a requirement to deal with the instability of the degeneracy of the down-converted light during lab work, where pushing the table was the method of choice to get degeneracy again. A manual relock each time would have hindered many measurement improvements.

The implemented autolock algorithm requires a monitoring signal from which the system can determine whether the cavity is locked or not. Here, the DC signal of the locking photodiode is sufficient and needs to be plugged into the auxiliary input of the specific NQontrol channel. The autolock scans the ramp with the previously selected parameters frequency, amplitude and offset until a specified threshold value is reached and the lock gets activated. Being able to select amplitude and offset allows to preselect the correct cavity peak and to speedup the lock-finding process. Now, if the relock is enabled, it permanently monitors the DC signal and, if it gets below a lower threshold value, activates the peak finding search again. To find the correct values for both thresholds, a scan over the whole selected amplitude range can be triggered. It looks for the highest peaks and selects 80 % of the maximum for the upper and 60 % for the lower threshold. Photodiodes often have negative voltage outputs, which is why the analysis can automatically detect positive and negative peaks.

5.3 Raspitemp – A digital temperature control system

I had the opportunity for a half-year extra project to develop a precise digital temperature control system that is able to handle all temperatures on a typical laboratory table. Previously, we used self-built analog controllers in our group, one for each temperature. That leads to a large footprint and requires to build each controller manually. The typical commercial systems are either for only one or two temperatures, not precise enough or extremely complex and expensive. Therefore, I developed a system combining precision with scalability, which should fulfill the requirements presented in the next section. At the moment, it is used to control all temperatures of both nonlinear cavities in our experiment; however, it can easily be extended to further temperatures if this is required for the experiment.

5.3.1 Design considerations

The developed temperature control system should fulfill the following experimental requirements:

1. It should be a modular system which can easily be extended to control all temperatures on a typical experiment.
2. A digital system should provide easy control with a computer via local network.
3. The temperatures should be controlled with an accuracy of less than 10 mK.
4. A programmable interface should be provided for easy measurement automatization.
5. A graphical user interface should simplify the everyday usage.
6. For typical nonlinear cavities the temperature range should be from about 15 to 60 °C.

The setup is based on a digital microcontroller that communicates via serial connection (UART) and handles the PID control autonomously. This way, only the modularity and the controlling interface for the user have to be developed.

5.3.2 Implementation

The temperature control system is based on the temperature controller *MTD415T* by Thorlabs, which is a digital PID controller with a serial connection to change settings. It needs a 5 V power supply providing a current of 1.5 A. The temperature is measured with an NTC having a resolution of 1 mK. It is designed for the 10 kΩ thermistor *TH10K* and provides a temperature range from 5 to 45 °C, but can be extended, see section 5.3.2. We use a Raspberry Pi 3B+ (in the following abbreviated as Raspi) as interface between the serial connections to up to twenty MTDs and the local network. As the Raspi only has one UART interface, the GPIO pins in combination with multiplexers are used. Often, several temperatures need to be controlled very close to each other. Hence, up to four MTDs share one circuit board in a

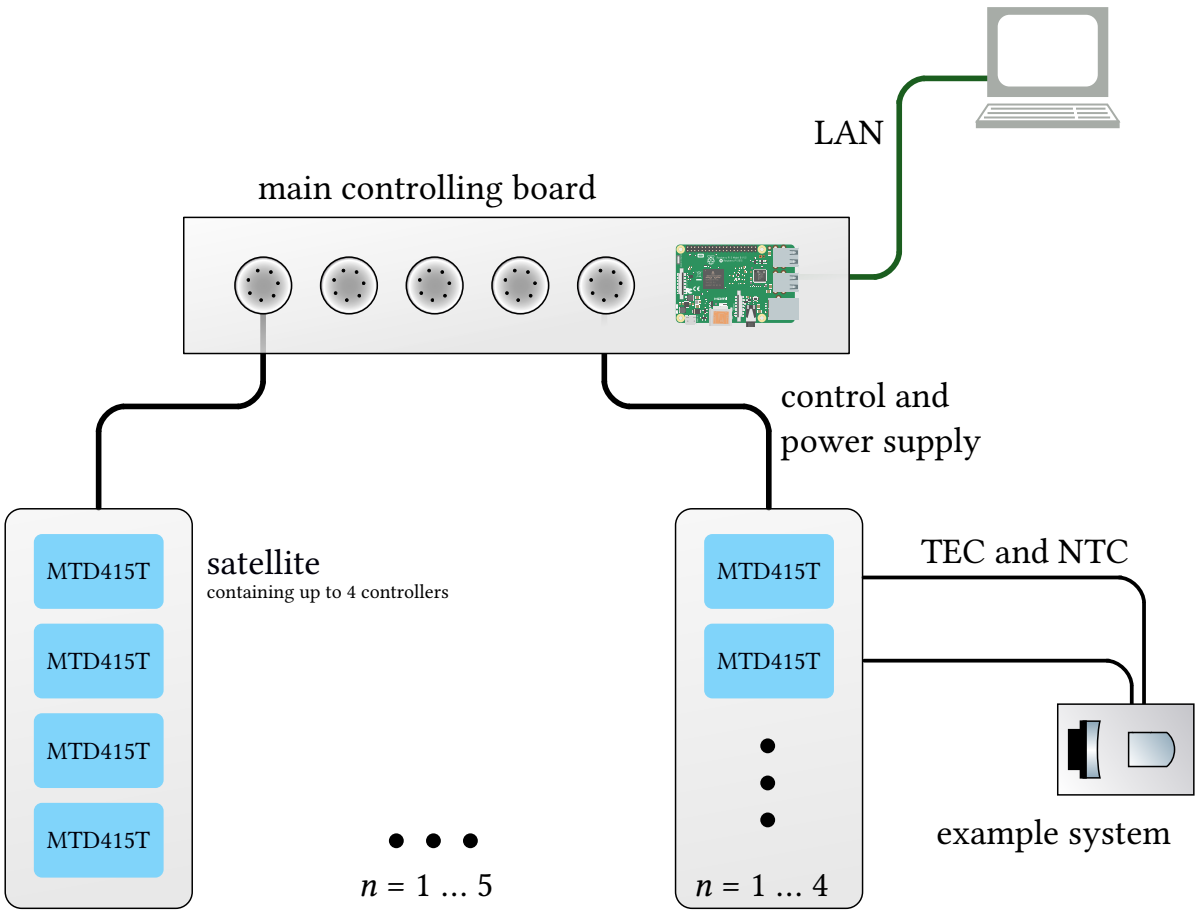

Figure 5.15: System overview of Raspitemp. Up to five satellites can be controlled by one Raspberry Pi sitting in the main controlling board. The whole setup is controlled via LAN, with the Raspberry Pi providing a management webpage. Each satellite is connected with only one network cable, which provides the power and control signals. Up to four temperature control microchips of the type MTD415T can be used in a satellite, providing a default temperature range of 5 to 45 °C. (Raspi image from [But16])

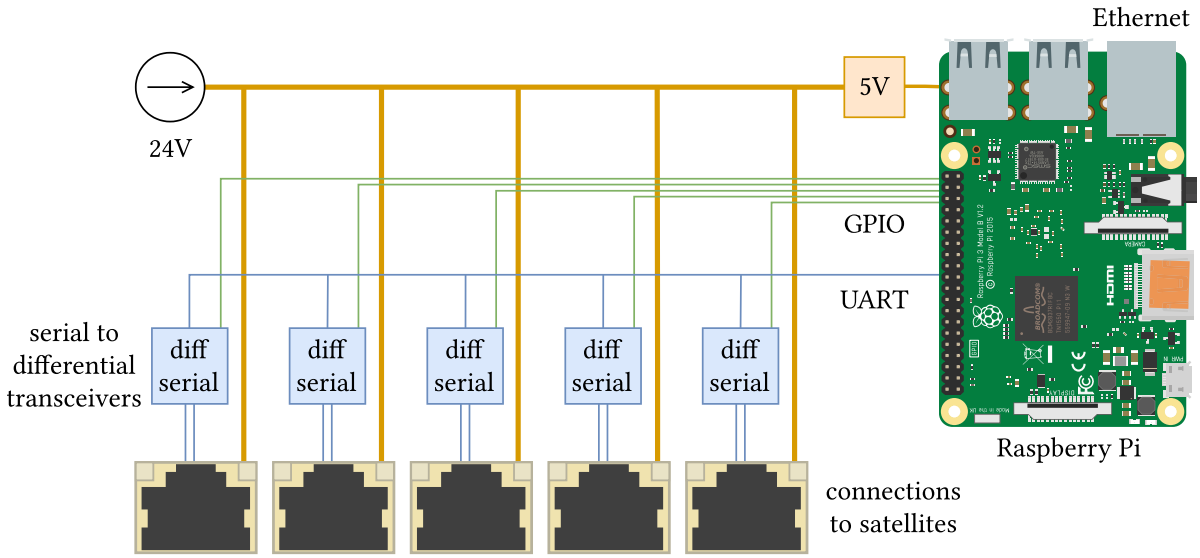

Figure 5.16: Main controlling board overview. The 24 V of the power supply are distributed to the satellites and converted to 5 V for the Raspi. As the Raspi only has one UART interface, it is connected to all satellites through serial differential converters with switching option. Those enable UART signal transmission to one single satellite at the time, activated using the Raspi's GPIO pins.

Figure 5.17: Main controlling board in the rack. The grey cable in the left is the local network connection, the five RJ-45 sockets are for the satellite connectors. The case contains a 24 V, 75 W power supply, a Raspberry Pi and a circuit board.

satellite which only needs one cable connection. Up to five satellites can be connected to the main controlling board. In the default configuration, a Jupyter server runs on the Raspi which provides both a graphical user interface and a Python programming interface which can be used simultaneously with the GUI.

Main controlling board

The main controlling circuit board (scheme shown in figure 5.16) enables the Raspi to orchestrate all the satellites and their temperature controllers. It provides a way to choose the satellite to talk to, as the Raspi only has one serial UART interface. Using programmable GPIO pins, the Raspi can enable and disable the line transceivers that forward the serial commands through the cables to the satellites. Furthermore, the circuit board delivers the 24 V voltage source to all satellites and provides the required 5 V to the Raspi. The circuit board, together with the power supply and the Raspi, is placed in the rack housing, which can be seen in figure 5.17. Additional details are visible in the schematics in appendix B.

Satellite

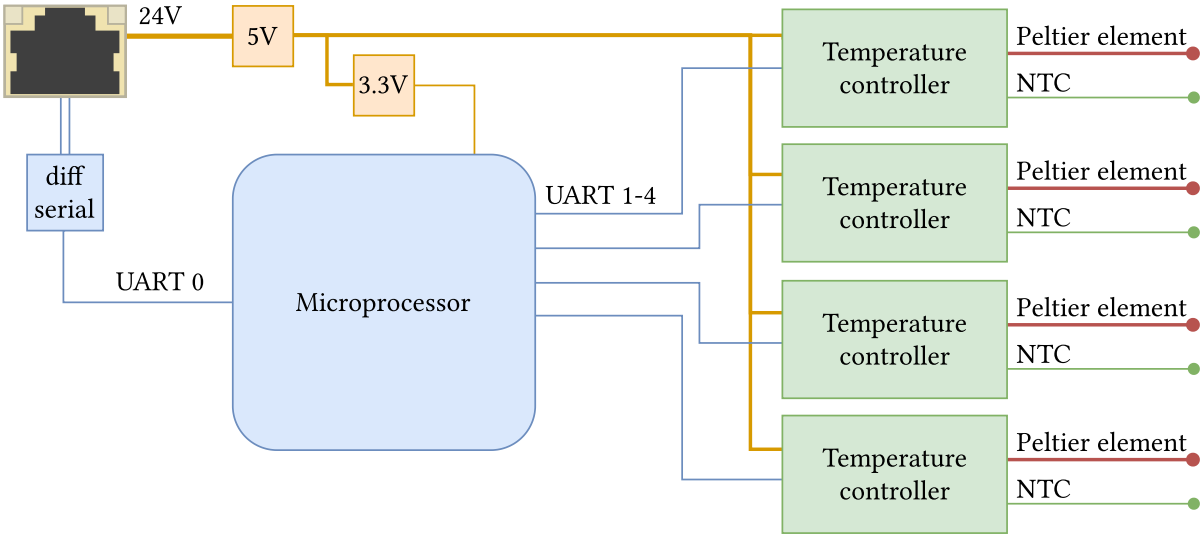

Figure 5.18: Overview of the satellite. The common single connector is used for power delivery and signal transmission Two DC-DC converters provide the voltages required for the temperature controllers and the microprocessor. The microprocessor, having five UART interfaces, acts as a demultiplexer and controls the communication to the different temperature controllers. Each temperature controller can be connected to a temperature sensor (NTC) and a peltier element, serving as actuator.

The modular satellite allows to control up to four temperatures in a small area, requiring only one single Ethernet cable for power delivery and controlling communication. Using 24 V for the power transmission enables powering four temperature controllers using thin network cables with more than 10 m length. Logical core of the circuit board is the microprocessor Atmel XMEGA 16A4U with five serial UART interfaces. It acts as a demultiplexer to deliver the commands to all temperature controllers using only one single communication channel to the Raspi. Figure 5.18 shows a schematic overview of the components on the satellite, while in figure 5.19 the real circuit board is shown with all its components.

Power delivery and data connections

A main issue is to provide the current for all MTDs without a critical voltage drop, while using long and thin standard cables. If all twenty MTDs run at full power (which could happen on startup) a current of 30 A could be drawn. The power issue is solved combining two approaches: The main power supply[1] uses 24 V and the voltage is converted to 5 V for the Raspi and on each satellite using small DC-DC converters[2]. This way, the currents in the long and thin wires are reduced and the voltage drop becomes irrelevant as the input voltage of the DC-DC converters only needs to be more than 6.5 V. But, even when using 24 V, the power can in principle be too high for the 75 W power supply and for the small 3 A DC-DC converters. As the overload of power supply and voltage regulators is not critical for the components, I solved it with a software implementation. Each time the maximum current for a MTD is

[1]Traco 75 W, 24 V DC switching power supply
[2]Gaptec LC78_05-3.0 DC/DC switching voltage converter, 5 V, 3 A

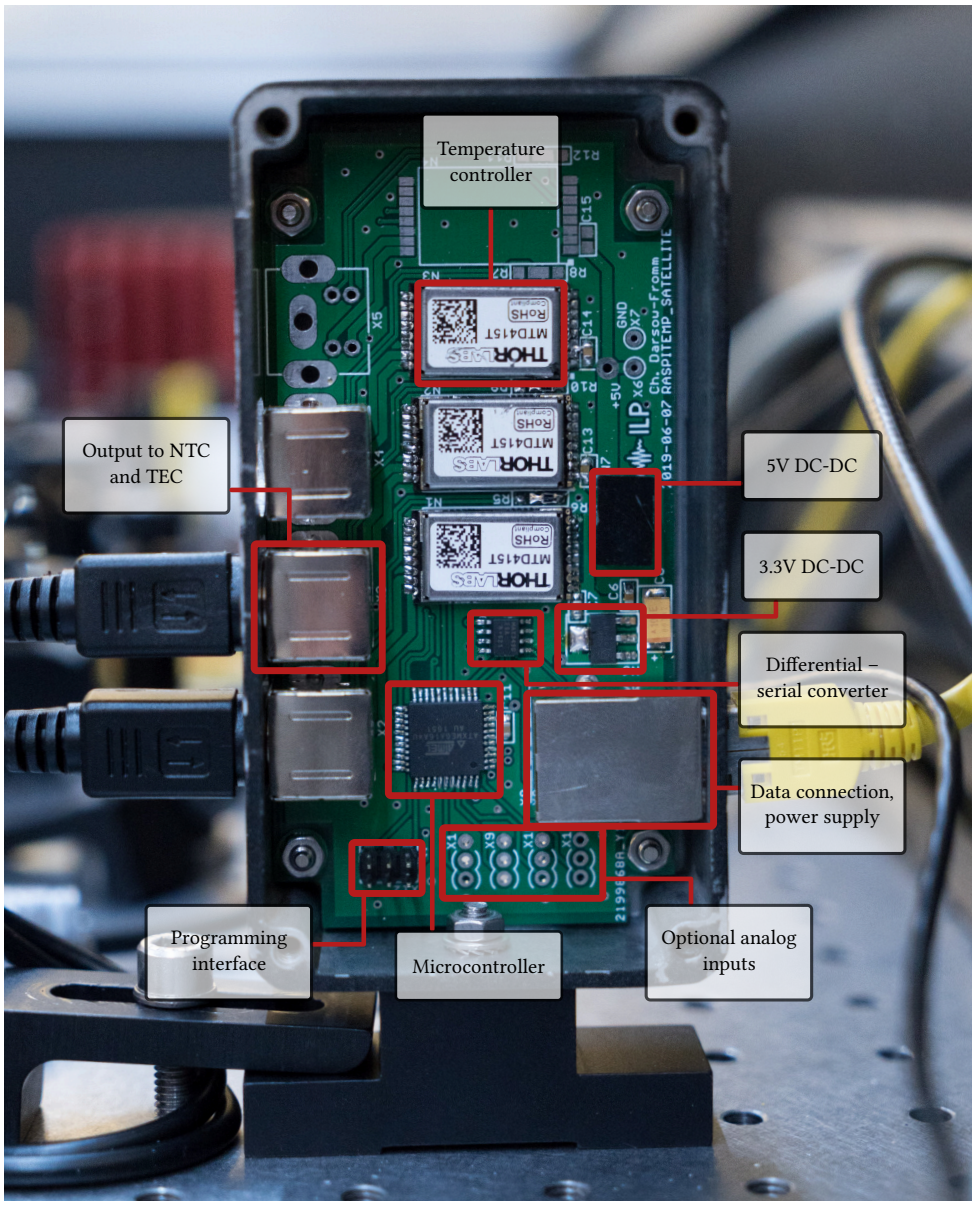

Figure 5.19: Opened case of the satellite that controls the squeezer. The microchip handles the communication to the different temperature controllers. In this case, two temperatures are needed for the nonlinear cavity and a third spare MTD is soldered on the circuit board. On the left is space for up to four Mini-DIN (S-Video) connectors for the NTC/TEC connections.

set, it is checked if the satellite limit of 3 A or the total limit of 12 A (corresponding to 5 V) is exceeded.

For the connection between satellites and main controlling board, standard LAN cables (RJ-45) are used. They have the benefit to be easily and everywhere available, having eight wires and a proper shielding. The combination of power supply and data connection is based on the simplest Power over Ethernet (PoE) specification. It uses each two wires for plus and minus of the power supply and two wires for the differential connection in transmission and receiving direction of the data. To avoid unnecessary complexity, the PoE specification is not completely fulfilled and the connected device is not checked for compatibility before supplying the power.

As the data connection is not using Ethernet, a compatibility to PoE is not required. Also, the voltage of 24 V is below the specified range of 37 V to 57 V. By this deviation from the PoE specifications, we avoid to destroy PoE compatible and even most PoE-incompatible devices that are mistakenly connected. In a controlled lab environment I think it is acceptable.

For the connection of NTC and peltier element (TEC) a four-wired cable is used with an easy connector and a small footprint. We decided to use Mini-DIN 4 which is also known for S-Video cables. This way one connection is enough for temperature sensor and peltier element which are soldered to the end of the cable.

Serial communication

The communication between Raspi and the MTDs is established via a serial connection using UART interfaces. A first attempt was the usage of a direct connection, where both devices share a common ground and the transmitting (Tx) output is directly connected to the receiving (Rx) input of the other device. It turned out that this simple approach only works if short cables (less than 1 m) are used. Otherwise oscillations of the signals occur, caused by the capacity of the cable, which even destroy the serial interface of the Raspi.

To protect the Raspies and to make the communication more reliable, the design was changed to differential communication. Here, the signal is split into a Tx+ and Tx- part (Rx+, Rx-) and the signal is high if Tx+ > Tx- and low if Tx+ < Tx-. The benefit of differential communication is that noise and disturbances act an both wires the same way, which does not affect the difference between the signal and makes it very resistant to noise. The other, for our setup more important, advantage is the possibility to match the impedance to avoid back reflections of the signal. Impedance matching is achieved using a 100 Ω resistor in the input between the Rx+ and Rx- wires.

The translation between serial and differential signals is done by line transceivers with switchable input and output ports. The switching allows to select the correct satellite to communicate with. Using the GPIO (general purpose input/output) pins of the Raspi, the transceivers can be switched programmatically.

On the satellite a microchip with five UART interfaces, placed behind a line transceiver, handles the selection of the correct MTD. Each message coming from the Raspi contains a hexadecimal prefix `F0` plus the index of the MTD on the satellite, which becomes `F3` for the third MTD. To ignore completely wrong messages, the microchip waits for a byte between `F1` and `F4`, selects the correct output interface and redirects the message. Then it waits for up to 100 ms for an answer and sends it back.

Software backend

The programming back end is written in Python and runs on the Raspberry Pi. Its main role is to translate between the serial commands and comfortable programming commands, and to address the correct MTD in the desired satellite. For that, the process to send a command to a MTD is:

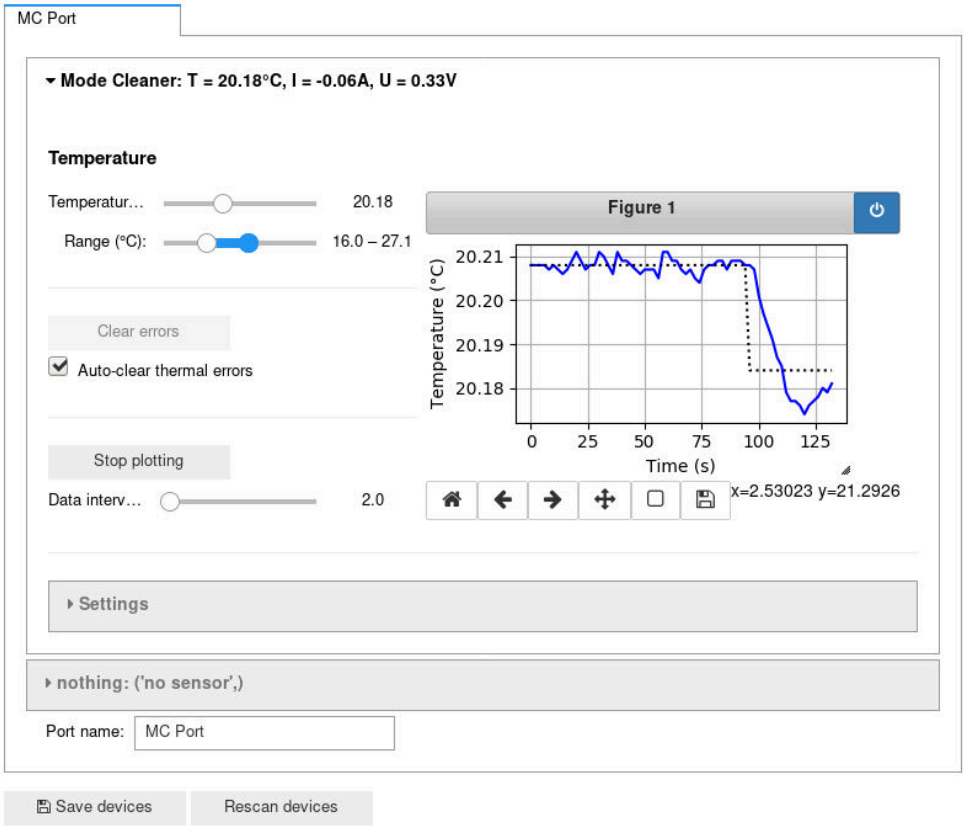

Figure 5.20: MTD view with the often used parameters of a temperature controller. The temperature and a range limit can be set and a real-time plot is provided.

1. Block the communication for other threads, as multiprocessing is used for the GUI.
2. Enable the GPIO pins for the desired satellite port, one for sending and one to receive.
3. Send the command with a prefix to address the correct MTD.
4. Wait for the answer (or break after timeout).
5. Release the multiprocessing block.

The software is structured object oriented with a class `Raspitemp` representing the main controlling board. This handles multiple satellites which are represented by the class `Port`. Each `Port` handles the MTDs soldered on the circuit board, represented by the class `MTD415`.

On startup, all ports are scanned for MTDs to check which devices are connected. All settings, such as PID parameters, temperatures, names of satellites and MTDs, can be saved to a JSON[3] file which is read and applied again on startup.

Graphical user interface

For the daily lab work, the temperature control system should be easy to handle and to play with. Therefore, I created a graphical user interface (GUI) using widgets in a Jupyter notebook. Such a notebook is used in a browser and runs as a server in the background, having system

[3]JSON, short for *JavaScript Object Notation*, is a compact, text based file format to describe objects. It is comparable to XML, but less verbose.

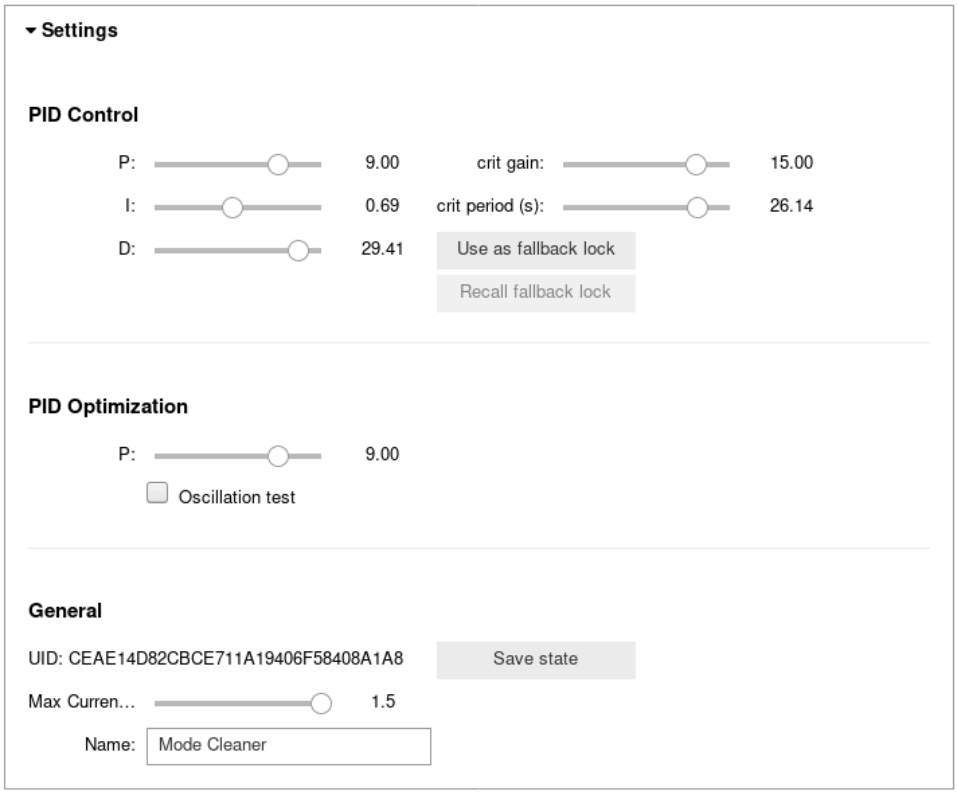

Figure 5.21: Settings for the controller configuration. The PID filters can be tuned or alternatively the recommended parameters critical gain and critical period. To enable playing with the filters, they can be saved to undo the changes if they did not improve the stabilization. An oscillation test can trigger a temperature step to enforce oscillations to use the Ziegler-Nichols optimization method.

access and the possibility to run Python code. Usually, the notebooks are used to combine data evaluation with plotting and data output. This way, it is easy to run custom commands to automate temperature optimization or measurement processes. Otherwise, the GUI provides a real-time overview of all sensors and gives the user the opportunity to manipulate them.

The GUI is structured like the real system and shows in each tab the available temperature sensors (figure 5.20). For each controller the temperature and the allowed temperature range can be set. Also a time series can be plotted to supervise the behaviour of the system (figure 5.22).

In the settings (figure 5.21) the PID control parameters and the maximum current can be set. The additional parameters *critical gain* and *critical period* can be used for a PID optimization technique that uses controlled oscillation. For this method, the critical proportional (P) gain is searched where the system answers on a disturbation with a small continuous oscillation. When the box *oscillation test* is checked, the temperature is increased by 0.1 °C to provide a disturbation and the plot shows a fit for a damped harmonic oscillator (figure 5.22) with the corresponding fitting results. This critical gain and the resulting oscillation period can be used for the MTD to calculate the PID parameters with the Ziegler-Nichols method [ZN42], usually providing a sufficiently good lock.

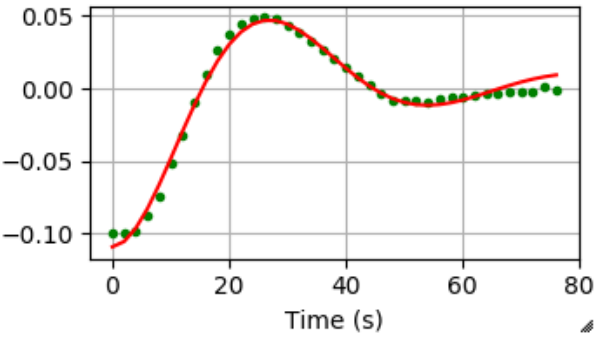

Figure 5.22: Fit view with good control filters. After the first overshoot, the real temperature is stabilized faster than the fit can follow, which assumes a damped harmonic oscillator.

Software operating options

There are two ways to run the Jupyter server that is used to control the temperatures to optimize for different needs. The first approach is to run the server on the Raspi and control it via network from another computer's browser. It is the simplest solution providing a nearly ready-to-run setup. Technically, the server runs in a Docker container[4] to provide freely selectable Python versions and to avoid the necessity of compiling `SciPy`, which would take several hours on a Raspi.

The second approach is to run the Jupyter server on the main laboratory computer and use remote serial and remote GPIO connections. It is more complicated to set up, but unifies the control of multiple devices to simplify taking measurements. This way, we are able to control the locks with NQontrol, change the crystal temperatures and take measurements with the oscilloscope and a spectrum analyzer, only using one single Python script. This feature allowed us to scan the 2D temperature parameter space presented in figure 3.10.

Temperature range manipulation

Some nonlinear crystals require a phase matching temperature above 45 °C. Hence, together with Maik Schröder I created a temperature manipulation method to reach higher temperatures. The MTD internally reads out the temperature sensor using a voltage divider, which has accessible contacts to the outside. With using slightly different NTCs or additional resistors on one of the voltage divider sides, the temperature seen by the MTD can be manipulated. This way, we made it possible to heat up to 75 °C while the MTD sees only 45 °C. The selected NTC with its characteristic curve and the used manipulation resistors can be selected in the GUI to make the user see the correct temperatures, even if the MTD works with wrong virtual temperatures. Obviously, if the overall temperature range is increased with the manipulation, the accuracy of the readout is decreased and PID parameters may need to be optimized for the temperatures of main usage.

[4]Docker containers are virtual environments to run software in a clean environment.

5.3.3 Daily lab usage

To sum up, the Raspitemp prototype has proven to be a reliable tool in the experiment, providing an accurate and reproducible temperature control. The digitalization allows even to recall old temperatures from a backup, which makes it easy to operate with PID parameters and temperatures to try optimizing it even more. If the optimization fails, it can easily be restored to the previous values. Furthermore, the ability to program temperature changes are very handy for automated measurements, such as 2D temperature maps, as used to get an overview of the temperature depending conversion characteristics.

5.4 Summary

Digital control systems provide high flexibility and enable automation as well as remote control, which is not easily possible with the classical analog systems. In the scope of this thesis, two digital control systems were developed which replace the formerly used analog devices used in the group. NQontrol (section 5.2) provides eight servo channels in one device with a sampling rate of 200 kHz. Control bandwidths of several kilohertz can easily be reached when fast actuators are used. All servos can be controlled with either a graphical user interface or a programmical Python interface, allowing automation scripts. The included autolock proved to be very helpful to automatically lock the cavities and to relock them if the beam was interrupted. Unused channels were used to scan additional cavities such as the confocal cavity and to monitor photodiodes.

The other developed digital control system Raspitemp (section 5.3) allows to control up to 20 temperatures with a precision of some Millikelvin. It uses a modular approach, where new satellites with up to four individual temperature controllers can easily be added, requiring only one LAN cable to connect. A graphical user interfaces in a Jupyter notebook is used to control all temperatures and can seamlessly be extended with Python scripting. The scripting possibility allowed to do elaborate measurements such as the 2D temperature scans (figure 3.10), where several thousands of temperature combinations were measured.

6 | Summary and Outlook

Current GWOs are in a wide frequency range limited by quantum noise and coating Brownian noise of the test masses. To circumvent the limitation by thermal noise of the coatings in future observatories, the test masses should be cooled to cryogenic temperatures, requiring a change of mirror and coating materials. A promising material candidate is silicon for the test mass with silicon-based coatings, which makes a change of the laser wavelength to $\geq 1.8\,\mu\text{m}$ necessary. The wavelengths $1.55\,\mu\text{m}$ and $2\,\mu\text{m}$ are currently being investigated, where the telecom wavelength has the advantage of existing technology while the latter could reduce the coating noise even further.

This thesis presented a novel approach to combine squeezed light generation at 2128 nm with degenerate optical-parametric oscillation pumped by an ultra-stable Mephisto laser at 1064 nm. The wavelength conversion scheme is a possible candidate as light source around $2\,\mu\text{m}$ for future GWOs. We achieved a high external conversion efficiency of $\eta = (87.1 \pm 0.4)\,\%$, which is especially important for adaption to high-power conversion to keep losses and heating of components to a minimum. If the elliptic beam of the Mephisto laser is being corrected, the efficiency can be improved further. The conversion adds only little noise to the pump laser in the range of 1 to 4 dB without active power stabilization. Altogether, our $2\,\mu\text{m}$ light source served as reliable laser for our squeezing experiment. The only drawback was sensitivity of the signal/idler degeneracy, which can be held over long time, but gets easily non-degenerate on back-reflections or changing room temperatures. The sensitivity on back-reflections can be reduced with optical isolators, but good Faraday isolators with high transmission, low reflection and high isolation still need to be developed for the wavelength and are not yet commercially available. Degeneracy monitoring and finding can be automated using the two digital control systems (NQontrol and Raspitemp) that control the experiment and were developed in the scope of this thesis. The conversion can be adapted to operate at higher conversion power, avoiding the usage of thulium or holmium fiber amplifiers.

NQontrol is an open source project to control a wide range of feedback systems with a sampling rate of 200 kHz and five second-order filters per channel. It can control up to eight channels simultaneously and is managed by a computer via network. The graphical user interface, the Python interface and the automated locking option made it a central tool for lab usage and automated measurements. Furthermore, I developed Raspitemp to have one centralized and digital system to control all temperatures on the optical table, also having a graphical and a Python interface. In contrast to commercially available products it provides high precision ($< 10\,\text{mK}$) and can control many (up to 20) temperatures simultaneously, while not being expensive.

We combined the converted light with squeezing and achieved (7.2 ± 0.2) dB of quantum noise reduction at MHz sideband frequencies, being mainly limited by the quantum efficiency of the available photodiodes. The concept of wavelength-doubling, combined with squeezing, makes the wavelength 2128 nm a promising, because cost-efficient candidate for all next-generation gravitational-wave detectors like Cosmic Explorer, Einstein Telescope, NEMO and LIGO Voyager. In these observatories, a squeezing level of 10 dB is usually aimed at. A reduction of optical loss within the detector to around 6.3 % may be within reach, for realistic technological advances. Further research into low-noise photo detectors with a quantum efficiency of 99 % is required to achieve this goal also at 2 µm.

Appendix

A Homodyne detector

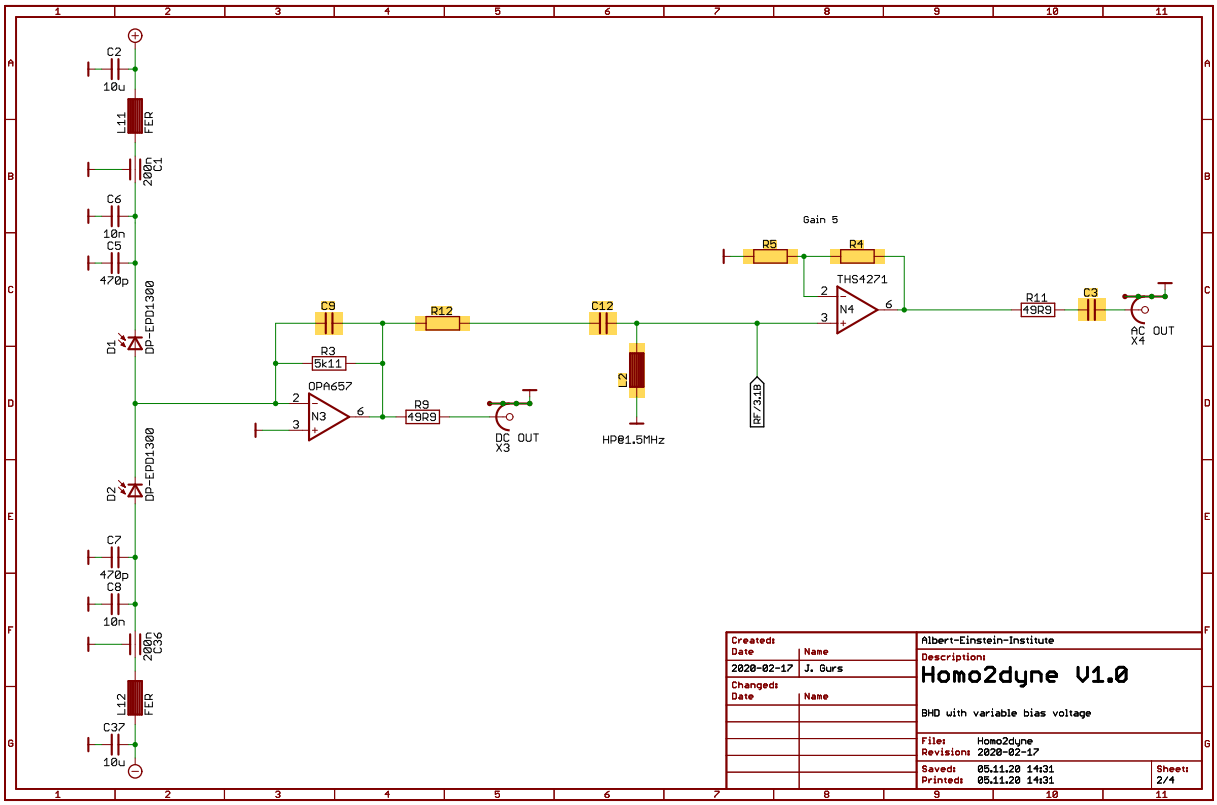

Figure 1: Customization of the homodyne detector electronics. A variable reverse voltage is included to the existing circuit board.

B Temperature control system

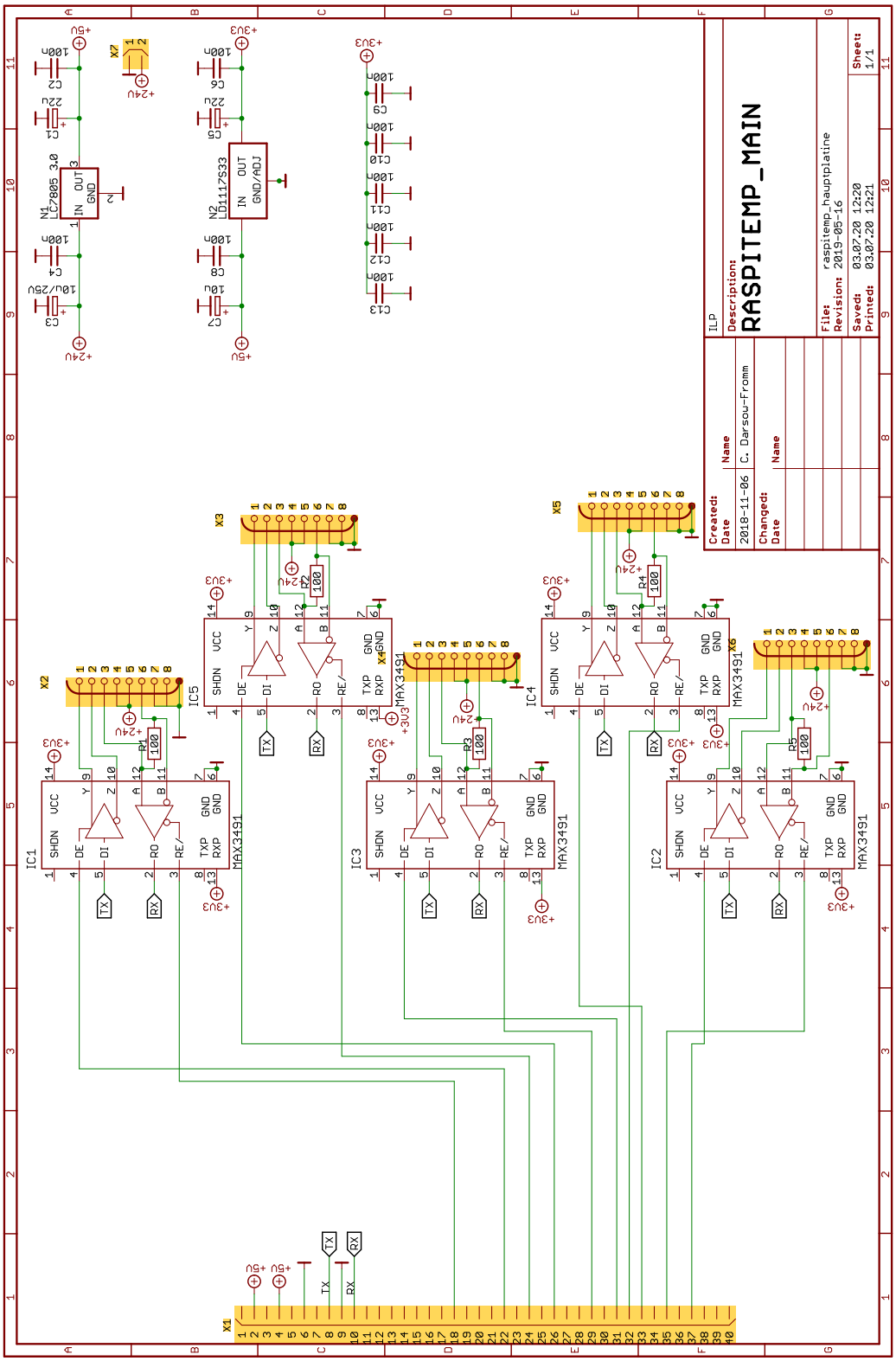

Figure 2: Schematics of the main circuit board, which delivers power and communication to all satellites.

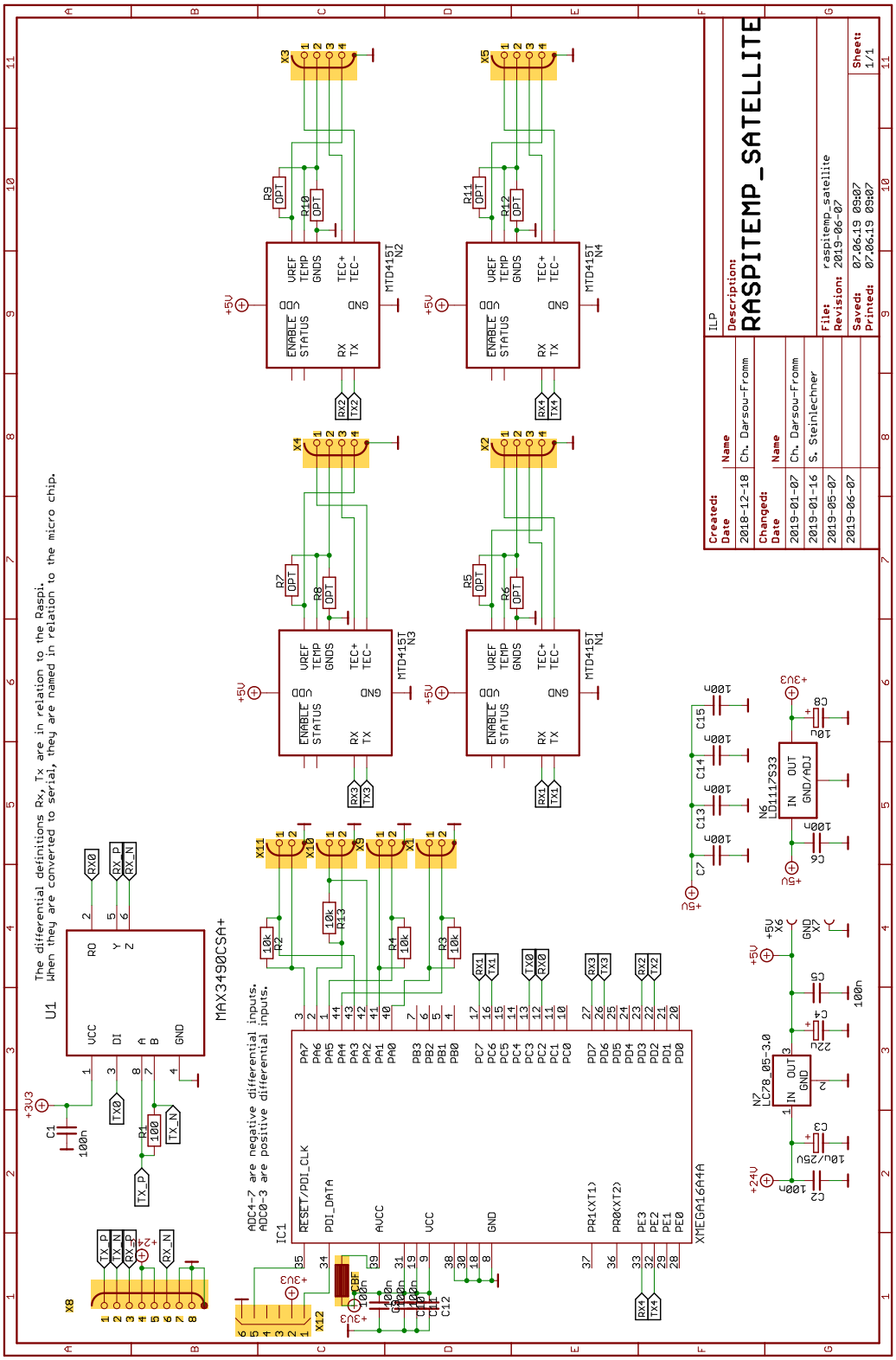

Figure 3: Schematics of the satellite, which includes a microcontroller and delivers the communication to four temperature controllers.

Bibliography

[Aas+15] J Aasi et al. "Advanced LIGO". In: *Classical and Quantum Gravity* 32.7 (Apr. 2015), p. 074001. DOI: 10.1088/0264-9381/32/7/074001.

[Abb+16] B. P. Abbott et al. "Observation of Gravitational Waves from a Binary Black Hole Merger". In: *Physical Review Letters* 116.6 (Feb. 2016). DOI: 10.1103/physrevlett.116.061102.

[Abb+17a] B. P. Abbott et al. "A Gravitational-Wave Standard Siren Measurement of the Hubble Constant". In: *Nature* 551.7678 (Nov. 2017), pp. 85–88. DOI: 10.1038/nature24471.

[Abb+17b] B. P. Abbott et al. "Estimating the Contribution of Dynamical Ejecta in the Kilonova Associated with GW170817". In: *The Astrophysical Journal* 850.2 (Dec. 2017), p. L39. DOI: 10.3847/2041-8213/aa9478.

[Abb+17c] B. P. Abbott et al. "Gravitational Waves and Gamma-Rays from a Binary Neutron Star Merger: GW170817 and GRB 170817A". In: *The Astrophysical Journal* 848.2 (Oct. 2017), p. L13. DOI: 10.3847/2041-8213/aa920c.

[Abb+21] R. Abbott et al. "Search for Anisotropic Gravitational-Wave Backgrounds Using Data from Advanced LIGO and Advanced Virgo's First Three Observing Runs". In: *Physical Review D* 104.2 (July 2021), p. 022005. DOI: 10.1103/PhysRevD.104.022005.

[Ace+15] F Acernese et al. "Advanced Virgo: A Second-Generation Interferometric Gravitational Wave Detector". In: *Classical and Quantum Gravity* 32.2 (Jan. 2015), p. 024001. DOI: 10.1088/0264-9381/32/2/024001.

[Ace+19] F. Acernese et al. "Increasing the Astrophysical Reach of the Advanced Virgo Detector via the Application of Squeezed Vacuum States of Light". In: *Physical Review Letters* 123.23 (Dec. 2019), p. 231108. DOI: 10.1103/PhysRevLett.123.231108.

[Ack+20] K. Ackley et al. "Neutron Star Extreme Matter Observatory: A Kilohertz-Band Gravitational-Wave Detector in the Global Network". In: *Publications of the Astronomical Society of Australia* 37 (2020). DOI: 10.1017/pasa.2020.39.

[Adh+20] R X Adhikari et al. "A Cryogenic Silicon Interferometer for Gravitational-Wave Detection". In: *Classical and Quantum Gravity* 37.16 (Aug. 2020), p. 165003. DOI: 10.1088/1361-6382/ab9143. arXiv: 2001.11173.

[ANR04] Gunnar Arisholm, Ørnulf Nordseth, and Gunnar Rustad. "Optical Parametric Master Oscillator and Power Amplifier for Efficient Conversion of High-Energy Pulses with High Beam Quality". In: *Optics Express* 12.18 (Sept. 2004), pp. 4189–4197. DOI: 10.1364/OPEX.12.004189.

[Ari+02] G. Arisholm et al. "Efficient Conversion from 1 to 2 μm by a KTP-based Ring Optical Parametric Oscillator". In: *Optics Letters* 27.15 (Aug. 2002), p. 1336. DOI: 10.1364/ol.27.001336.

[Bar+18] L Barsotti et al. *The Updated Advanced LIGO Design Curve*. Tech. rep. 2018. URL: https://dcc.ligo.org/LIGO-T1800044/public.

[Bec05] John Bechhoefer. "Feedback for Physicists: A Tutorial Essay on Control". In: *Reviews of Modern Physics* 77.3 (Aug. 2005), pp. 783–836. DOI: 10.1103/RevModPhys.77.783.

[BF14] Daniel David Brown and Andreas Freise. *Finesse*. May 2014. DOI: 10.5281/zenodo.821363.

[BF17] Daniel David Brown and Andreas Freise. *Pykat*. July 2017. DOI: 10.5281/zenodo.821389.

[Bos+96] Walter R. Bosenberg et al. "93% Pump Depletion, 3.5-W Continuous-Wave, Singly Resonant Optical Parametric Oscillator". In: *Optics Letters* 21.17 (Sept. 1996), pp. 1336–1338. DOI: 10.1364/OL.21.001336.

[Boy08] Robert W. Boyd. *Nonlinear Optics*. Elsevier, May 2008.

[Bri+19] J Briggs et al. *Using Extended InGaAs Photodiodes for the Detection of Gravitational Waves*. 2019. URL: https://dcc.ligo.org/LIGO-P1900325.

[BSM95] G. Breitenbach, S. Schiller, and J. Mlynek. "81% Conversion Efficiency in Frequency-Stable Continuous-Wave Parametric Oscillation". In: *JOSA B* 12.11 (Nov. 1995), pp. 2095–2101. DOI: 10.1364/JOSAB.12.002095.

[But16] Butix, based on works by Lucasbosch and Cmykey. *Vector Illustration of a Raspberry Pi 3*. Oct. 2016. URL: https://commons.wikimedia.org/wiki/File:Raspberry_Pi_3_illustration.svg (visited on 04/09/2022).

[Cav81] Carlton M. Caves. "Quantum-Mechanical Noise in an Interferometer". In: *Physical Review D* 23.8 (Apr. 1981), pp. 1693–1708. DOI: 10.1103/PhysRevD.23.1693.

[Che+05] Simon Chelkowski et al. "Experimental Characterization of Frequency-Dependent Squeezed Light". In: *Physical Review A* 71.1 (Jan. 2005), p. 013806. DOI: 10.1103/PhysRevA.71.013806.

[Col+21] The LIGO Scientific Collaboration et al. "Upper Limits on the Isotropic Gravitational-Wave Background from Advanced LIGO's and Advanced Virgo's Third Observing Run". In: *arXiv:2101.12130 [astro-ph, physics:gr-qc]* (Jan. 2021). arXiv: 2101.12130.

[Cre21] Teviet Creighton. *Gravitational Waves Demystified*. 2021. URL: http://www.tapir.caltech.edu/~teviet/Waves/ (visited on 06/23/2021).

[Dar+20a] Christian Darsow-Fromm et al. "Highly efficient generation of coherent light at 2128 nm via degenerate optical-parametric oscillation". In: *Optics Letters* 45.22 (Nov. 2020), pp. 6194–6197. DOI: 10.1364/OL.405396. arXiv: 2008.07193.

[Dar+20b] Christian Darsow-Fromm et al. "NQontrol: An Open-Source Platform for Digital Control-Loops in Quantum-Optical Experiments". In: *Review of Scientific Instruments* 91.3 (Mar. 2020), p. 035114. DOI: 10.1063/1.5135873. arXiv: 1911.08824.

[Dar+21] Christian Darsow-Fromm et al. "Squeezed light at 2128 nm for future gravitational-wave observatories". In: *Optics Letters* 46.23 (Dec. 2021), pp. 5850–5853. DOI: 10.1364/OL.433878. arXiv: 2105.10209.

[Dek19] Luis Dekant. "Algorithmische Regleroptimierung in Python". BA thesis. Universität Hamburg, 2019.

[Dre+83] R. W. P. Drever et al. "Laser Phase and Frequency Stabilization Using an Optical Resonator". In: *Applied Physics B* 31.2 (June 1983), pp. 97–105. DOI: 10.1007/BF00702605.

[Eck+91] Robert C. Eckardt et al. "Optical Parametric Oscillator Frequency Tuning and Control". In: *Journal of the Optical Society of America B* 8.3 (Mar. 1991), p. 646. DOI: 10.1364/JOSAB.8.000646.

[ET 11] ET Science Team. *Einstein Gravitational Wave Telescope Conceptual Design Study*. 2011. URL: https://tds.virgo-gw.eu/ql/?c=7954.

[ET 20] ET Steering Committee Editorial Team. *Einstein Telescope Design Report Update 2020*. Sept. 2020. URL: https://apps.et-gw.eu/tds/?content=3&r=16984.

[ETp20] ETpathfinder Team. *ETpathfinder Design Report*. 2020. URL: https://dcc.ligo.org/LIGO-P2000109.

[Fej+92] M.M. Fejer et al. "Quasi-Phase-Matched Second Harmonic Generation: Tuning and Tolerances". In: *IEEE Journal of Quantum Electronics* 28.11 (1992), pp. 2631–2654. DOI: 10.1109/3.161322.

[Fri+20] Peter Fritschel et al. *Instrument Science White Paper 2020*. 2020. URL: https://dcc.ligo.org/LIGO-T2000407.

[Gen+92] M. Gendry et al. "Critical Thicknesses of Highly Strained InGaAs Layers Grown on InP by Molecular Beam Epitaxy". In: *Applied Physics Letters* 60.18 (May 1992), pp. 2249–2251. DOI: 10.1063/1.107045.

[GK05] Christopher Gerry and Peter Knight. "Introductory Quantum Optics". In: (2005), p. 333.

[GK95] Martin A. Green and Mark J. Keevers. "Optical Properties of Intrinsic Silicon at 300 K". In: *Progress in Photovoltaics: Research and Applications* 3.3 (1995), pp. 189–192. DOI: 10.1002/pip.4670030303.

[GM65] J. A. Giordmaine and Robert C. Miller. "Tunable Coherent Parametric Oscillation in LiNb O 3 at Optical Frequencies". In: *Physical Review Letters* 14.24 (June 1965), pp. 973–976. DOI: 10.1103/PhysRevLett.14.973.

[Gro+13] H. Grote et al. "First Long-Term Application of Squeezed States of Light in a Gravitational-Wave Observatory". In: *Physical Review Letters* 110.18 (May 2013), p. 181101. DOI: 10.1103/PhysRevLett.110.181101.

[Gur21] Julian Gurs. "Generation of Squeezed Light at the Sub-Harmonic Wavelength of the Nd:YAG Laser at 2128 nm". MA thesis. Universität Hamburg, 2021.

[Har+02] Gregory M. Harry et al. "Thermal Noise in Interferometric Gravitational Wave Detectors Due to Dielectric Optical Coatings". In: *Classical and Quantum Gravity* 19.5 (Feb. 2002), pp. 897–917. DOI: 10.1088/0264-9381/19/5/305.

[Hil+10] S Hild et al. "A Xylophone Configuration for a Third-Generation Gravitational Wave Detector". In: *Classical and Quantum Gravity* 27.1 (Jan. 2010), p. 015003. DOI: 10.1088/0264-9381/27/1/015003.

[Hir+14] Eiichi Hirose et al. "Sapphire Mirror for the KAGRA Gravitational Wave Detector". In: *Physical Review D* 89.6 (Mar. 2014), p. 062003. DOI: 10.1103/PhysRevD.89.062003.

[HRS02] Gerhard Heinzel, Albrecht Rüdiger, and Roland Schilling. *Spectrum and Spectral Density Estimation by the Discrete Fourier Transform (DFT), Including a Comprehensive List of Window Functions and Some New at-Top Windows*. Tech. rep. Max-Planck-Institut für Gravitationsphysik, 2002. URL: http://hdl.handle.net/11858/00-001M-0000-0013-557A-5 (visited on 04/07/2022).

[Jäg] Jäger GmbH. *ADwin*. URL: https://www.adwin.de/ (visited on 12/29/2021).

[JNN13] J. R. Johansson, P. D. Nation, and Franco Nori. "QuTiP 2: A Python Framework for the Dynamics of Open Quantum Systems". In: *Computer Physics Communications* 184.4 (Apr. 2013), pp. 1234–1240. DOI: 10.1016/j.cpc.2012.11.019.

[Kas+17] Daniel Kasen et al. "Origin of the Heavy Elements in Binary Neutron-Star Mergers from a Gravitational-Wave Event". In: *Nature* 551.7678 (Nov. 2017), pp. 80–84. DOI: 10.1038/nature24453.

[KB85] Thomas J. Kane and Robert L. Byer. "Monolithic, Unidirectional Single-Mode Nd:YAG Ring Laser". In: *Optics Letters* 10.2 (Feb. 1985), p. 65. DOI: 10.1364/OL.10.000065.

[KE95] J. Kennedy and R. Eberhart. "Particle Swarm Optimization". In: *Proceedings of ICNN'95 - International Conference on Neural Networks*. Vol. 4. Perth, WA, Australia: IEEE, 1995, pp. 1942–1948. DOI: 10.1109/ICNN.1995.488968.

[Kha10] F. Ya. Khalili. "Optimal Configurations of Filter Cavity in Future Gravitational-Wave Detectors". In: *Physical Review D* 81.12 (June 2010), p. 122002. DOI: 10.1103/PhysRevD.81.122002.

[Kim+01] H. J. Kimble et al. "Conversion of Conventional Gravitational-Wave Interferometers into Quantum Nondemolition Interferometers by Modifying Their Input and/or Output Optics". In: *Physical Review D* 65.2 (Dec. 2001), p. 022002. DOI: 10.1103/PhysRevD.65.022002.

[Las10] Nico Lastzka. "Numerical Modelling of Classical and Quantum Effects in Non-Linear Optical Systems". PhD thesis. Universität Hannover, 2010.

[Lev98] Yu. Levin. "Internal Thermal Noise in the LIGO Test Masses: A Direct Approach". In: *Physical Review D* 57.2 (Jan. 1998), pp. 659–663. DOI: 10.1103/PhysRevD.57.659.

[LIG] LIGO Scientific Collaboration. *Gwinc / Pygwinc*. URL: https://git.ligo.org/gwinc/pygwinc (visited on 03/08/2022).

[LIG11] LIGO Scientific Collaboration. "A Gravitational Wave Observatory Operating beyond the Quantum Shot-Noise Limit". In: *Nature Physics* 7.12 (Dec. 2011), pp. 962–965. DOI: 10.1038/nphys2083.

[LIG16] LIGO Scientific Collaboration. "The LSC-Virgo White Paper on Instrument Science". In: (2016). URL: https://dcc.ligo.org/LIGO-T1600119/public.

[LIG17] LIGO Scientific Collaboration and Virgo Collaboration. "GW170817: Observation of Gravitational Waves from a Binary Neutron Star Inspiral". In: *Physical Review Letters* 119.16 (Oct. 2017), p. 161101. DOI: 10.1103/PhysRevLett.119.161101.

[LIG19] LIGO Scientific Collaboration. *Instrument Science White Paper 2019*. Tech. rep. 2019. URL: https://dcc.ligo.org/LIGO-T1900409/public (visited on 03/31/2020).

[LIG20] LIGO Scientific Collaboration and Virgo Collaboration. "GW190814: Gravitational Waves from the Coalescence of a 23 Solar Mass Black Hole with a 2.6 Solar Mass Compact Object". In: *The Astrophysical Journal* 896.2 (June 2020), p. L44. DOI: 10.3847/2041-8213/ab960f.

[LLM81] L. D. Landau, E. M. Lifshitz, and John Menzies. *Quantum Mechanics: Non-Relativistic Theory*. United Kingdom: Elsevier Science & Technology, 1981.

[Loe20] Abraham Loeb. "Upper Limit on the Dissipation of Gravitational Waves in Gravitationally Bound Systems". In: *The Astrophysical Journal* 890.2 (Feb. 2020), p. L16. DOI: 10.3847/2041-8213/ab72ab.

[Lou+21] James Lough et al. "First Demonstration of 6 dB Quantum Noise Reduction in a Kilometer Scale Gravitational Wave Observatory". In: *Physical Review Letters* (2021), p. 7.

[Lug+88] L. A. Lugiato et al. "Bistability, Self-Pulsing and Chaos in Optical Parametric Oscillators". In: *Il Nuovo Cimento D* 10.8 (Aug. 1988), pp. 959–977. DOI: 10.1007/BF02450197.

[Ma+17] Yiqiu Ma et al. "Proposal for Gravitational-Wave Detection beyond the Standard Quantum Limit through EPR Entanglement". In: *Nature Physics* 13.8 (Aug. 2017), pp. 776–780. DOI: 10.1038/nphys4118.

[Man+18] Georgia L. Mansell et al. "Observation of Squeezed Light in the 2um Region". In: *Physical Review Letters* 120.20 (May 2018). DOI: 10.1103/physrevlett.120.203603.

[Mar+01] M Martinelli et al. "Ultra-Low Threshold CW Triply Resonant OPO in the near Infrared Using Periodically Poled Lithium Niobate". In: *Journal of Optics A: Pure and Applied Optics* 3.4 (July 2001), pp. 300–303. DOI: 10.1088/1464-4258/3/4/312.

[Mar+09] I. W. Martin et al. "Comparison of the Temperature Dependence of the Mechanical Dissipation in Thin Films of Ta_2O_5 and Ta_2O_5 Doped with TiO_2". In: *Classical and Quantum Gravity* 26.15 (July 2009), p. 155012. DOI: 10.1088/0264-9381/26/15/155012.

[Mar+12] Alireza Marandi et al. "All-Optical Quantum Random Bit Generation from Intrinsically Binary Phase of Parametric Oscillators". In: *Optics Express* 20.17 (Aug. 2012), pp. 19322–19330. DOI: 10.1364/OE.20.019322.

[Mar+14] I. W. Martin et al. "Low Temperature Mechanical Dissipation of an Ion-Beam Sputtered Silica Film". In: *Classical and Quantum Gravity* 31.3 (Jan. 2014), p. 035019. DOI: 10.1088/0264-9381/31/3/035019.

[McK11] Wes McKinney. "Pandas: A Foundational Python Library for Data Analysis and Statistics". In: *Python for High Performance and Scientific Computing* 14 (2011).

[Mos+86] A.J. Moseley et al. "High-Efficiency, Low-Leakage MOCVD-grown GaInAs/AlInAs Heterojunction Photodiodes for Detection to 2.4μm". In: *Electronics Letters* 22.22 (1986), p. 1206. DOI: 10.1049/el:19860826.

[Mur+15] Peter G. Murray et al. "Ion-Beam Sputtered Amorphous Silicon Films for Cryogenic Precision Measurement Systems". In: *Physical Review D* 92.6 (Sept. 2015), p. 062001. DOI: 10.1103/PhysRevD.92.062001.

[MV18] M. Mehmet and H. Vahlbruch. "High-Efficiency Squeezed Light Generation for Gravitational Wave Detectors". In: *Classical and Quantum Gravity* 36.1 (Dec. 2018), p. 015014. DOI: 10.1088/1361-6382/aaf448.

[MZL88] Ramon U. Martinelli, Thomas J. Zamerowski, and Paul A. Longeway. "2.6 µm InGaAs Photodiodes". In: *Applied Physics Letters* 53.11 (Sept. 1988), pp. 989–991. DOI: 10.1063/1.100050.

[Nab+90] C. D. Nabors et al. "Coherence Properties of a Doubly Resonant Monolithic Optical Parametric Oscillator". In: *JOSA B* 7.5 (May 1990), pp. 815–820. DOI: 10.1364/JOSAB.7.000815.

[Oli06] Travis E Oliphant. *A Guide to NumPy*. Vol. 1. Trelgol Publishing USA, 2006.

[PDS] Jan Petermann, Christian Darsow-Fromm, and Sebastian Steinlechner. *OpenQlab*. Group LasNQ, University of Hamburg. URL: https://gitlab.com/las-nq/openqlab.

[Plo] Plotly Technologies Inc. *Dash*. URL: https://plot.ly/products/dash (visited on 12/28/2021).

[PPF11] C. R. Phillips, J. S. Pelc, and M. M. Fejer. "Continuous Wave Monolithic Quasi-Phase-Matched Optical Parametric Oscillator in Periodically Poled Lithium Niobate". In: *Optics Letters* 36.15 (Aug. 2011), p. 2973. DOI: 10.1364/OL.36.002973.

[Rei+19] David Reitze et al. "Cosmic Explorer: The U.S. Contribution to Gravitational-Wave Astronomy beyond LIGO". In: *Bulletin of the AAS* 51.7 (Sept. 2019). URL: https://baas.aas.org/pub/2020n7i035/release/1 (visited on 12/29/2021).

[RY92] M. D. Reid and B. Yurke. "Effect of Bistability and Superpositions on Quantum Statistics in Degenerate Parametric Oscillation". In: *Physical Review A* 46.7 (Oct. 1992), pp. 4131–4137. DOI: 10.1103/PhysRevA.46.4131.

[Sau17] Peter R. Saulson. *Fundamentals of Interferometric Gravitational Wave Detectors*. Second edition. Hackensack, NJ: World Scientific, 2017.

[Sch+10] Roman Schnabel et al. "Quantum Metrology for Gravitational Wave Astronomy". In: *Nature Communications* 1.1 (Dec. 2010), p. 121. DOI: 10.1038/ncomms1122.

[Sch17] Roman Schnabel. "Squeezed States of Light and Their Applications in Laser Interferometers". In: *Physics Reports* 684 (Apr. 2017), pp. 1–51. DOI: 10.1016/j.physrep.2017.04.001.

[Sch18] Axel Schönbeck. "Compact squeezed-light source at 1550 nm". PhD thesis. Hamburg: Universität Hamburg, 2018.

[Sch19] Maik Schröder. "Setup and Characterization of a Bright Light Source at 2128 nm". MA thesis. Universität Hamburg, 2019.

[Sch26] E. Schrödinger. "Der stetige Übergang von der Mikro- zur Makromechanik". In: *Naturwissenschaften* 14.28 (July 1926), pp. 664–666. DOI: 10.1007/BF01507634.

[SE98] Y. Shi and R. Eberhart. "A Modified Particle Swarm Optimizer". In: *1998 IEEE International Conference on Evolutionary Computation Proceedings. IEEE World Congress on Computational Intelligence (Cat. No.98TH8360)*. Anchorage, AK, USA: IEEE, 1998, pp. 69–73. DOI: 10.1109/ICEC.1998.699146.

[SH10] Orazio Svelto and D. C. Hanna. *Principles of Lasers*. 5th ed. New York: Springer, 2010.

[Sho19] DavidMcLaughlin Shoemaker. *Gravitational-Wave Astronomy in the 2020s and Beyond: A View Across the Gravitational Wave Spectrum*. Tech. rep. Mar. 2019. URL: https://ntrs.nasa.gov/search.jsp?R=20190002313 (visited on 07/01/2020).

[SSD16] Arlee V. Smith, Jesse J. Smith, and Binh T. Do. "Thermo-Optic and Thermal Expansion Coefficients of RTP and KTP Crystals over 300-350 K". In: (July 2016). arXiv: 1607.03964.

[Ste+18] J. Steinlechner et al. "Silicon-Based Optical Mirror Coatings for Ultrahigh Precision Metrology and Sensing". In: *Physical Review Letters* 120.26 (June 2018), p. 263602. DOI: 10.1103/PhysRevLett.120.263602.

[Süd+20] Jan Südbeck et al. "Demonstration of Interferometer Enhancement through Einstein–Podolsky–Rosen Entanglement". In: *Nature Photonics* 14.4 (Apr. 2020), pp. 240–244. DOI: 10.1038/s41566-019-0583-3.

[Tak+07] Yuishi Takeno et al. "Observation of -9 dB Quadrature Squeezing with Improvement of Phase Stability in Homodyne Measurement". In: *Optics Express* 15.7 (Apr. 2007), pp. 4321–4327. DOI: 10.1364/OE.15.004321.

[TH06] Michael Tröbs and Gerhard Heinzel. "Improved Spectrum Estimation from Digitized Time Series on a Logarithmic Frequency Axis". In: *Measurement* 39.2 (Feb. 2006), pp. 120–129. DOI: 10.1016/j.measurement.2005.10.010.

[Tse+19] M. Tse et al. "Quantum-Enhanced Advanced LIGO Detectors in the Era of Gravitational-Wave Astronomy". In: *Physical Review Letters* 123.23 (Dec. 2019), p. 231107. DOI: 10.1103/PhysRevLett.123.231107.

[Ueh+97] Noboru Uehara et al. "Modeling of Efficient Mode-Matching and Thermal-Lensing Effect on a Laser-Beam Coupling into a Mode-Cleaner Cavity". In: *Modeling and Simulation of Higher-Power Laser Systems IV*. Vol. 2989. International Society for Optics and Photonics, May 1997, pp. 57–68. DOI: 10.1117/12.273681.

[Vah+07] H Vahlbruch et al. "Quantum Engineering of Squeezed States for Quantum Communication and Metrology". In: *New Journal of Physics* 9.10 (Oct. 2007), pp. 371–371. DOI: 10.1088/1367-2630/9/10/371.

[Vah+10] Henning Vahlbruch et al. "The GEO 600 Squeezed Light Source". In: *Classical and Quantum Gravity* 27.8 (Apr. 2010), p. 084027. DOI: 10.1088/0264-9381/27/8/084027.

[Vah+16] Henning Vahlbruch et al. "Detection of 15 dB Squeezed States of Light and Their Application for the Absolute Calibration of Photoelectric Quantum Efficiency". In: *Physical Review Letters* 117.11 (Sept. 2016), p. 110801. DOI: 10.1103/PhysRevLett.117.110801.

[Val+21] Eleonora Di Valentino et al. "In the Realm of the Hubble Tension—a Review of Solutions". In: *Classical and Quantum Gravity* 38.15 (July 2021), p. 153001. DOI: 10.1088/1361-6382/ac086d.

[Vir+20] Pauli Virtanen et al. "SciPy 1.0: Fundamental Algorithms for Scientific Computing in Python". In: *Nature Methods* (2020). DOI: 10.1038/s41592-019-0686-2.

[WD97] David J. Wales and Jonathan P. K. Doye. "Global Optimization by Basin-Hopping and the Lowest Energy Structures of Lennard-Jones Clusters Containing up to 110 Atoms". In: *The Journal of Physical Chemistry A* 101.28 (July 1997), pp. 5111–5116. DOI: 10.1021/jp970984n.

[Wu+00] R. F. Wu et al. "Compact 21-W 2-µm Intracavity Optical Parametric Oscillator". In: *Optics Letters* 25.19 (Oct. 2000), p. 1460. DOI: 10.1364/ol.25.001460.

[Yap+19] M. J. Yap et al. "Squeezed Vacuum Phase Control at 2um". In: *Optics Letters* 44.21 (Nov. 2019), pp. 5386–5389. DOI: 10.1364/OL.44.005386.

[ZN42] J. G. Ziegler and N. Nichols. "Optimum Settings for Automatic Controllers". In: (1942). DOI: 10.1115/1.2899060.

Danksagung

Im Laufe dieser Arbeit waren viele Menschen wichtig, mit denen ich zusammen gearbeitet habe und die mich unterstützt haben. Angefangen mit Roman und Sebastian, die mir das Projekt anvertraut haben, obwohl ich das Angebot einige Monate vorher ausgeschlagen hatte. Vielen Dank an Roman, dass ich Teil seiner wunderbaren Arbeitsgruppe und von LIGO sein konnte, wo ich mich sehr wohl gefühlt habe. Und danke an Sebastian für die grandiose Betreuung und das gut durchdachte Projekt. Seine Tür stand immer offen für Fragen und bei der Fehlersuche, auch wenn sie leider nur noch virtuell erreichbar war, seitdem er nach Maastricht gegangen ist.

Danke auch an meine Frau Romy für die bald vierzehn gemeinsamen Jahre, das Zutrauen und insbesondere die Unterstützung in der letzten Zeit. Ebenso an meine Eltern für die Unterstützung, das Vertrauen, die Gespräche und auch das Interesse an meinem abgedrehten Forschungsthema. Und nicht zu vergessen, das Coverbild von Alexandra und das langjährige Vertrauen meiner Schwiegerfamilie.

Vielen Dank an die ganze Arbeitsgruppe, in der ich viele gute Tage hatte und an alle aus Raum 115 für die vielen physikalischen Diskussionen und unphysikalischen Gespräche. Besonders erwähnen möchte ich noch Maik und Julian, deren Masterarbeiten ich betreuen durfte sowie Luis in seiner Bachelorarbeit. Es war eine sehr gute Zusammenarbeit mit jedem einzelnen und schön, dass das Projekt von Julian noch weiter fortgeführt wird und ich weiterhin gedanklich beteiligt sein kann. Danke an Jan und Alex für die gemeinsame und inspirierende Arbeit an unseren Programmierprojekten und unsere kleinen Workshops, die wir in der Gruppe veranstaltet haben. Danke auch an Sophie für die vielen Kletterabende, die immer ein wunderbarer Ausgleich waren. Zum Abschluss vielen Dank an Torben, Sebastian und Roman für das Korrekturlesen dieser Arbeit und die wertvollen Rückmeldungen.

Eidesstattliche Versicherung / Declaration on oath

Hiermit versichere ich an Eides statt, die vorliegende Dissertationsschrift selbst verfasst und keine anderen als die angegebenen Hilfsmittel und Quellen benutzt zu haben.

Die eingereichte schriftliche Fassung entspricht der auf dem elektronischen Speichermedium.

Die Dissertation wurde in der vorgelegten oder einer ähnlichen Form nicht schon einmal in einem früheren Promotionsverfahren angenommen oder als ungenügend beurteilt.

Hamburg, den 12. Juli 2022

Unterschrift des Doktoranden